THESIS

GEOLOGIC MAPPING AND STRUCTURAL EVOLUTION OF THE DEADMAN CREEK THRUST IN THE SANGRE DE CRISTO RANGE, SOUTHERN COLORADO

Submitted by

Miriam Primus

Department of Geosciences

In partial fulfillment of requirements

For the Degree of Master of Science

Colorado State University

Fort Collins, Colorado

Spring 2026

Master's Committee:

Advisor: John Singleton

Lauren Harrison
John Ridley
Erika Szymanski

ABSTRACT

GEOLOGIC MAPPING AND STRUCTURAL EVOLUTION OF THE DEADMAN CREEK THRUST IN THE SANGRE DE CRISTO RANGE, SOUTHERN COLORADO

The western flank of the Sangre de Cristo Range in southern Colorado contains exposures of Proterozoic gneisses and granitoids that are locally thrust over slivers of Mississippian, Devonian, and Ordovician sedimentary rocks (MDO) and intruded by Oligocene granodiorite to diorite stocks and aplite dikes. These rocks record a complex geologic history that includes folding and faulting related to Laramide contraction and normal faulting and magmatism associated with Rio Grande rift extension. We investigated this multistage deformation with detailed geologic mapping and kinematic analysis of sheared rocks related to the Deadman Creek thrust – a top-NE directed thrust fault that juxtaposes Proterozoic crystalline rocks in the hanging wall over MDO in the footwall. Where the Deadman Creek thrust is best exposed away from the range front, it records top-NE contractional shear primarily localized in mylonitic MDO. This structure has been deformed by subsequent NE-vergent fault-propagation folds, locally reactivated as an extensional shear zone, and later dissected by brittle-plastic normal faults. One of these normal faults, designated as the Short Creek fault, is localized on the steep to moderately NE-dipping folded limb of the Deadman Creek thrust. Along the western flank of the range subhorizontal to gently-SW dipping mylonite zones (herein named the Duncan shear zone) in the footwall and hanging wall of the Deadman Creek thrust consistently record top-SW sense shear, opposite of the Laramide contractional regime. These zones are locally 10s of meters thick and are characterized by plastic deformation of quartz, brittle deformation of feldspar, and extensive chloritization, indicating greenschist facies deformation conditions. Quartz crystallographic preferred orientation data from mylonites in these zones are consistent with top-SW shear as well as local coaxial strain, and c-axis opening angles indicate deformation temperatures ranging from ~300–500° C. The thickest mylonite zones are found proximal to locally strained range-front Oligocene diorite and granodiorite intrusions, rather than along the contact of the Deadman Creek thrust, suggesting these mylonites are associated with magma emplacement. Zircon U-Pb data from one of these mylonitic intrusions yielded a date of 27.9 ± 0.3 Ma. Additionally, one of the NE-dipping brittle-plastic normal faults that cuts the Deadman Creek thrust involves an aplite intrusion with a 26.2 ± 0.3 Ma zircon U-Pb date. We interpret the top-SW shear zones and the brittle-plastic normal faults to record the earliest stages of Rio Grande rift extension that was coeval with magmatism and preceded development of the range-bounding Sangre de Cristo normal fault system in the Miocene.

ACKNOWLEDGEMENTS

I would first like to express my deepest gratitude to my advisor, John Singleton. This work would not have been possible without his encouragement, guidance, and steadfast support both scientifically and personally. His extensive knowledge of the geology of the Sangre de Cristo Range was invaluable in shaping this project, and I am continually grateful for the academic mentorship he has provided throughout this process.

I would also like to thank Jeffrey Rahl and Gabrielle Ursin at Washington and Lee University for their assistance with the EBSD analyses, as well as Liam Courtney-Davies at the CU TRaiL Lab for his analytical expertise in U-Pb geochronology and thermochronology, and Jonathan Caine for introducing me to the Deadman Creek field area. Fieldwork would not have been nearly as productive without the support, laughter, and teamwork of Dylan Frawley, Sammy Malavarca, Hunter Broeder, and Matt Lodi. Tackling the steep terrain, complex geology, and rapidly changing weather in the Sangre de Cristo Range made this experience both humbling and deeply rewarding, and I am grateful to have had such a reliable team with me. I am also sincerely appreciative of my committee members John Ridley, Lauren Harrison, and Erika Szymanski for their feedback and guidance, which greatly strengthened this thesis.

My sincere thanks goes to the U.S. Forest Service and the National Park Service for granting field access and for allowing several stays at Duncan Cabin, which made long days in the field much more manageable. This work was supported by the National Science Foundation (Award EAR -2115719, Tectonics program). Additional support came from research and teaching assistantships funded by the Warner College of Natural Resources. This study was built on the pioneering work of USGS Geologist David Lindsey, who passed away in Fall 2025. None of our work would have happened were it not for his heroic mapping efforts in the Sangre de Cristo Range.

Finally, I am grateful to my family, my friends, and the community within the CSU Geosciences Department for their encouragement and unwavering support throughout this entire process.

TABLE OF CONTENTS

LIST OF TABLES

LIST OF FIGURES

1. INTRODUCTION

Viewed through the lens of geologic time, humanity is a recent addition to a planet shaped by billions of years of physical, biological, and chemical processes. Studying geology provides the means to widen our perspective, revealing landscapes that evolved over millions of years and natural forces that operate far beyond human timescales. Among the most compelling records of these long-term geologic processes is the continental crust, which preserves the structure and history of Earth's ongoing tectonic evolution. This study focuses on the tectonic development of the Sangre de Cristo Range in southern Colorado, where the rocks record key events that contributed to the geologic evolution of North America and the Rocky Mountain region, including polyphase Proterozoic shortening (Jones and Connelly, 2006), Pennsylvanian-Permian deformation (the Ancestral Rocky Mountains orogeny; e.g., Hoy and Ridgway, 2002), Late Cretaceous to early Paleogene folding and thrusting (the Laramide orogeny; e.g., Lindsey and Caine, 2024), and Cenozoic extension (the Rio Grande rift; e.g., Tweto, 1979).

The influence of pre-existing geological structures and tectonic events on the development of younger geological features, known as structural inheritance, is pervasive in orogenic systems such as the Sangre de Cristo Range (e.g., Holdsworth et al., 1997; Şengör et al., 2019). Studying complex polyphase deformation helps inform orogenic processes and deformation in the continental crust. Additionally, because of recent extension related to the Rio Grande rift, the Sangre de Cristo Range exposes some of the deepest Phanerozoic crustal levels in the Rocky Mountain region, offering a rare window into the continental crust at the brittle-plastic transition (BPT) (i.e., the depth at which rocks begin deforming plastically rather than brittlely (Sibson, 1983; Kohlstedt et al., 1995; Behr and Platt, 2014); which broadly controls the distribution, rate, and mechanisms of deformation in the lithosphere. Studying the rheology, behavior, and kinematics of faults and shear zones in the Sangre de Cristo Range can help us to understand long-term deformation of the continental crust in a tectonic context.

Central to this study is the Deadman Creek thrust, a Laramide-age thrust fault exposed along the western flank of the Sangre de Cristo Range. This fault system and adjacent structures record multiple episodes of shortening, extension, and magmatism, making this area key for investigating the dynamics of intraplate continental deformation. This thesis begins with an overview of the geographic and historical context of the Sangre de Cristo Mountains, followed by a geological framework and a summary of previous work in the Deadman Creek thrust area. Subsequent sections detail the methods employed, present the results of field mapping and structural analysis, and provide a discussion of the implications for crustal deformation processes in this region.

1.1 Geographic Setting and History

The Sangre de Cristo Mountains were named in 1719 by Spanish explorer Antonio Valverde y Cosio, who, impressed at sunrise by the red-tinted snowy peaks, reportedly uttered a fervent “Sangre de Cristo” (“Blood of Christ”) (Julyan, 1998). The Sangre de Cristo Range constitutes the northern end of the Sangre de Cristo Mountains, which is itself the southernmost mountain range in the Rocky Mountains. The Culebra Range makes up the southern part of the Sangre de Cristo Mountains. Many of the summits in the Sangre de Cristo Mountains surpass 14,000 feet elevation, including Kit Carson, Crestone, Humbolt, Wheeler, and Blanca Peak.

The Sangre de Cristo Range separates the San Luis Valley on the west from the Wet Mountain Valley on the east (Figure 1a) and is approximately 15 km wide and extends 120 km in south-central Colorado from Poncha Springs to the town of Blanca. The range’s steep slopes

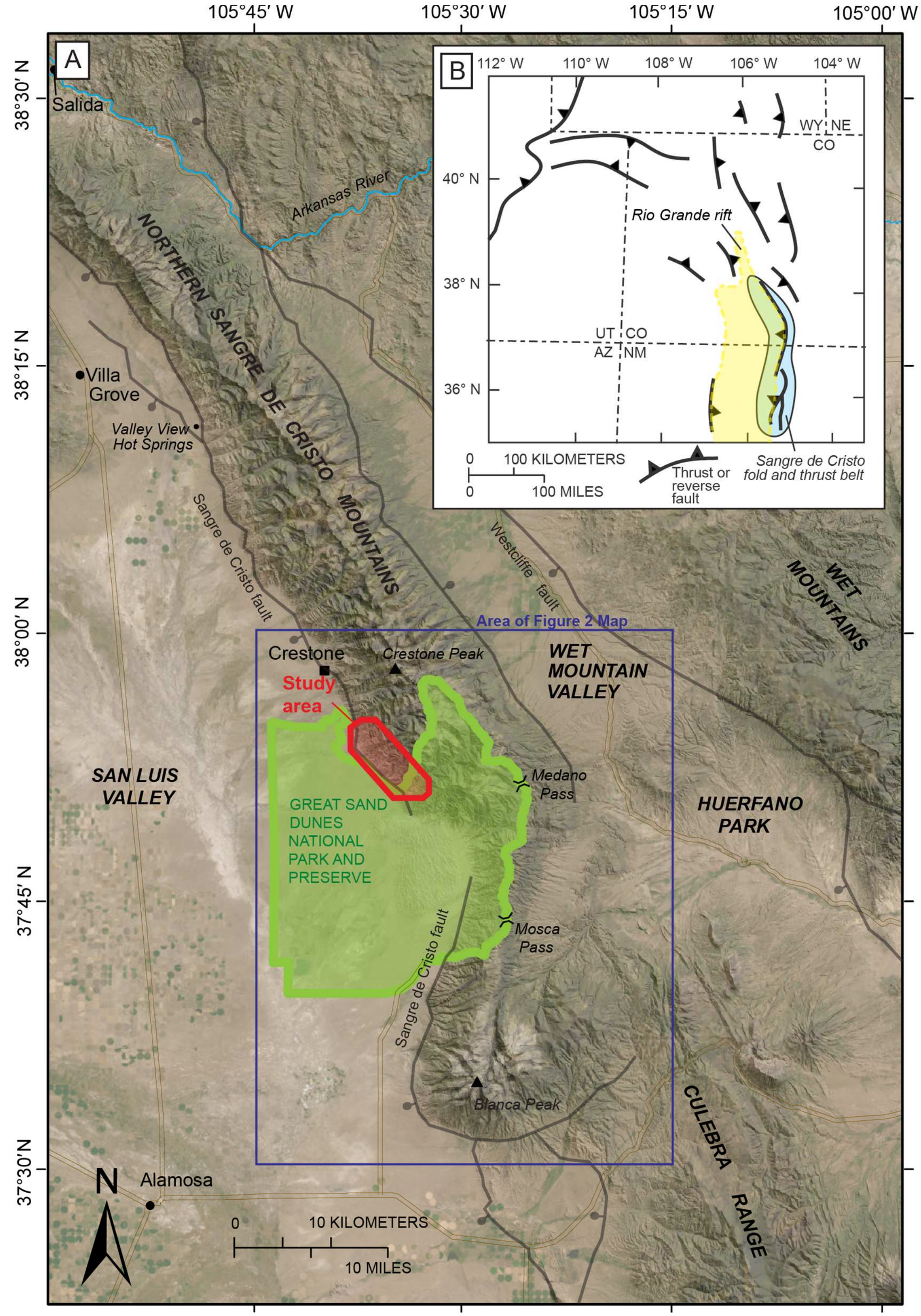

Figure 1: Overview map of the Sangre de Cristo Range. (a) Overview map of the Sangre de Cristo Range with hillshade and satellite imagery. Study area outlined in red, Great Sand Dunes National Park and Preserve outlined in green, and area of Figure 2 outlined in blue. Traces of major Rio Grande Rift-associated normal faults are shown in gray. (b) Simplified index map showing major Laramide thrust and reverse faults in CO, UT, AZ, and NM. Approximate extent of Rio Grande Rift structures in CO and NM shaded in yellow. The Sangre de Cristo Mountains are outlined in light blue. Modified from Lindsey and Caine (2024).

and narrow width are attributed to its origin as an extensional fault block, in which the Wet Mountain Valley and San Luis Valley dropped down relative to the Sangre de Cristo Range (Lindsey, 2010). Flatiron shaped features, called “faceted spurs” can be seen along the western range front, evidence of geologically recent normal fault offset. Numerous Quaternary fault scarps associated with the range-bounding Sangre de Cristo fault system exist on the eastern side of the San Luis Valley and on the flank of the Sangre de Cristo Range (McCalpin, 1981; Ruleman and Brandt, 2021; Hurtado and Gallen, 2024).

Eolian sand from the San Luis Valley collects against the western flank of the range (Figure 1a), and especially in the embayment to the NW of Blanca Peak, where it forms the prominent dune fields of Great Sand Dunes National Park and Preserve (Machette et al., 2007). Outside the boundaries of the National Park, the Sangre de Cristo National Wilderness encompasses most of the interior of the range. The land on the western and eastern flanks of the range is managed by the U.S. Forest Service (Rio Grande and San Isabel National Forests) with small sections of private land.

The study area for this project is located just north of Great Sand Dunes National Park on the western flank of the Sangre de Cristo Range and is delineated by a red polygon in Figure 1. Slopes along the range front in the study area are steep and rise from an elevation of 2,400 m (7,900 feet) on the alluvial plain of the San Luis Valley on the southwestern side of the study area to elevations of over 3,600 m (12,000 feet) on the northeastern side of the study area. Ephemeral creeks, including Deadman Creek, Alpine Creek, Pole Creek, Short Creek and Sand Creek, generally flow SW and form steep-walled valleys that serve as landmarks in the study area. With the exceptions of cliffs, some south-facing slopes, and areas above timberline, the study area is heavily vegetated with grass and sagebrush dominant at lower elevations (~8,000 feet), juniper and piñon dominant at moderate elevations (~8,500 feet), and denser coniferous and aspen forests dominant at high elevations below timberline (~9,500–12,000 feet; McCalpin, 1981).

Access to and use of this land for geological research is made possible through its federal designation as public land. However, the San Luis Valley and the Sangre de Cristo Range are the ancestral lands of the Ute, Navajo, Apache, Kiowa, and Comanche tribes. Spanish claims to the area began in 1598, leading to the establishment of long-standing Hispanic communities. Following the Treaty of Guadalupe Hidalgo in 1848, the land was ceded to the United States, and by 1858, Fort Garland had been constructed to support westward expansion under the ideology of Manifest Destiny: the belief that the U.S. was divinely destined to occupy the continent. Today, the region is a cultural palimpsest, shaped by the layered histories of indigenous nations, Spanish and Mexican settlers, and American expansionism. This complex human history parallels the region's geologic history, which also reflects successive phases of overprinting and deformation.

During the mining boom of the 1870s, vein-style gold and copper (Au-Cu) deposits were discovered along the western flank of the Sangre de Cristo Range (Benson and Jones, 1990; Clement, 1952; Johnson et al., 1984). Mining-related infrastructure, such as cabins, prospect pits, and structural remnants, are widespread throughout the study area, particularly in zones where mineral alteration is visibly concentrated along faults and shear zones. These historic features serve as evidence of early prospecting and mining activity driven by the pursuit of economic opportunity. Many of the prospect pits provide valuable bedrock exposures in otherwise poorly exposed terrain. The now-abandoned mining settlements of Duncan and Liberty, located within the study area, stand as historical remnants of this era of intensive mineral exploration.

1.2 Geologic Setting

The Sangre de Cristo Range records a multiphase deformation history that includes every major period of tectonism affecting the Rocky Mountain region. These events include Proterozoic shortening (Jones and Connelly, 2006), Pennsylvanian-Permian contraction and sedimentation associated with the Ancestral Rocky Mountains (ARM) (Hoy and Ridgway, 2002), Late Cretaceous shortening associated with the Laramide orogeny (Lindsey et al., 1984a), and finally middle to late Cenozoic extension and magmatism associated with the Rio Grande rift (Tweto, 1979). The approximate boundaries of the Rio Grande rift and the Sangre de Cristo Range are shown in Figure 1b, shaded in yellow and blue. This section briefly summarizes the tectonic evolution of the Sangre de Cristo Mountains, with emphasis on the geologic framework and previous research in the Deadman Creek thrust area. Figure 2 is a simplified geologic map of the region that shows the general structural geology of the Sangre de Cristo Range.

1.2.1 Proterozoic Basement Rocks

The oldest rocks exposed in the Sangre de Cristo Range are Paleoproterozoic igneous and metamorphic units, which are interpreted as products of crustal growth and deformation during the Yavapai (~1.8 Ga) and Mazatzal (~1.6 Ga) orogenies (Jones and Connelly, 2006). These events record the accretion of volcanic-arc terrains to the Archean Wyoming craton. The resulting crust is dominated by foliated gneiss, schist, and granitic units exposed in Rocky Mountain uplifts. The Proterozoic gneiss ranges in composition, reflecting variable protoliths of the rocks before metamorphism during the Mazatzal and Yavapai orogenies. The Sangre de

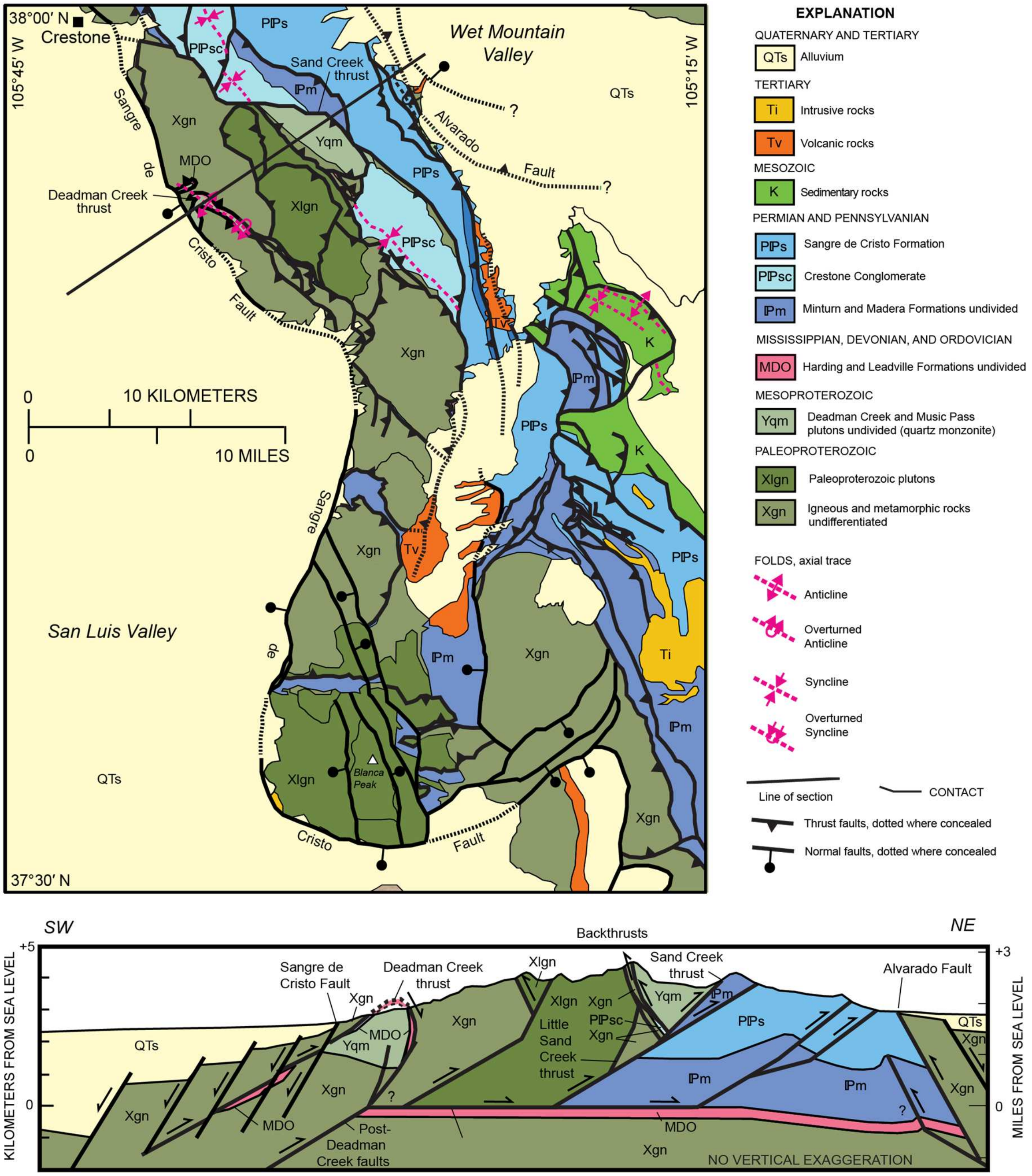

Figure 2: Simplified geologic map and cross section of the Sangre de Cristo Range. Simplified geologic map and schematic cross section showing general structural geology of the Sangre de Cristo Range near the Deadman Creek thrust. Modified from Lindsey and Caine (2024), B-B'.

Cristo Range also contains Paleoproterozoic (~1.7 Ga) quartzites which are interpreted to represent fluvial and shallow marine sedimentation in basins that developed during the time between the Yavapai and Mazatzal orogenies, possibly related to slab rollback and associated back-arc extension Jones and Connelly, 2006; Lindsey et al., 1986). Finally, the Music Pass quartz monzonite (~1.4 Ga) is a prominent Mesoproterozoic intrusive body located in the northern Sangre de Cristo Range. Previous researchers describe this unit as medium to coarse-grained with potassium feldspar megacrysts and plagioclase, quartz, and biotite (Jones and Connelly, 2006; Lindsey et al., 1986).

1.2.2 Paleozoic Sedimentation and Ancestral Rocky Mountains Deformation

Within the Rocky Mountain regions, a prominent nonconformity ("the Great Unconformity") separates the Proterozoic crystalline basement units from the overlying Paleozoic strata. This unconformity represents more than a billion years of missing time in the rock record, reflecting prolonged periods of erosion and non-deposition prior to the onset of widespread marine deposition during Paleozoic transgression. The Ordovician Harding Formation, Leadville Limestone, and other carbonate units in the map area are associated with this deposition. During the Pennsylvanian-Permian, the modern Sangre de Cristo Range was the location of the Central Colorado trough, a >4 km thick depositional basin that formed in response to Ancestral Rocky Mountain (ARM) uplifts (Lindsey et al., 1986a; Hoy and Ridgway, 2002). The Minturn and Sangre de Cristo formations were deposited in the Central Colorado trough and record evidence of high-energy sedimentation derived from the rapidly eroding Uncompahgre uplift to the southwest (Hoy and Ridgway, 2002). While ARM geologic structures are rarely preserved (Sweet and Soreghan, 2010), the Gibson Peak syncline and the Sand Creek thrust system (Figure 2) provide examples of syndepositional NE-SW shortening of ARM age (Hoy and Ridgway, 2002; Lindsey and Caine, 2024). These structures suggest that active deformation and sedimentation were coeval during the ARM tectonic regime. Some researchers (e.g., Lindsey et al., 1986b; Lindsey, 2010) have interpreted the Sand Creek thrust system as a continuation of the Deadman Creek thrust fault, on which this study is focused.

1.2.3 Mesozoic Tectonism: The Laramide Orogeny

The Laramide orogeny (~80–40 Ma) was the dominant Phanerozoic tectonic event across much of the Rocky Mountain region (e.g., Bush et al., 2016; Cather, 2004; Lindsey and Caine, 2024). Typically attributed to low-angle subduction of the Farallon Plate beneath North America, the Laramide orogeny produced widespread basement-involved uplifts, crustal shortening, and reactivation of older structural features (e.g., Weil and Yonkee, 2023). In the study area, WSW-dipping thrust and reverse faults on the southwestern flank of the Sange de Cristo Range, such as the Crestone thrust and the Deadman Creek thrust (Figure 2), likely accommodated Laramide shortening (Hoy and Ridgway, 2002; Lindsey, 2010). These faults may have reactivated or exploited pre-existing zones of weakness inherited from earlier ARM or Proterozoic structures. Mesozoic sedimentary units are locally preserved east of the Sangre de Cristo Range and record a transition from marine to fluvial environments, reflecting changing depositional regimes across the developing Laramide foreland (Bush et al., 2016). Much of the Mesozoic cover has since been removed by erosion and is not exposed in the study area; however, some Laramide age thrust faults along the eastern flank of the Sangre de Cristo Range (e.g., the Loco Hill thrust and JM thrust; Lindsey and Caine, 2024) involve Mesozoic units and thus unequivocally record Laramide shortening.

1.2.4 Cenozoic Evolution: Rift, Volcanism, and Glaciation

Following Laramide uplift, the region around the Sangre de Cristo Range underwent significant erosion, stripping much of the Mesozoic and Paleozoic cover (Cather, 2004; Bush et al., 2016; Abbott et al., 2022). In the late Eocene to late Oligocene, asthenospheric upwelling drove volcanism in the San Juan Volcanic Field. This ignimbrite "flare-up" deposited volcaniclastic sediments and thick ignimbrites across the region. One of the most voluminous eruptions, the Fish Canyon Tuff (~28 Ma), originated from the La Garita Caldera and is a major regional stratigraphic marker (Brister and Gries, 1994).

The “flare-up” volcanism overlaps in time with the beginning of extensional deformation associated with the Rio Grande rift, which began in the late Oligocene (~28–25 Ma). The rifting is marked by slip on approximately N-S to NW-SE normal faults, crustal thinning, and development of large structural basins such as the San Luis Valley and the Wet Mountain Valley (Wallace, 2004; Ricketts et al., 2016; Abbey and Niemi, 2020). Some minor intrusive magmatic bodies which may be related to rift-related magmatism have been identified in the Sangre de Cristo Range (Malavarca et al., 2023; Sitar et al., 2025).

The Sangre de Cristo fault system forms the western range-bounding structure of the Sangre de Cristo Range and defines the eastern margin of the San Luis Valley (Plate 1). This fault system dips moderately to steeply W to SW and cumulatively accommodates ~7–9 km of displacement, with the largest faults located several kilometers into the San Luis Basin (Brister and Gries, 1994; Kluth and Schaftenaar, 1994; Grauch et al., 2013). The main range-front strand of the Sangre de Cristo fault system is mapped along the western edge of the Sangre de Cristo Range (Ruleman and Brandt, 2021), though this strand likely does not accommodate the bulk of displacement and instead is on the order of tens to hundreds of meters in most places (Watkins, 1996). Quaternary fault scarps and faceted spurs along the western flank of the Sangre de Cristo Range provide evidence for geologically recent activity of range-bounding faults in the Sangre de Cristo fault system (Lindsey et al., 1984b; McCalpin, 1981; Ruleman and Brandt, 2021; Hurtado and Gallen, 2024).

Though not discussed in this study, alpine glaciation in Quaternary time sculpted the high peaks and valleys of the Sangre de Cristo Range. Features such as cirques, moraines, and U-shaped valleys are preserved in the high peaks of the study area and reflect multiple glacial episodes (McCalpin, 1981; Leonard et al., 2017; Ruleman & Brandt, 2021; Madole et al., 2008). Recent work suggests that deglaciation from the Last Glacial Maximum (LGM) resulted in accelerated post-LGM slip rates across the Sangre de Cristo fault due to a reduction of fault clamping stress (Hurtado and Gallen, 2024).

1.3 Prior Geologic Mapping

Geologic mapping of the Sangre de Cristo Mountains dates back to the Hayden Survey of 1877, which broadly identified metamorphic, "eruptive," and carboniferous rocks in the range (Hayden, 1877). The first detailed map of the western range front near the Deadman Creek thrust was produced by Jean F. Clement (1952), a Colorado School of Mines master's student, who mapped the area between south Crestone Creek and Pole Creek as part of a mineral survey of Luis Baca Grant No. 4.

In the 1980s, David Lindsey, Bruce Johnson, and others at the U.S. Geological Survey significantly expanded the mapped area of the Sangre de Cristo Range through reconnaissance-level geologic mapping at the 1:24,000 scale (Lindsey et al., 1984, 1985, 1986). These efforts culminated in the 1:62,500-scale geologic map by Johnson et al. (1987), which emphasizes mineral resources along the western flank of the range. While these maps provided comprehensive regional coverage and are an important basis for this study, they were not focused on detailed structural analysis. Some studies have built on this foundation by targeting specific time periods and structural elements. Jones and Connelly (2006) mapped selected areas of Proterozoic basement units near Music Pass and along the western flank of the range and dated several units using zircon U-Pb geochronology. Hoy and Ridgway (2002) investigated Paleozoic stratigraphy and Ancestral Rocky Mountain deformation. More recently, Lindsey and

Caine (2024) reexamined Ancestral Rocky Mountain and Laramide contractional structures across the range. McCalpin (1981) and Ruleman and Brandt (2021) contributed to understanding of Quaternary faulting and geomorphology in the San Luis Valley and the western flank of the Sangre de Cristo Range. Sitar (2023) and Sitar et al. (2025) documented the Independence Mine shear zone, located just north of the Deadman Creek thrust, providing new structural data that contributes to understanding the kinematic framework of the western Sangre de Cristo Range. A 2014 Colorado School of Mines MS thesis project (Weigel, 2014) presented brittle structural data from the Deadman Creek thrust area and evaluated the geometry of the Deadman Creek thrust. However, prior to our mapping project, no detailed geologic mapping and structural analysis systematically characterized the mylonitic shear zones in the Deadman Creek thrust area, leaving key questions about their geometry, kinematics, and tectonic evolution unanswered.

1.4 Research Goals and Relevance

The primary objective of this study was to produce a high-resolution (1:10,000 scale) geologic map of the bedrock in the Deadman Creek thrust area (Plate 1), located adjacent to Great Sand Dunes National Park and nearby the settlement of Crestone, CO on the western side of the San Luis Valley. Existing published maps of the region, such as those produced by Lindsey and colleagues in the 1980s, were generated at broader scales and lack the spatial resolution made possible by modern mapping techniques, including high-precision GPS, GIS mapping, lidar datasets, and high-resolution satellite imagery. Relatively little is currently known about the detailed geometry and kinematics of Laramide contractional structures in the Sangre de Cristo Range, as well as the early stages of Rio Grande rift extension. The increased detail in this study provides new insights into the tectonic history and deformation styles of the area. This mapping effort enables refined geologic characterization of the Deadman Creek thrust, evaluation of reactivation and overprinting relationships, and improved constraints on the timing and kinematics of fault systems and associated structures. These data contribute to a more comprehensive understanding of the tectonic evolution of the Sangre de Cristo Range and the broader processes controlling continental crustal deformation.

2. METHODS

The Deadman Creek thrust was characterized through 1:10,000-scale geologic mapping of a ~32 km^2 area (Plate 1), detailed structural data collection (Datasets 2, 3, & 4), and kinematic analysis of oriented samples (Dataset 5 & 6), including electron backscatter diffraction (EBSD) analysis of quartz. Structural relationships and lithologic units in the mapping area were further characterized with geochronological constraints provided by zircon U-Pb geochronology (Dataset 7). Field work was conducted in June 2023, May 2024, August-October 2024, and May 2025.

2.1 Geologic Mapping and Sample Collection

The primary objective of field work was to produce a detailed geologic map of the Deadman Creek thrust area and collect structural data. The mapping process includes detailed geometric analysis (strike and dip of planar features, trend and plunge of linear features), outcrop-scale kinematic analysis of brittle faults and mylonitic fabrics and observations of lithology and geologic relationships. Oriented and unoriented rock samples were collected where appropriate for further kinematic and geochronologic analysis of the study area. Structural data, field notes, photos, and samples were georeferenced to waypoints captured on a handheld GPS unit (Dataset 1).

Because of the ruggedness of the field area, we used an approach of recording notes, collecting samples, and measuring structural data while walking transects typically along NEtrending ridges and valleys. Streams in the field area were used as landmarks (Figure 3). We then interpolated map-scale features based on georeferenced field data integrated with analysis of satellite imagery and a high resolution lidar hillshade (i.e., "waypoint mapping"). During the mapping process, a total of 1707 geologic waypoints were recorded (Figure 4, Dataset 1), 129 samples were collected (Dataset 6), and 1044 raw structural orientations were measured (Dataset 2 & 4). The structural orientation data measured includes gneissic foliation, mylonitic foliation, mylonitic lineation, bedding, fault planes, and slickenlines. At exposures of small-scale fault planes, recorded data includes assessments of slip sense (if observable) with confidence values (0-3) assigned to each assessment. At exposures of mylonitic/sheared rocks, recorded data includes sense of shear (if observable) and associated kinematic indicators.

Structural data were collected in the field using primarily the *Stereonet Mobile* iPhone application (Allmendinger et al., 2017) and analog Brunton compasses. Manual calibration (i.e., confirmation that the compass measurement agrees with the iPhone measurement) of the *Stereonet Mobile* application was done prior to collecting data, as per the best practices outlined by Allmendinger et al. (2017).

Sampling for petrographic and/or microstructural analysis, lithologic description, geochronology, and electron backscatter diffraction (EBSD) was conducted throughout the study area. Oriented samples were collected primarily from mylonitic shear zones or brittle fault cores. Unoriented samples were collected at some locations for lithologic description. Bulk sampling (~3 liters of material) was conducted at several locations for mineral separation and zircon U-Pb

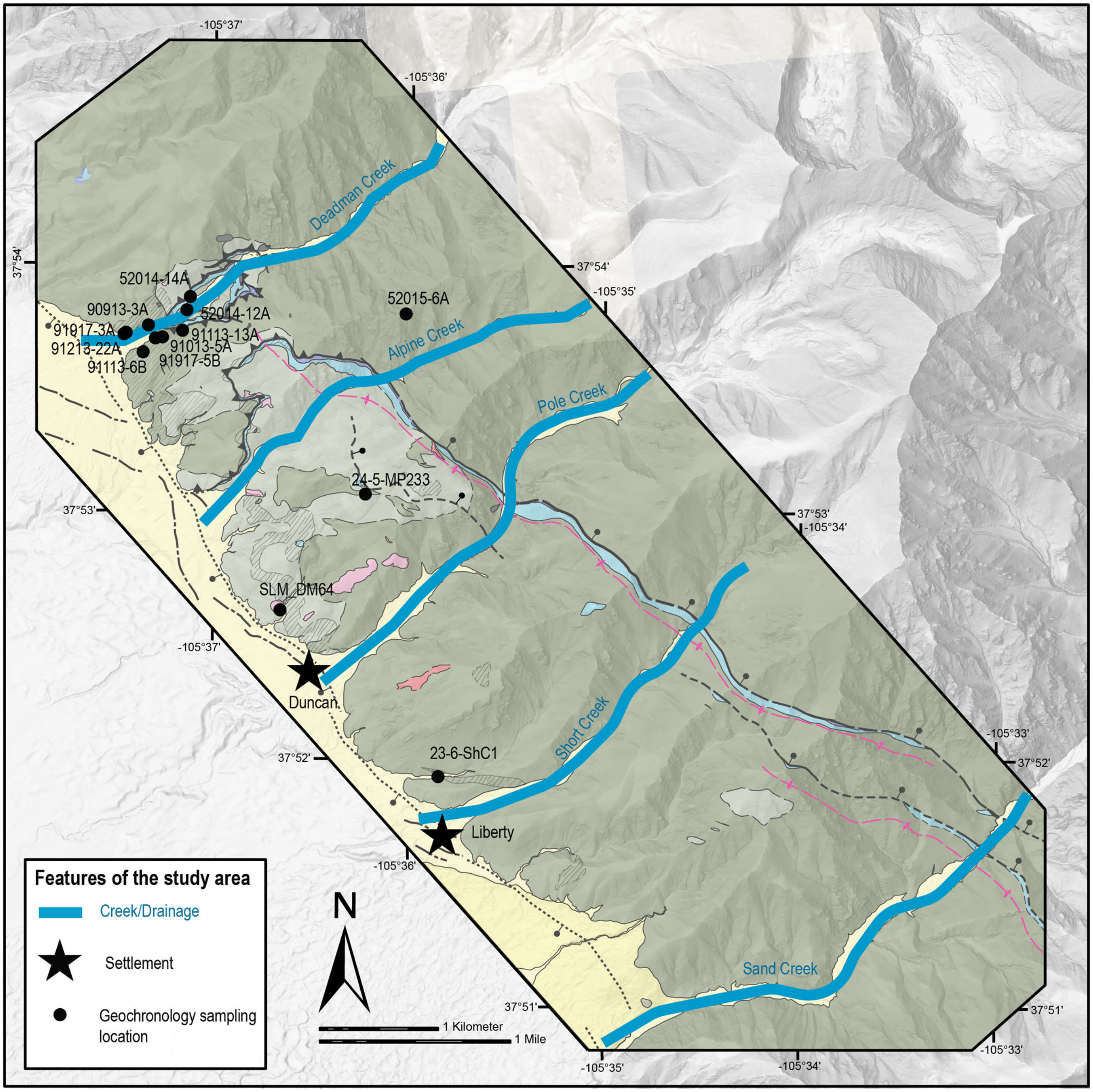

Figure 3: Simplified map of the Deadman Creek thrust area streams, settlements, and labeled geochronology sample conditions. Streams (teal) trend NE–SW across the study area. Black dots represent geochronology sample locations compiled from the USGS dataset as well as samples collected during this study. Black stars denote abandoned mining settlements, which serve as useful geographic landmarks.

geochronology using LA-ICP-MS. Information on each sample collected in the study area is available in Dataset 6.

2.2 Data Processing and Sample Preparation

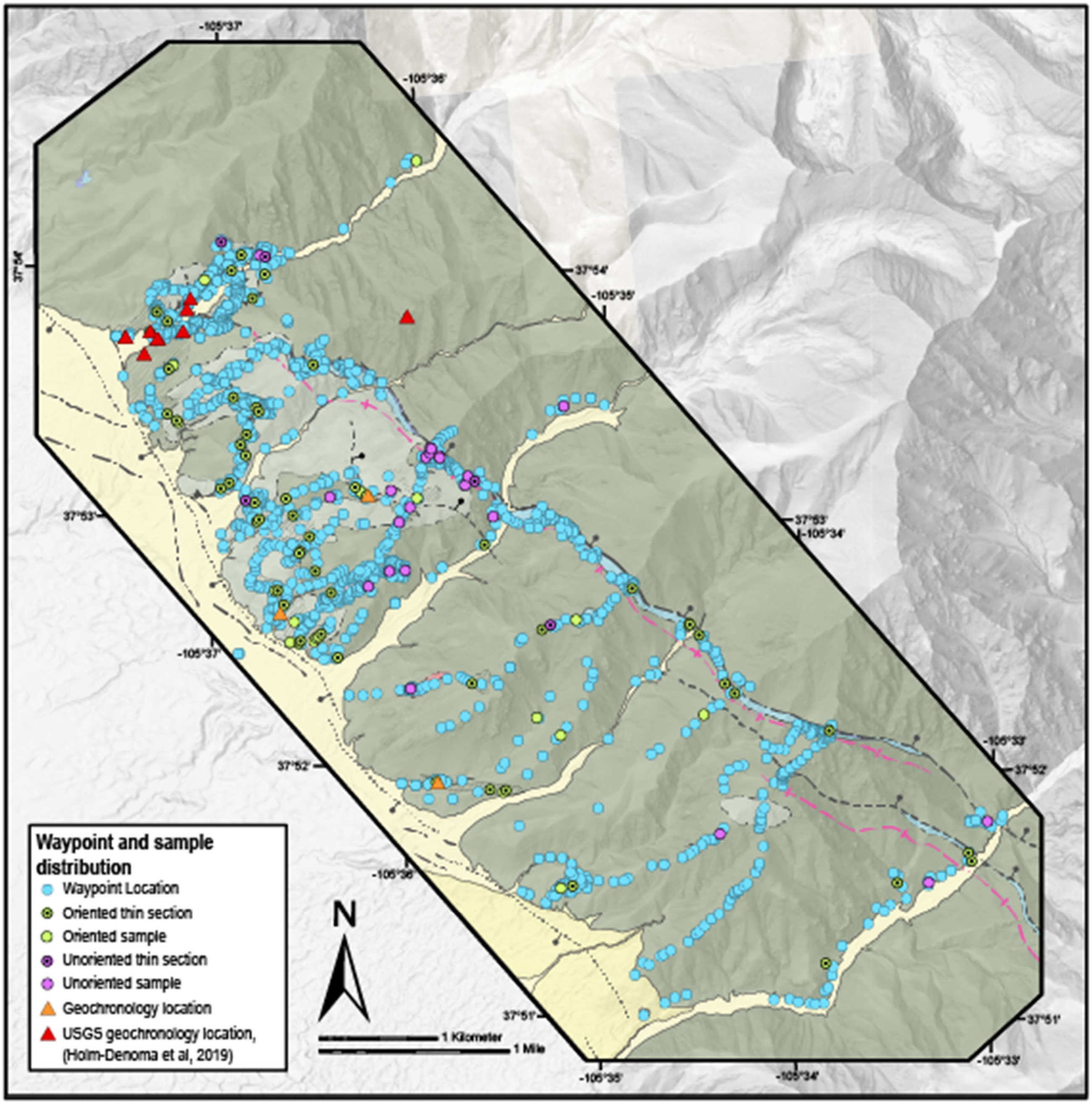

Figure 4: Simplified map of the Deadman Creek thrust area with waypoint and sample locations. Simplified geologic map (modified from Plate 1) showing waypoint and sample coverage within the study area, with types symbolically differentiated. All GPS waypoint locations are available in Dataset 1. Sample information is available in Dataset 6. Geochronologic analytical data is available in Dataset 7.

Following each field work trip, GPS waypoint location data, structural data, field notes, and sample information were organized and compiled. Field notes for were scanned and saved for reference, and selected samples were cut into thin sections for microstructural analysis or processed for geochronologic analysis.

All waypoints were assigned a unique waypoint ID depending on the date of the fieldwork and geologist recording the waypoint (i.e. for waypoint 24-10-MP1038, MP = Miriam Primus, 24 = year 2024, and 10 = October, and 1038 is the waypoint number, Dataset 1). Raw structural orientation data from each waypoint were compiled in a Microsoft Excel spreadsheet document (Dataset 2). The raw structural data were consolidated by calculating per-station, per-structure eigenvector best fit-solutions using the *Stereonet* desktop application (Allmendinger 2017) for waypoints with multiple measurements of the same structural features (bedding, gneissic foliation, mylonitic foliation) (Dataset 3). These "averaged" eigenvector best fit data were plotted on the map (Plate 1) and were used for geometric analysis of map-scale features in *Stereonet*. Eigenvector best-fit solutions were not calculated where orientations varied due to folding.

The main map product (Plate 1) for this study was constructed in *Adobe Illustrator* with geolocated waypoints and aerial imagery from *ArcGIS Pro*. A 1-m resolution DEM was built from lidar point-cloud files from in and around the study area (U.S. Geological Survey, 2021). A multidirectional hillshade layer was constructed using these DEMs in *ArcGIS Pro*. This hillshade serves as a basemap on the geologic map (Plate 1) and was referred to when interpolating contacts and structures between waypoints and field transects. A secondary hillshade with the illumination at azimuth 225° and elevation 35° was created to highlight fault scarps and alignments in the Quaternary sediments in the San Luis Valley on the western side of the range.

Oriented petrographic section billets were cut parallel to mineral lineations and perpendicular to foliations to obtain X-Z sections for microstructural study. Several non-oriented samples were cut into billets for lithologic analysis and unit description. Petrographic sections were prepared from the cut billets by Paula Leek Petrographics. A total of 69 thin sections were made from samples in the study area, 42 polished and 27 cover-slipped. Polished thin sections were prepared from billets that appeared viable for electron backscatter diffraction (EBSD) analysis of quartz or in-situ U-Pb monazite or zircon geochronology; covered thin sections were prepared from all other billets. Information on each thin section is available in Dataset 6.

2.3 Kinematic, Microstructural, and Geometric Analysis

Microstructural kinematic indicators (e.g., S-C fabrics, C' shear bands, brittle fracturing with rotation, recrystallized grain shape fabrics, mantled porphyroclasts) in oriented thin sections were documented and sense of shear was evaluated for each thin section. Assessments of microstructural kinematics were compiled with field observations of outcrop scale kinematics to show map-scale trends in sense of shear. In addition, each thin section of sheared rocks was evaluated and assigned a deformation category (1, 2, or 3) based on the relative deformation conditions represented primarily by quartz microstructures. Category 1 represents samples with brittlely deformed quartz or pressure solution of quartz. In many of these category 1 samples quartz also records sweeping extinction and minor subgrain development indicative of incipient crystal plastic deformation. This category correlates to overall lower deformation temperatures near or just below the brittle-plastic transition in quartz (~200–300°C, e.g., Stipp et al., 2002; Singleton et al., 2020). Category 2 correlates to moderate deformation temperatures characterized by plastically deformed quartz ribbons with bulging recrystallization, minor subgrain rotation recrystallization, and fractured feldspars characteristic of lower greenschist facies deformation conditions (~300–400°C). Category 3 correlates to samples with more pervasive dynamic quartz recrystallization primarily via subgrain rotation, characteristic of upper greenschist-facies deformation temperature (~400–550°C; e.g., Stipp et al., 2002). Where applicable, temperatures derived from c-axis opening angle (OA) thermometry were also used to assign categories to each sample (see section 2.4). Microstructural kinematics, deformation information, and other descriptive data for each oriented sample are available in Dataset 4.

Structural measurements were compiled, visualized, and analyzed using the Stereonet program (Allmendinger et al., 2017). Fault slip data were further evaluated using the Marrett and Allmendinger (1990) kinematic analysis method, which calculates P- and T-axes from measured fault planes and slip directions. These axes are interpreted as the incremental shortening (P) and extension (T) directions for each fault and were used to assess kinematic compatibility of fault populations and to approximate the overall paleostrain directions associated with brittle deformation.

2.4 Quartz Electron Backscatter Diffraction Analysis

For this study, thirteen relatively quartz-rich, polished, oriented petrographic thin sections from mylonitic samples from the Deadman Creek thrust were analyzed using electron backscatter diffraction (EBSD) analyses in collaboration with Dr. Jeffrey Rahl at Washington and Lee University in Lexington, Virginia. The thin sections were polished using colloidal silica, cleaned with isopropyl alcohol, and analyzed using a Zeiss EVO MA 15 Scanning Electron Microscope (SEM) operating in low vacuum at an accelerating voltage of 25kV, a probe current of 20-25 nA, and a working distance between 15- and 25-mm. Raster map step sizes between 0.5 and 20 microns were chosen on a sample-to-sample basis.

The EBSD data were analyzed on MATLAB using MTEX (Hielscher and Schaeben, 2008). During analysis, the crystallographic data were rotated and reflected, if needed, to align the trace of the foliation on the E-W axis of the pole figure and E/NE on the right of the plot. The

MTEX analysis also included a) extraction of crystal symmetry based on correlation measurements from the SEM software; b) filtering to remove low quality data based on a mean angular deviation (MAD) threshold; c) calculating individual quartz grains based on a 10° difference in crystal orientation; and d) merging of Dauphine twins and grains with subgrains into single grains. C- and a-axis pole figure plots (both for all grains and one point per grain), inverse pole figures, intensity spectrums, orientation distribution function pole figures (ODF), and c-axis opening angle (OA) and corresponding temperature calculations based on the Faleiros et al. (2016) empirical calibration were also created in the MTEX analysis. In this study, the c-axis opening angles were calculated using the method of Hunter et al. (2018), which determines the intensity of girdle maxima on the margin of the c-axis pole figure and uses the distance between the maxima to calculate an angle.

2.5 Geochronology

Two igneous bulk rock samples (23-6-ShC1 and 24-5-233b) were prepared for zircon U-Pb geochronology. In addition, one bulk rock sample (SLM_DM64) was used for apatite U-Pb geochronology. Mineral separation was done by GeoSep services in Moscow, Idaho. Zircons were mounted in epoxy and polished to expose the center of the grains. Zircon grains from sample 23-6-ShC1 were imaged using cathodoluminescence (CL) on the scanning electron microscope (SEM) at the USGS laboratories at the Denver Federal Center to document internal zoning patterns. Samples were then analyzed on the LA-ICP-MS at the CU TRaiL lab in Boulder, Colorado. This data was compiled with zircon U-Pb igneous and detrital zircon geochronology from USGS (Holm-Denoma et al., 2019) into a comprehensive geochronology dataset from the study area.

All U-Pb geochronology data were processed and visualized using the IsoplotR package (Vermeesch, 2018) in Rstudio (See supplementary material). The analytical data were imported as csv files, specifying the appropriate data format according to the ratio configuration (^{207}Pb/^{235}U vs. ^{206}Pb/^{238}U, ^{207}Pb/^{206}Pb vs. ^{238}U/^{206}Pb). All datasets were loaded with analytical uncertainties at 2σ confidence. For each sample, concordia diagrams and weighted mean plots were generated to evaluate the isotopic age data and calculate apparent ages. Concordia plots were produced using the concordia() function, applying either Wetherill or Tera-Wasserburg plot types (type = 1 or type = 2) depending on sample age. The plotted ellipses represent individual zircon or apatite analyses. Where necessary, data outside the expected discordance range were excluded using the discfilter() function to remove significantly discordant analyses or inherited grains. Weighted mean ages were calculated using the weightedmean() function, with Chauvenet's criterion enabled to identify and exclude statistical outliers. Analyses were plotted in ranked order of increasing age, and age uncertainties were reported at 2σ. For younger samples (<1100 Ma), the ^{206}Pb/^{238}U ages were used, while for older samples (>1100 Ma), the ^{207}Pb/^{206}Pb ages were used.

Detrital zircon datasets were plotted as kernel density estimate (KDE) age distributions using the kde() function in IsoplotR. Datasets were imported including ^{207}Pb/^{235}U, ^{206}Pb/^{238}U, and ^{207}Pb/^{206}Pb ratios with 2σ uncertainties. Analyses exceeding ±20% or <–5% discordance were removed prior to plotting. KDEs were generated emphasizing ^{206}Pb/^{238}U ages for grains younger than 1100 Ma and ^{207}Pb/^{206}Pb ages for older grains. All figures, including concordia, weighted mean, and KDE plots, were exported as high-resolution PDFs. Plot parameters such as axis limits, ellipse fill transparency, and concordia curve color were standardized for visual clarity.

3. RESULTS

2.6 Geologic Mapping and Field Relations

1:10,000-scale detailed field mapping of the Deadman Creek thrust has provided new information on lithologic units and structural geology in the region. The mapped area includes Proterozoic gneiss, Proterozoic quartzite, Mesoproterozoic quartz monzonite, Cambrian gabbro intrusions, Paleozoic sedimentary rocks, and Oligocene granodiorite, diorite, and aplite intrusions (Plate 1). Mylonite is also designated as a map unit, regardless of protolith. Each of these units are described below.

2.6.1 Proterozoic Crystalline Rocks

Proterozoic Gneiss (Xgn)

The dominant rock type in the mapping area is a heterogeneous complex of Proterozoic gneiss. While this gneissic unit is extremely variable in composition and texture, it occurs in two dominant varieties: dark-colored amphibole-rich gneiss (Figure 5a) and light-colored quartzofeldspathic gneiss (Figure 5b). The amphibole-rich variety is comprised of plagioclase, biotite, amphibole, ± secondary epidote and white mica. The quartzo-feldspathic variety contains quartz, plagioclase, ± secondary white mica, epidote, and chlorite. The gneiss represents the oldest Precambrian rocks in the Sangre de Cristo Range and serves as both the host rock for intrusive phases and the crystalline basement to the overlying Paleozoic sedimentary sequence. This unit is generally well-foliated with gneissic banding (Figure 5a), though some exposures of the quartzofeldspathic variety are weakly-foliated to massive (Figure 4b). This unit is locally chloritically altered, especially near the western range front.

Proterozoic Quartzite (Xq)

Multiple slivers of gray to pale blue, fine-grained, completely recrystallized, weathering-resistant quartzite are present throughout the mapping area. This unit has massive to poorly defined bedding (Figure 5c) and typically occurs in isolated pods and lenses within the Proterozoic gneiss (Plate 1), especially in the area around Deadman Creek. The unit is typically >90% quartz with a fine-grained white mica matrix, ± minor feldspar and iron oxides (Figure 6a). 1:10,000-scale mapping of the Proterozoic quartzite shows irregular contacts of the Proterozoic quartzite with the Proterozoic gneiss and relict bedding that aligns with the gneissic fabric. This unit may be mistaken for Paleozoic quartzite (i.e. the Ordovician Harding Formation, see section 3.1.3), but it is locally intruded by ~1.4 Ga Mesoproterozoic quartz monzonite (see subsequent section, Figure 5d) and lacks any stratigraphic relationship with the Paleozoic sedimentary rocks, providing constraints on its depositional age.

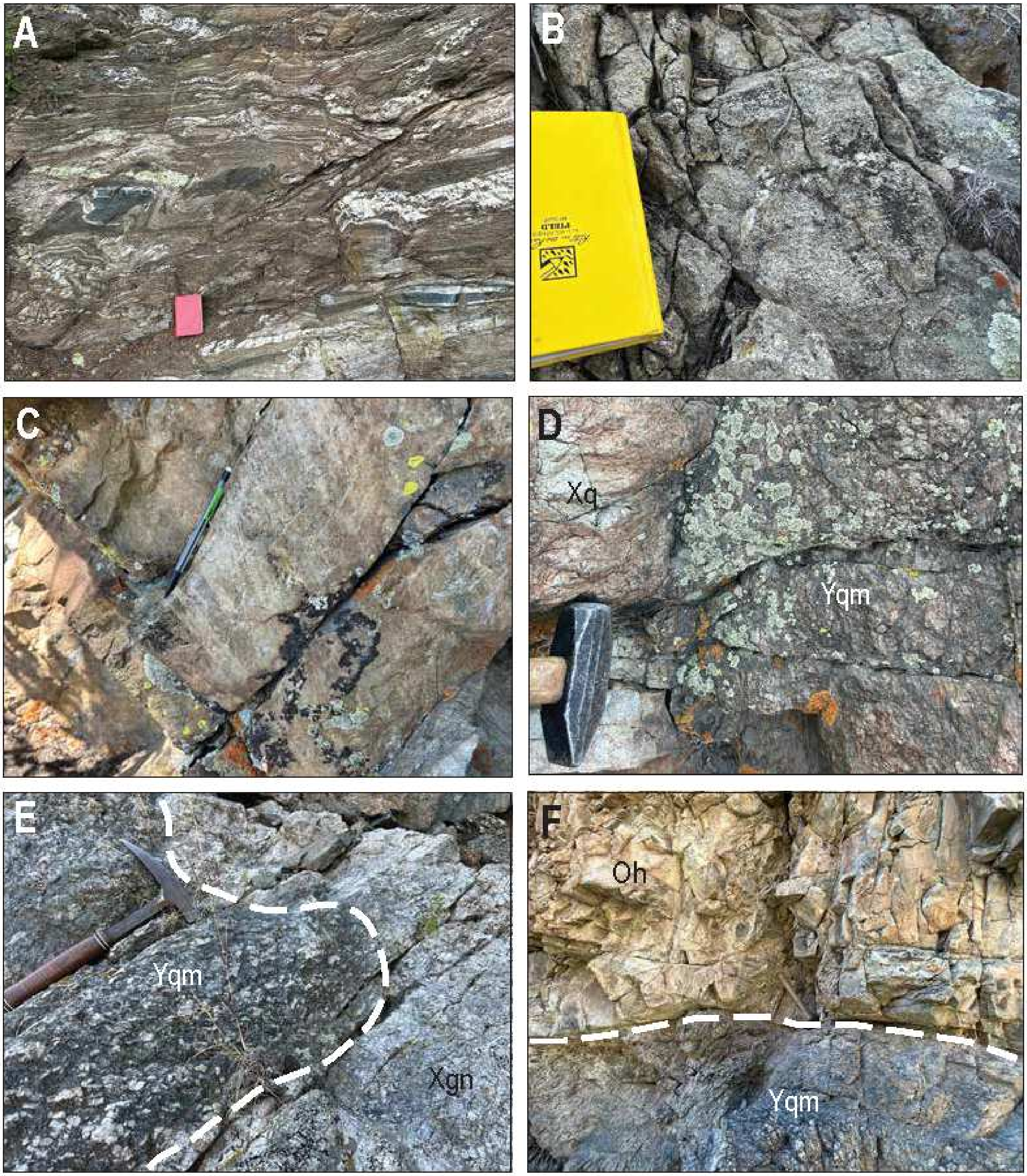

Figure 5: Representative outcrop photos from the study area. (a) Amphibolite-rich, banded Proterozoic gneiss (Xgn) exposed in the study area near Sand Creek; field notebook (~20 cm long) shown for scale. (b) Quartzo-feldspathic variety of Proterozoic gneiss (Xgn); field notebook (~20cm) shown for scale. (c) Proterozoic quartzite preserving faint bedding traces; pencil (~15 cm long) shown for scale. (d) Intrusive contact between Proterozoic quartzite (Xq) and Mesoproterozoic quartz monzonite (Yqm); rock hammer (~10 cm wide) shown for scale. (e) Intrusive contact between Proterozoic gneiss (Xgn) and Mesoproterozoic quartz monzonite (Yqm); rock hammer (~30 cm long) shown for scale. White dashed line delineates the contact. (f) Depositional contact between the Harding Formation (Oh) and Proterozoic gneiss (Xgn), representing the Great Unconformity; white dashed line delineates the contact.

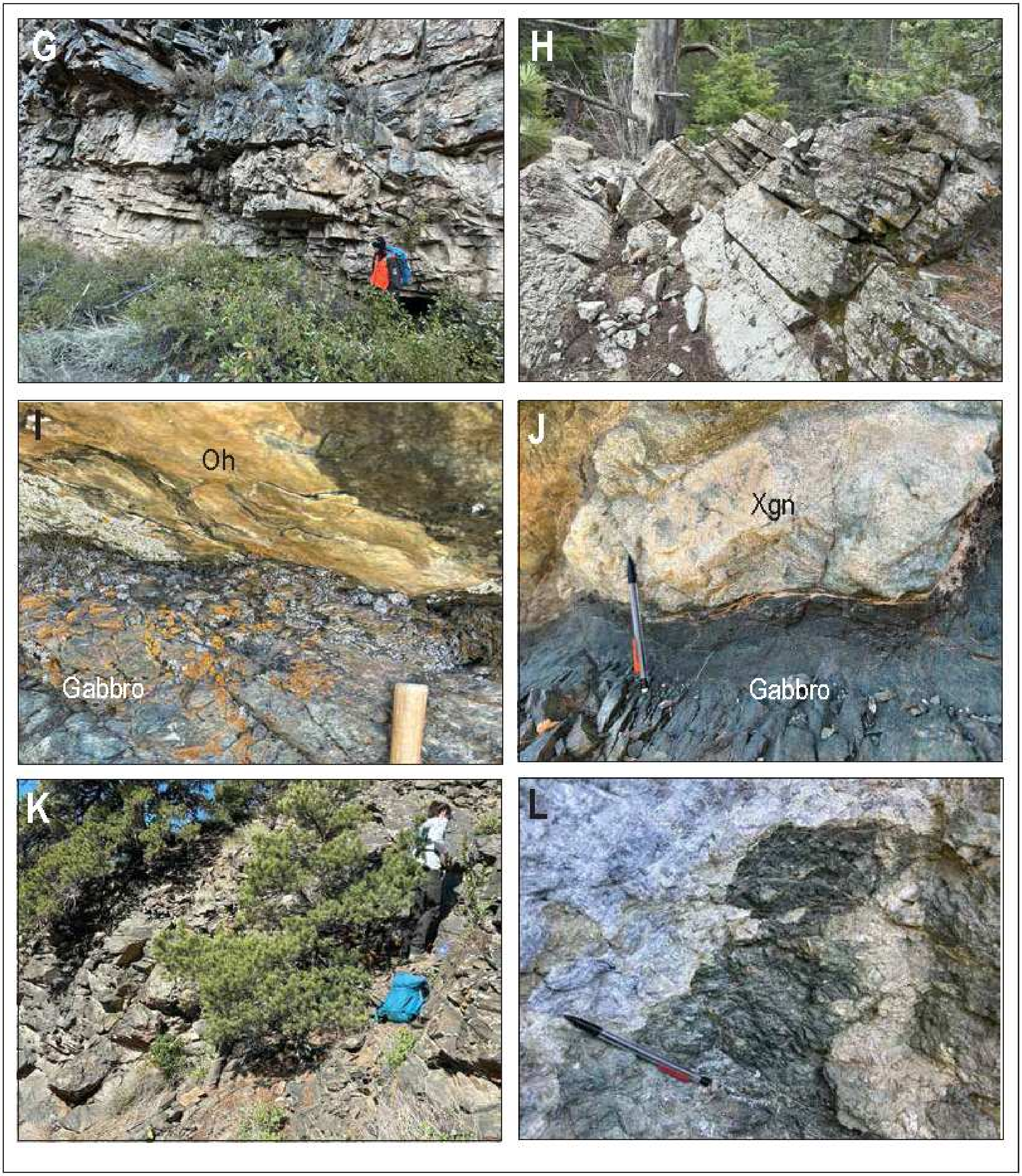

Figure 5 Cont: (g) Outcrop of bedded quartzite of the Harding Formation (Oh). (h) Well-bedded outcrop of the Mississippian-Devonian carbonates (MD). (i) Interpreted depositional contact between the Harding Formation (Oh) and Cambrian gabbro; hammer handle (~3 cm wide) shown for scale. (j) Intrusive contact between Cambrian gabbro and Proterozoic gneiss (Xgn); pencil (~15 cm long) shown for scale. (k) Outcrop of Cambrian gabbro unit. (l) Chloritic breccia in Proterozoic gneiss (Xgn) exposed near the mouth of Deadman Creek; pencil (~15 cm long) shown for scale.

Mesoproterozoic Quartz Monzonite (Yqm)

The Mesoproterozoic quartz monzonite is a gray to pinkish-brown, coarse-grained, intrusive unit, characterized by subhedral microcline crystals up to 3 centimeters in length. The unit is comprised of subequal amounts of quartz, potassium feldspar, ± secondary minor white mica, chlorite, and epidote. The quartz monzonite is prevalent throughout the study area, especially in the northern part of the map area, where it likely correlates to the ~1.4 Ga Music Pass pluton (1434 ± 2 Ma; Jones and Connelly, 2006). Intrusive and interleaved contacts between the Mesoproterozoic quartz monzonite, the Proterozoic gneiss, and Proterozoic quartzite are clearly visible in outcrop (Figure 5d & e) and on Plate 1. A prominent nonconformity exists between the quartz monzonite and the Ordovician Harding Formation (Figure 5f). The quartz monzonite is largely unfoliated, though weak foliation and protomylonitic textures are present locally. The unit commonly weathers to rounded boulders and blocky outcrops. A bulk geochronology sample of this unit from an outcrop along Deadman Creek yielded an LA-ICP-MS U-Pb zircon age of 1439 ± 13 Ma (Holm-Denoma et al, 2019, and see Figure 21e and section 3.5.1).

2.6.2 Paleozoic Intrusive Rocks

Cambrian Gabbro (€g)

Dark gray-green (weathered) and black (fresh) gabbroic dikes and bodies of various sizes (10s of meters up to 100s of meters wide, Plate 1) comprised of plagioclase, amphibole, and clinopyroxene ± secondary chlorite, epidote, and other phyllosilicates (Figure 6a) intruded the Proterozoic gneiss and Mesoproterozoic quartz monzonite (Figure 5j). These intrusions are fine- to medium-grained, generally massive, and weather to dark brown, blocky outcrops (Figure 5k). At one locality, this unit appears to be overlain unconformably by gently-dipping Ordovician

Harding Formation (Figure 5i, section 3.1.3). The contact between these units at that location is sheared and mylonitic fabrics are present in the quartzite. We did not observe the gabbro intruding the Paleozoic sedimentary units. The gabbro intrusive contacts with the crystalline basement units are irregular with chilled margins.

Gabbroic intrusions are especially concentrated in the footwall of the Deadman Creek thrust near the western range front in the northern part of the study area, though small exposures of gabbro are also present in the hanging wall of the thrust near Deadman Creek (Plate 1). While the gabbro is commonly unstrained, rare, altered portions have weakly developed shear fabrics. These include elongate amphibole crystals, aligned and sheared chlorite, and mylonitic lineations that trend eastward (Figure 8i). Based on field relations and LA-ICP-MS analysis of apatite grains from one gabbro sample (see section 3.5.2) we tentatively interpret the gabbro to be Cambrian age and associated with cryptic rifting in southern Colorado (e.g., Magnin et al., 2023). However, the gabbro is texturally and compositionally similar to a ~26 Ma gabbro exposed ~5 km to the northwest (Sitar et al., 2025). Given these conflicting data and ambiguous field relationships, the age of the intrusion is uncertain.

2.6.3 Paleozoic Sedimentary Rocks

As mentioned above, a regional nonconformity separates the Proterozoic crystalline basement from the Paleozoic sedimentary sequence (Figure 5f), which, in this study area, includes the Ordovician Harding Formation, the Devonian Fremont Dolomite, Mississippian Leadville Limestone, and the Pennsylvanian Minturn Formation. Collectively, the Mississippian, Devonian, and Ordovician units are referred to as MDO in this study and on older USGS maps. On Plate 1, the Ordovician Harding Formation (Oh) has been separated from the Mississippian and Devonian units (MD), where possible. The Pennsylvanian Minturn Formation (Pm) is also

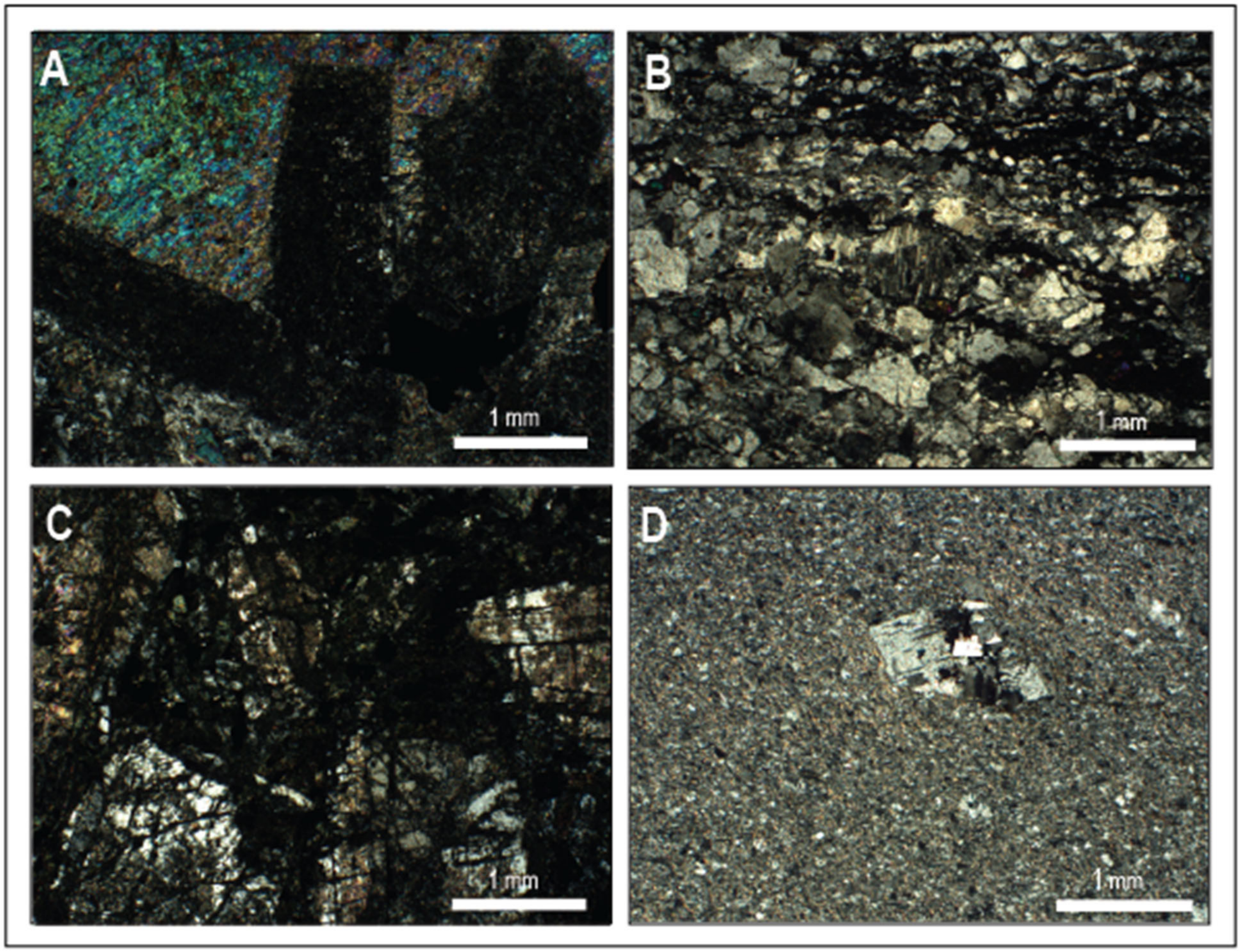

Figure 6: Photomicrographs of Cambrian and Oligocene intrusive rocks in the study area. Cross-polarized light (XPL) photomicrographs of intrusive igneous rocks from the study area illustrating primary igneous textures, alteration, and deformation-related microstructures. (a) Cambrian gabbro (sample 24-8-JS14) at 5x magnification. The rock is coarse grained and dominated by tabular, extensively altered plagioclase (~70%) and clinopyroxene (~25%), with minor quartz (~5%). Relict hornblende is locally preserved and there is pervasive alteration to chlorite and white mica. (b) Oligocene granodioritic intrusion (sample 23-6-ShC1a) at 5x magnification. The rock exhibits a protomylonitic to mylonitic fabric defined by fractured plagioclase, recrystallized quartz ribbons, and a fine-grained, dynamically recrystallized groundmass. Modal mineralogy is estimated as plagioclase (~45-50%), quartz (~25-30%), K-feldspar (~5-10%), and mafic minerals (~5-10%). Secondary chlorite, white mica, and epidote are abundant, and polyphase fine-grained aggregates record chemical breakdown of feldspar. (c) Oligocene diorite intrusion (sample 24-9-MP925) at 5x magnification. The rock is characterized by coarse-grained plagioclase feldspar with minor quartz (<5%), and mafic minerals that are now largely altered to chlorite and epidote. Extensive alteration of feldspar to white mica is present, and Fe-Ti oxides (locally needle-shaped, interpreted as ilmenite) occur within the matrix. Post-crystallization fractures cut primary grains. Modal mineral proportions are consistent with diorite, with dominant plagioclase feldspar and subordinate quartz. (d) Oligocene aplite intrusion (sample 24-5-MP233a) at 5x magnification. The rock is fine grained and composed primarily of quartz, feldspar, and white mica, with veins of coarser-grained quartz. Sparse feldspar phenocrysts are preserved.

delineated separately. The Paleozoic sedimentary section is typically thin in the study area (ranging from several meters to 10s of meters thick) and is truncated by the Deadman Creek thrust (see section 3.2.1), which is locally exposed as a subhorizontal to gently SW-dipping fault that juxtaposes the Proterozoic crystalline basement over the Paleozoic strata. Mylonitic foliation oriented parallel or at a low angle to bedding is common in the Paleozoic strata along the Deadman Creek thrust (Figure 15a, b, c, section 3.3.1).

Ordovician Harding Formation (Oh)

The Ordovician Harding Formation is a buff to light gray, fine-grained, strongly indurated and massive to well-bedded quartz arenite (Figure 5g). The unit is comprised of >90% well-sorted and sub-rounded to rounded quartz with minor feldspar and interstitial white mica (Figure 7b). Frequently, this unit contains a basal conglomeratic layer where it nonconformably overlies the Proterozoic basement rocks. 1:10,000-scale mapping in the Deadman Creek thrust area shows this unit as a moderately continuous alignment of outcrops with bedding typically striking NW-SE and dipping steeply to the NE or shallowly to the SW, depending on the location of the outcrop on either limb of the late-stage Laramide folds (see section 3.2.2). Some outcrops of the Harding Formation on the folded limb of the Deadman Creek thrust are overturned and dip to the SW, especially in the exposures just south of Pole Creek (Plate 1). In the Deadman Creek drainage, the Harding Formation is exposed in a gentle fold and dips shallowly to either the N-NE or S-SW. The Deadman Creek thrust and unconformity between the basement and Paleozoic strata is well exposed along the Deadman Creek canyon. The Harding Formation is conformably overlain by the Fremont Dolomite, Leadville Limestone, and other Paleozoic sedimentary rocks. This unit may be easily mistaken for the Proterozoic quartzite, but distinction can be made based on the presence of locally well-developed bedding, lesser degree of recrystallization, and conformable contact with overlying carbonate units, which are typically not present in the Proterozoic sequence.

Devonian Fremont Dolomite and Mississippian Leadville Limestone (MD)

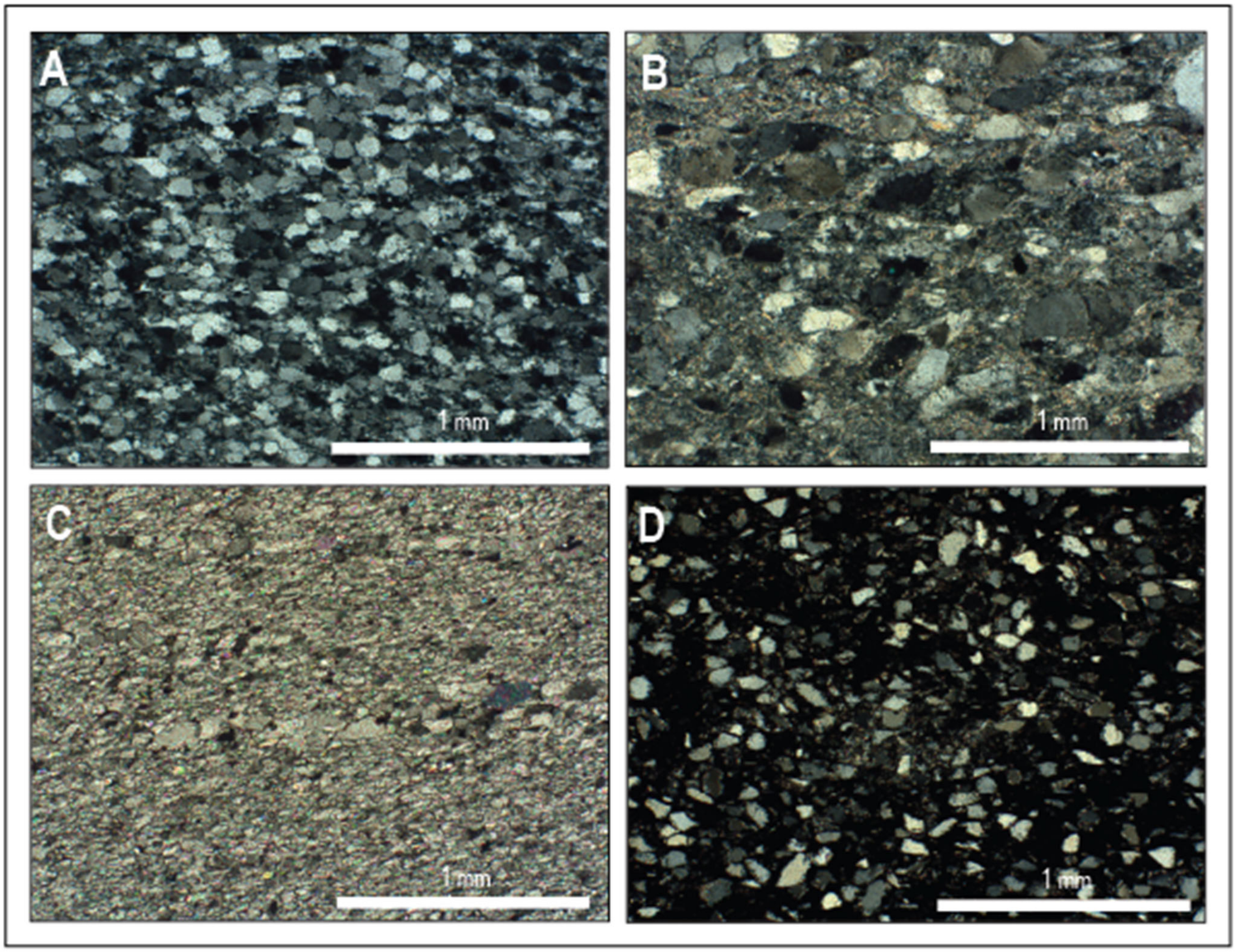

Figure 7: Photomicrographs of Paleozoic sedimentary rocks in the study area. Cross-polarized light (XPL) photomicrographs of sedimentary and metasedimentary rocks from the study area. (a) Proterozoic quartzite (sample 24-10-MP1113) at 5x magnification. The rock is composed predominantly of fine-grained quartz and exhibits incipient foliation and localized subgrain rotation (SGR) recrystallization. (b) Ordovician Harding Formation (sample 24-5-MP2-240c) at 5x magnification. Rounded to sub-rounded medium-grained quartz grains are supported by a fine-grained matrix dominated by white mica, which defines a weak foliation. (c) Leadville Limestone (sample 24-5-MP172) at 5x magnification. The rock consists of fine-grained, dynamically recrystallized polygonal calcite with a well-developed oblique grain-shape fabric. (d) Pennsylvanian Minturn Formation (sample 24-5-MP74a) at 5x magnification. Finely foliated, eye-shaped quartz grains within a dark, opaque matrix interpreted to consist of clay-rich and/or organic material. A weak foliation is defined by fine-grained white mica and pressure-solution seams. Sparse chloritoid is present in this sample.

As mentioned in the previous section, the Harding Formation is overlain by bedded carbonate units – predominantly presumed to be the Fremont Dolomite and Leadville Limestone (Figure 5h). These units are dark- to light-gray and sometimes tan to orange where altered and sheared. In thin section, samples of carbonate outcrops are comprised of >90% polygonal calcite (Figure 7b), typically devoid of fossils, and are fine- or medium-grained with variable thicknesses of bedding, ranging from massive to platy. The bedding is especially thin along the contact of these units with the Deadman Creek thrust, where they are commonly mylonitic and likely accommodated strain associated with the Laramide-associated NE-directed contraction. The package of Fremont Dolomite and Leadville Limestone is thin (<1 to 5 m thick) compared to the Harding Formation (up to 20 m thick), and it is inconsistently exposed along the trace of the Deadman Creek thrust.

Pennsylvanian Minturn Formation (Pm)

In a few areas along the steeply dipping to overturned folded limb of the Deadman Creek thrust (see sections 3.2.2 and 3.2.3) the base of the Pennsylvanian Minturn Formation is exposed stratigraphically above the carbonate units as thin (~1 to 3 m thick) intervals of orange to gray, slaty to phyllitic fine-grained clastic rock comprised of subangular to rounded quartz clasts, organic matter, and rare chloritoid (Figure 7d). Metamorphic chloritoid is characteristic of the lower Minturn Formation in some other areas in the Sangre de Cristo Range, such as along Crestone Creek (Lindsay et al., 1986a). The exposures of the Minturn Formation represent the uppermost Paleozoic sedimentary unit in the study area and records mylonitic to brittle-plastic strain where it is sheared along the Deadman Creek thrust and Short Creek fault system. Previous maps of this area of the Sangre de Cristo Range do not show the Minturn Formation.

2.6.4 Paleogene Intrusive Rocks

Granodiorite dikes (Tgd)

White to light-green, finger-like granodiorite bodies comprised of plagioclase, quartz, minor potassium feldspar ± secondary calcite, chlorite, and white mica (Figure 6b) occur in at least one locality in the mapping area in a drainage just north of Short Creek (Plate 1). Few original igneous mafic minerals are preserved in this unit at this location. These medium- to fine-grained phaneritic dikes intrude into the quartzo-feldspathic variety of Proterozoic gneiss and have mylonitic to protomylonitic foliation striking predominately NW-SE and dipping gently to the SW, with top-SW shear sense indicators . Pervasive chlorite alteration makes the intrusive contacts of this unit difficult to delineate, but field observations suggest thin and elongate intrusion geometries. An LA-ICP-MS igneous zircon analysis of this unit gives a crystallization age of ~28 Ma, indicating emplacement in the Oligocene (section 3.5.1). Additional granodioritic intrusive bodies are likely present in the area but were not mapped during this study.

Diorite Intrusions (Td)

Isolated and irregularly-shaped, dark gray-green to black porphyritic dioritic intrusions (Td) up to ~400 m wide occur in several localities throughout the mapping area (Plate 1). These bodies are recognizable by their tabular plagioclase phenocrysts (up to ~1 cm in length), altered mafic minerals (likely clinopyroxene) ± secondary chlorite and epidote (Figure 6c). The mapped intrusions, interpreted as stocks at depth, form outcrops 10s of meters wide. Contacts are discordant to gneissic foliation and occasionally show chilled margins. Although no geochronologic data is available, they intrude into the Proterozoic gneiss and are unstrained. An Oligocene age is assumed, consistent with other most intrusions in the study area, except the possible Ordovician-Cambrian gabbro bodies (see section 3.5.3). Because the diorite units are scattered across an approximately ~3 km wide area within the map (Plate 1), it is possible that they are connected at depth as part of a larger subsurface body. The distribution of exposed diorite intrusions suggests the presence of additional, unexposed or unmapped bodies at depth or in poorly exposed areas.

Aplite Intrusions (Ta)

Light-colored aphanitic to porphyritic aplite dikes, composed mainly of fine-grained quartz, plagioclase, and k-feldspar are abundant throughout the study area (Figure 6d). The aplite dikes are typically <1 m wide tabular bodies that crosscut almost every other lithologic unit in the field area (Plate 1). Typically, these dikes are oriented parallel to the NW-SE trend of the range. While they may resemble fine-grained quartzite in the field, their aphanitic texture, presence of tabular euhedral K-feldspar grains and intrusive contacts distinguish these aplite dikes from other units in the mapping area. A sample from an aplite dike (24-5-MP233b) yielded a U-Pb zircon age of ~26 Ma, similar to several ages obtained by Holm-Denoma et al (2019) of the same aplite unit (section 3.5.1). The mapped aplite intrusions represent the most prominent exposures within the study area, but additional aplite dikes are likely present.

2.6.5 Mylonite

A mylonite unit is delineated on the geologic map (Plate 1) by a diagonal linear pattern and is most prominent along the western range front, although smaller bodies occur elsewhere throughout the study area, and narrow mylonite zones are localized along the Deadman Creek thrust in some areas. The unit locally incorporates deformed Oligocene granodiorite intrusions (section 3.1.4). However, the mylonite is crosscut by younger Oligocene aplite dikes (section 3.1.4), indicating that mylonitic deformation predates these felsic intrusions. A particularly large and continuous body of mylonite along the western range front is here termed the Duncan shear zone (discussed further in section 3.2.4).

2.7 Structural Relationships

Field mapping and structural data collection in the Deadman Creek thrust area has refined interpretations of previously mapped geologic structures in the study area and identified several previously unrecognized structural features. The geological features discussed in this section include the Deadman Creek thrust, NE-vergent folds that involve the Deadman Creek thrust, a newly-identified mylonite zone referred to as the Duncan shear zone, a newly-identified brittle-plastic set of faults referred to as Short Creek fault system, and the Sangre de Cristo fault system. These structures record a complex deformational history that reflects both contractional (Laramide) and extensional (Rio Grande rift) tectonic events. The following sections describe the structural features in detail, including geometric and kinematic data.

2.7.1 Deadman Creek thrust

The Deadman Creek thrust is the primary contractional structure in the study area and represents a significant structural boundary between the Proterozoic crystalline basement in the hanging wall and Paleozoic strata (MDO) in the footwall (Plate 1). The Deadman Creek thrust generally dips shallowly to the W or SW or is subhorizontal (e.g., along Deadman Creek), except where it is interpreted to be folded (see cross sections on Plate 1 and section 3.2.2). Displacement along the Deadman Creek thrust and most other contractional structures in the range is NE to ENE-directed (e.g., Lindsey and Caine, 2024). The northernmost exposure of the Deadman Creek thrust is in a structural window north of Deadman Creek, mapped by Sitar et al. (2025) (see also Sitar, 2023), where the MDO strata are exposed underneath the overlying basement. The southernmost mapped exposure of the Deadman Creek thrust occurs near Sand Creek, where the Proterozoic gneiss and MDO are juxtaposed along a subvertical folded limb of the thrust.

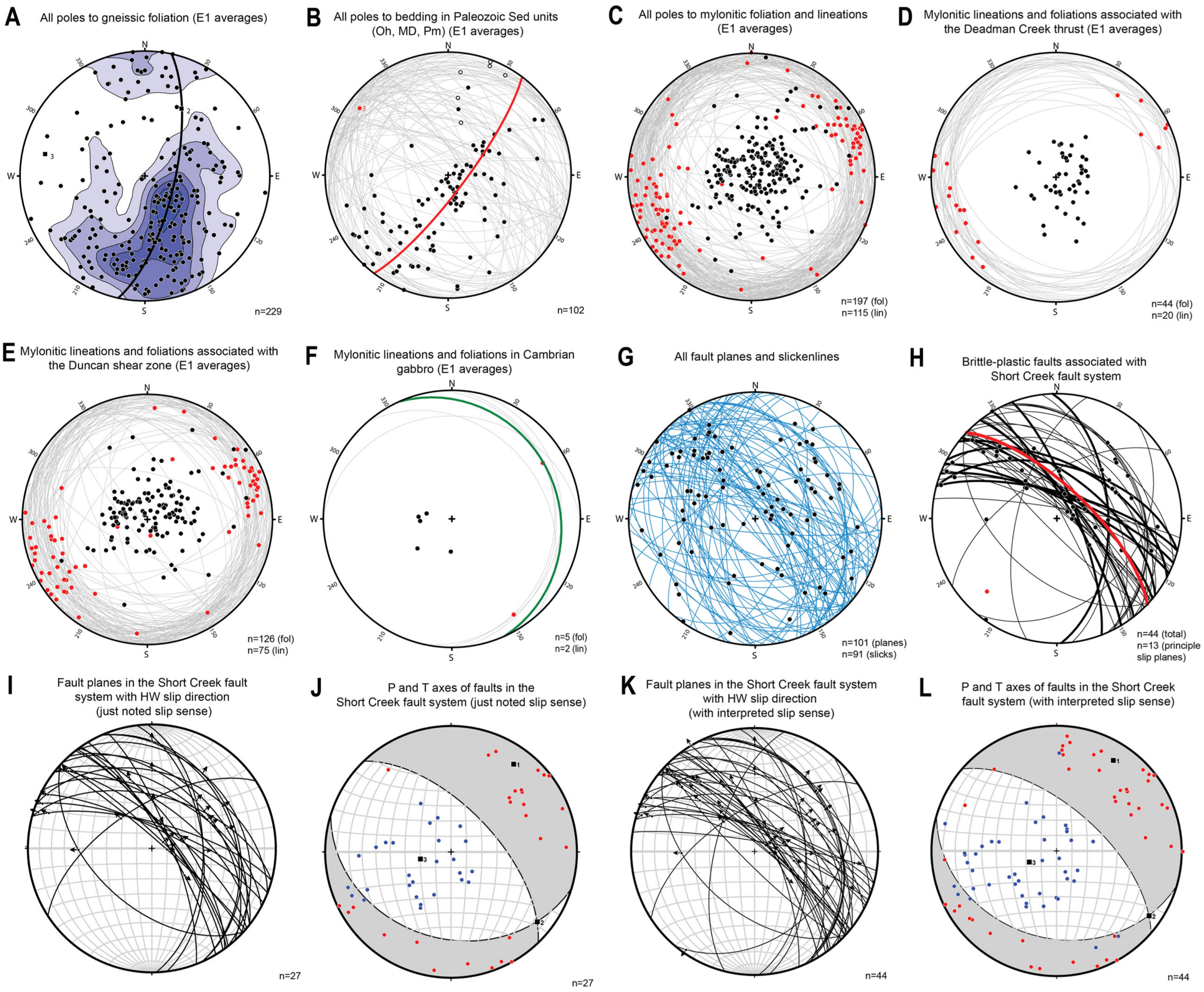
A
All poles to gneissic foliation (E1 averages)
n=229
B
All poles to bedding in Paleozoic Sed units (Oh, MD, Pm) (E1 averages)
n=102
C
All poles to mylonitic foliation and lineations (E1 averages)
n=197 (fol)
n=115 (lin)
D
Mylonitic lineations and foliations associated with the Deadman Creek thrust (E1 averages)
n=44 (fol)
n=20 (lin)
E
Mylonitic lineations and foliations associated with the Duncan shear zone (E1 averages)
n=126 (fol)
n=75 (lin)
F
Mylonitic lineations and foliations in Cambrian gabbro (E1 averages)
n=5 (fol)
n=2 (lin)
G
All fault planes and slickenlines
n=101 (planes)
n=91 (slicks)
H
Brittle-plastic faults associated with Short Creek fault system
n=44 (total)
n=13 (principle slip planes)
I
Fault planes in the Short Creek fault system with HW slip direction (just noted slip sense)
n=27
J
P and T axes of faults in the Short Creek fault system (just noted slip sense)
n=27
K
Fault planes in the Short Creek fault system with HW slip direction (with interpreted slip sense)
n=44
L
P and T axes of faults in the Short Creek fault system (with interpreted slip sense)
n=44
N
E
S
W
30
60
120
150
210
240
300
330
1
2
3

Figure 8: Lower-hemisphere, stereonet projections summarizing structural orientation data from the study area. (a) Poles to gneissic foliation measured in Proterozoic crystalline rocks (primarily Proterozoic gneiss and Mesoproterozoic quartz monzonite). A total of 372 foliation planes were measured across the study area (Dataset 2) and averaged by outcrop (using eigenvector 1 to poles) to yield 229 foliation measurements (Dataset 3). The poles define an approximate girdle distribution with a mean orientation of 171°/45° (eigenvector 1), indicating folding of the gneiss about an axis plunging gently to the northwest, represented by eigenvector 3 (282°/20°, black square). The distribution and mean orientation are comparable to poles to gneissic foliation reported north of the study area by Sitar et al. (2025), although foliation adjacent to the Deadman Creek thrust is generally steeper. The complexity of the pole distribution suggests polyphase deformation of the Proterozoic basement. (b) 132 bedding planes were measured in the Paleozoic strata in the study area (Dataset 2), with most measurements taken from the Ordovician Harding Formation and the Devonian and Mississippian carbonates. Bedding planes measured on the same outcrops were averaged (using eigenvector 1 to poles) for a total of 102 condensed bedding measurements (black circles) including 7 overturned bedding planes (hollow circles) (Dataset 3). The poles to bedding define a girdle distribution corresponding to a fold axis (eigenvector 3, red circle) oriented 307°/11°. The overall orientation and folding of bedding is consistent with NE-vergent folding. The cylindrical best fit great circle is shown in red. Measured bedding planes are shown in light gray. (c) Poles to mylonitic foliation (black circles) and corresponding lineations (red circles) measured throughout the map area. In total, 277 mylonitic foliation planes and 149 mylonitic lineations were measured (Dataset 2) and averaged by outcrop to produce 197 foliation and 115 lineation measurements (Dataset 3). Measured foliation planes are shown in light gray. (d) Poles to mylonitic foliation (black points) and corresponding lineations (red points) measured within 10 meters of the Deadman Creek thrust fault. This dataset includes 44 mylonitic foliation planes and 20 mylonitic lineations. Measured foliation planes are shown in light gray. The orientation pattern closely resembles that of the broader mylonitic dataset shown in (c). (e) Poles to mylonitic foliation (black points) and corresponding lineations (red points) measured within or associated with the Duncan shear zone. This dataset includes 126 mylonitic foliation planes and 75 mylonitic lineations. Measured foliation planes are shown in light gray. The orientation pattern closely resembles that of the broader mylonitic dataset shown in (c). (f) Mylonitic foliation and lineation measured in the Cambrian gabbro unit. 5 mylonitic foliation planes and 2 associated lineations were measured. Foliation planes are shown as light gray great circles, corresponding poles to foliation are shown as black points, and lineations are shown as red points. The green great circle represents the plane defined by the maximum eigenvector (eigenvector 1), corresponding to the average orientation of the measured foliation planes. (g) All measured fault planes in the study area. A total of 101 fault planes are plotted as blue great circles, and 91 associated slickenside lineations are shown as black points. The distribution of fault-plane and slickenline orientation shows the range of brittle fault geometries recorded across the study area. (h) Fault plane and slickenline orientations associated with the Short Creek fault system. A total of 44 fault planes are plotted as black great circles, including 13 measurements from the principal slip surface shown as bold great circles. 42 associated slickenside lineations are plotted as black points. The red great circle represents the plane defined by the maximum eigenvector (red point, 224°/20°) to the principal slip surface measurements. The distribution of fault planes indicates a dominantly steep northeast-dipping fault geometry for the Short Creek fault system. (i) Fault planes associated with the Short Creek fault system plotted with hanging wall (HW) slip directions derived from observed kinematic indicators. A total of 27 fault planes with directly noted slip sense are included. The hanging wall slip directions are dominantly normal, NE-down dip-slip motion, with a minor component of left-lateral slip. (j) P– and T-axes (interpreted as shortening and extension axes, respectively) calculated from fault-plane solutions for faults associated with the Short Creek fault system using only faults with observed slip sense (n = 27). P-axes are shown in blue and T-axes in red. The orientations of the principal axes reflect the strain regime responsible for faulting within the Short Creek fault system. Linked Bingham axes define a mean extension direction of 35°/16° (1) and a mean shortening direction of 258°/70° (3). The corresponding fault-plane solution compatible with these axes is shown. (k) Fault planes associated with the Short Creek fault system plotted with hanging-wall (HW) slip directions, including both faults with observed kinematic indicators and faults for which shear sense was interpreted where direct slip indicators were absent. A total of 44 fault planes are included in this plot. The combined dataset provides a more complete representation of fault kinematics within the Short Creek fault system. (l) P- and T-axes calculated from fault-plane solutions for faults associated with the Short Creek fault system, including faults with interpreted slip sense where direct observations of slip were not recorded in the field. The plot includes solutions derived from 44 fault planes. P-axes are shown in blue and T-axes in red. Linked Bingham axes define a mean extension direction of 32°/16° (1) and a mean shortening direction of 249°/71° (3). The corresponding fault-plane solution compatible with these axes is shown.

The geometry and thickness of the footwall MDO package are highly variable along the Deadman Creek thrust. In some localities, the thrust completely cut out the Paleozoic strata, placing basement rocks directly over other basement units with a narrow (~2–3 m thick) zone of mylonite/protomylonite defining the thrust. Elsewhere, as in Deadman Creek, the MDO package is preserved as a continuous sequence up to approximately 60 meters thick (Figure 9b). The Deadman Creek thrust zone is characterized primarily by mylonite and local cataclasite. Along the western flank of the range the thrust spatially overlaps with mylonitic fabrics associated with the top-SW directed Duncan shear zone (see section 3.2.4). The most clearly developed mylonitic fabrics associated with the top-NE thrust-related shear are located in the footwall, particularly in carbonate strata likely derived from the Leadville Limestone. Near the northeastern exposure of the thrust in Deadman Creek, mylonitic fabrics with top-ENE-directed shear are concentrated in a ~5 m thick zone of calcareous mylonite directly below the thrust, whereas Harding Formation below record little to no penetrative strain. In some localities, the mylonitic fabric is also developed in the hanging wall basement units, particularly the Mesoproterozoic quartz monzonite, where recrystallized quartz ribbons and fractured feldspar porphyroclasts show protomylonitic textures (section 3.3.3, Figure 11). The intensity of mylonitic fabric in the crystalline rocks of the hanging wall is generally weaker and more discontinuous compared to the mylonitic MDO in the footwall.

Mylonitic fabrics that are most spatially associated with the Deadman Creek thrust (within 10 m from the thrust) are overall subhorizontal with shallowly NE-SW to E-W plunging lineations (Figure 8d). The mylonitic foliation and lineation orientations associated with the Deadman Creek thrust do not vary significantly from the broad patterns of mylonitic foliation and lineation across the map area (Figure 8c).

While the geometry of the Deadman Creek thrust is defined by top-NE directed contraction likely associated with the Laramide orogeny, kinematic indicators along the thrust display both top-NE and top-SW shear sense indicators. Most of the top-NE shear sense occurs in the Paleozoic carbonates (Leadville Limestone), while dominant top-SW directed shear is more common in the mylonitic fabrics of the Harding Formation as well as in the crystalline basement units. The predominance of top-SW shear sense is consistent with the kinematic patterns across the entirety of the mapping area (see section 3.3, Figure 16) and may be a function of the proximity to the Duncan shear zone (described in section 3.2.4).

Displacement on the Deadman Creek thrust must be at least equal to the map-view distance of basement transported over the MDO in the slip direction, which reaches a maximum of approximately 1.5 km in the Alpine Creek area and provides a reasonable minimum displacement estimate. The total slip may not be substantially greater than this value based on several lines of evidence. Similar basement lithologies above and below the thrust, such as the presence of Cambrian gabbro on both sides, suggest limited thrust displacement. This interpretation is also supported by our detailed mapping that reveals a more continuous distribution of basement units than shown in previous USGS maps, which often separate the Mesoproterozoic quartz monzonite and Proterozoic gneiss across the fault. Additionally, in areas not overprinted by the Duncan shear zone, such as east of Alpine Creek and along the eastern side of Deadman Creek, the thrust zone is narrow and consists of only a few meters of mylonitic rock, inconsistent with major (i.e., several km) displacement along the thrust.

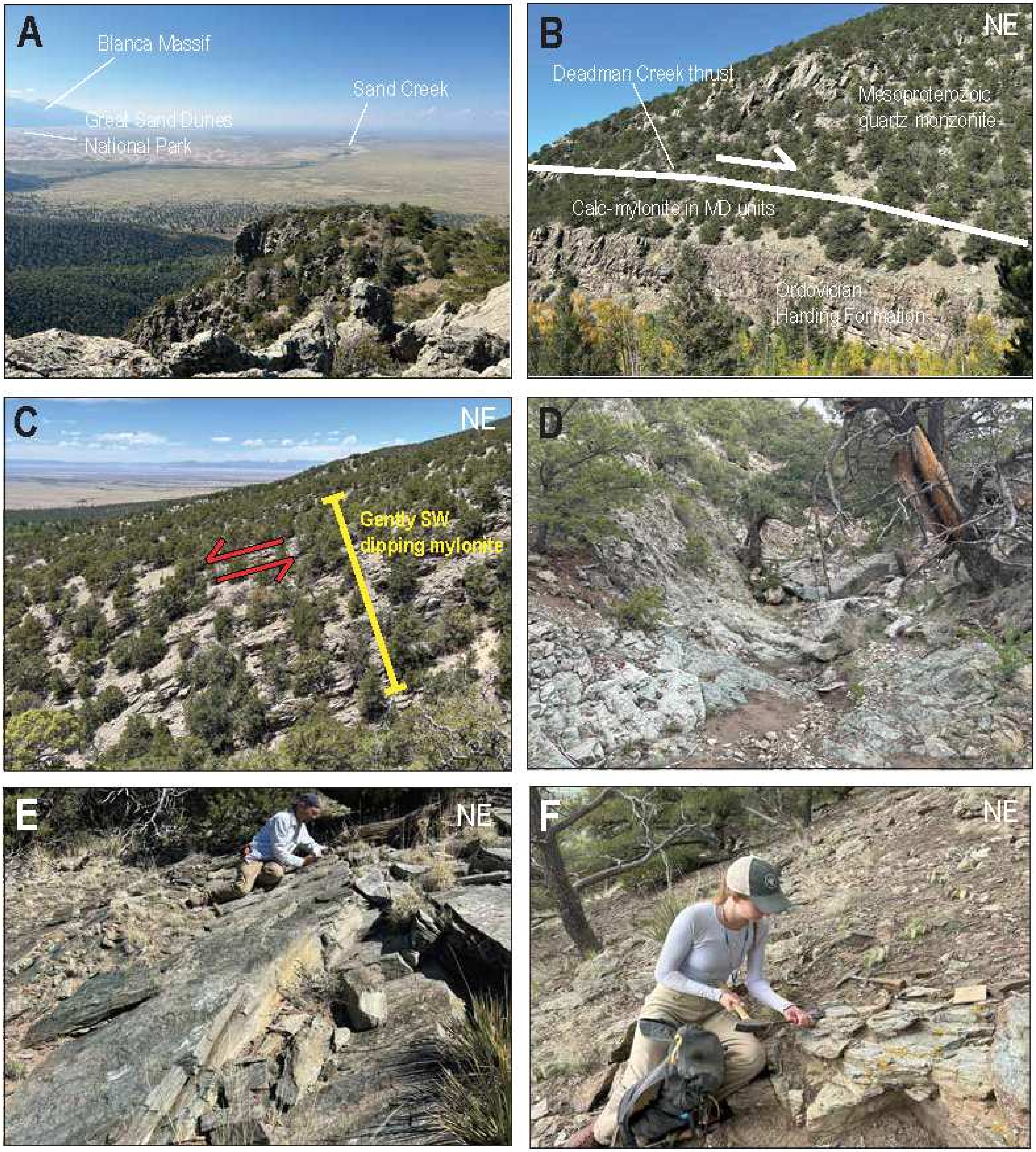

Figure 9: Field photographs showing major structures and features in the study area. (a) Regional overview of the mapping area showing Great Sand Dunes National Park, Sand Creek, the San Luis Valley, and the Blanca Massif in the background. (b) Exposure of the Deadman Creek thrust fault along Deadman Creek, showing the basement rocks over the Paleozoic stratigraphy. (c) Thick, gently SW-dipping mylonite zone exposed north of Alpine Creek, a major zone of ductile shear. (d) Chloritized gneiss exposed along Short Creek, possibly indicating fluid-rock interaction associated with deformation. (e) SW-dipping mylonite zone within the Duncan shear zone. (f) Additional exposure of a gently-dipping mylonite zone in the

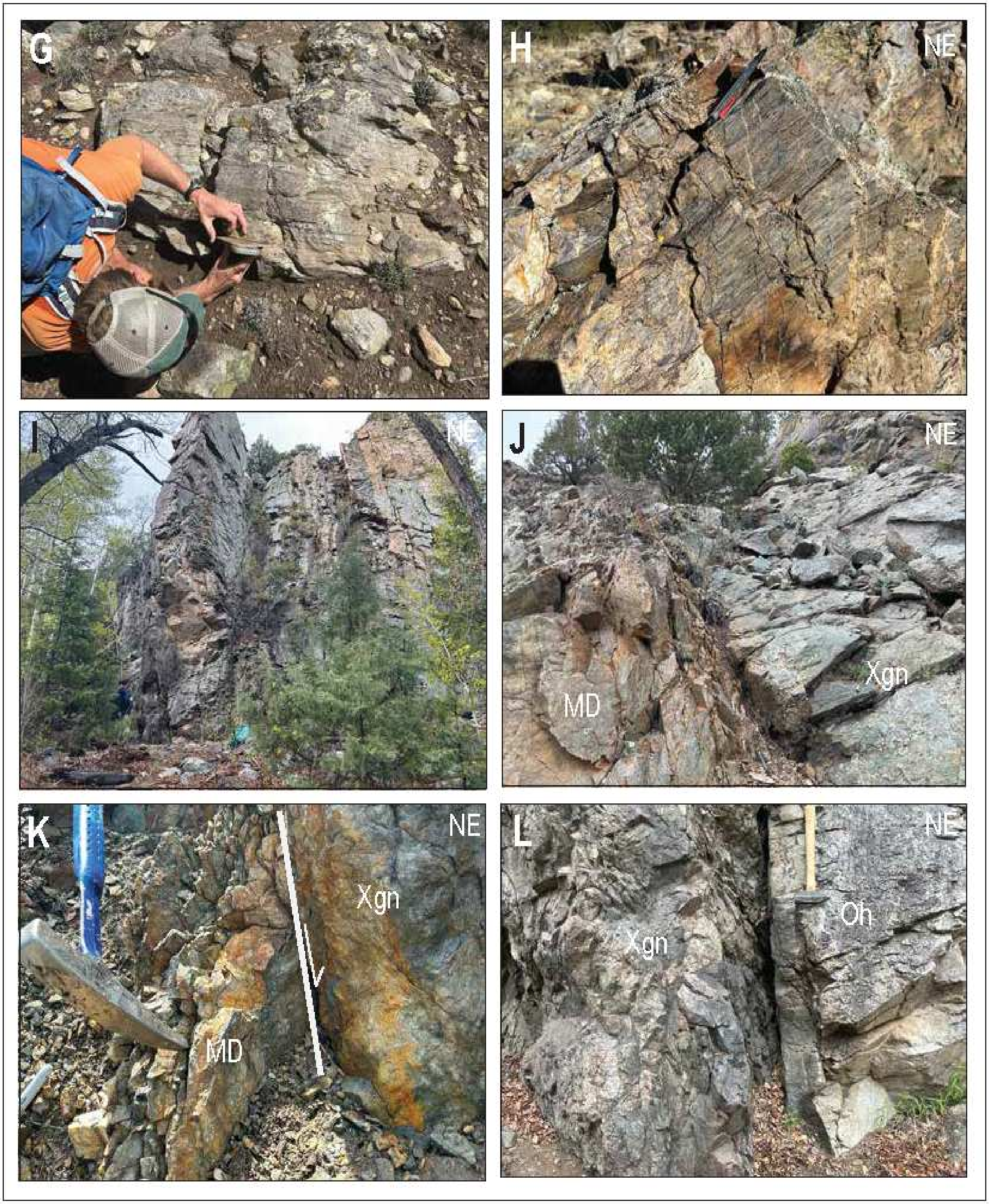

Figure 9 Cont: (g) Mylonite zone developed within gneiss in the Duncan shear zone. (h) Mylonitic fabric preserved in Proterozoic quartzite near the sampling location of sample 24-10-MP1113 on the north side of Deadman Creek. (i) Nearly vertical cliffs of MDO exposed along Sand Creek. (j) Exposure of the Short Creek fault along Short Creek, with mylonitic MD on the left side of the fault and Proterozoic gneiss on the right. (k) An additional exposure of the Short Creek fault, again juxtaposing MD on the left against Proterozoic gneiss on the right. (l) Slightly sheared depositional contact between Xgn and Oh exposed along Sand Creek, indicating localized deformation along the contact.

2.7.2 NE-Vergent Folds

The Deadman Creek thrust has been modified by a phase of NE-vergent folding, likely associated with continued or later-stage Laramide contraction, and best visualized on the cross sections on Plate 1. This folding is expressed in both the geometry of the thrust surface itself and in the orientation of lithologic units in the hanging wall and footwall, especially the Paleozoic strata. The MDO package records the orientation of the footwall directly below the fault trace. Stereonet plots of poles to bedding in the MDO (see section 3.1.3, Figure 8b) display a broad girdle distribution consistent with folding about a northwest-trending, gently-plunging fold axis. This supports the interpretation of a large-scale, NW-trending, NE-vergent fold superimposed on the Deadman Creek thrust. Gneissic foliation in Proterozoic rocks below the MDO is also folded by the NE-vergent folds (Plate 1), and overall patterns of gneissic foliation across the field area define a heterogeneous distribution that suggests a folding about a shallow WNW-plunging axis (Figure 8a). The folds are characterized by a moderately SW-dipping axial surface and a NE-vergent fold geometry, indicating NE-directed shortening superimposed on the original SW-dipping thrust surface. The SW limb of the fold corresponds to the gently SW-dipping segment of the thrust, while the NE limb is steeply NE-dipping to vertical, and locally overturned (steeply SW-dipping).

Geologic mapping in this study demonstrates that the Deadman Creek thrust is not isoclinally folded, contrary to the interpretation of earlier USGS mapping by Johnson et al. (1989), as shown in Figure 10. The apparent isoclinal fold in this earlier map likely resulted from unrecognized stratigraphic repetition and geometry introduced by the Short Creek fault system (discussed in the following section). The intensity and geometry of the NE-vergent folding changes progressively along strike of the Deadman Creek thrust. At Deadman Creek, the northernmost part of the study area (cross section A-A’), the fold is the most open and shallow. In the central part of the study area (cross sections B-B’ and C-C’), the fold tightens slightly to an open to gentle geometry with an interlimb angle of approximately 150°, indicating broad warping of the thrust surface. In the southern part of the map area (cross sections F-F’ and G-G’), the fold becomes tighter with an interlimb angle of ~120°. In this part of the map, two steeply dipping MDO bodies are present. The earlier USGS maps (Johnson et al., 1989; Lindsey et al., 1986) place the Deadman Creek thrust between the MDO and Xgn contact along the southwestern margin of the southwestern MDO body. However, new field evidence instead supports this contact as a locally sheared nonconformity, with Harding Formation quartzite depositionally overlying the crystalline basement. This depositional relationship is well exposed along Sand Creek (Figure 9l). Recognizing this contact as depositional on the southwest side of both MDO bodies indicates that the structural repetition reflects a thrust duplex geometry rather than isoclinal folding, with faults along the northeastern margins of both MDO bodies (Figure 10). Therefore, there are two NE-vergent folds recorded in the MDO package (Plate 1), as well as an interpreted duplex thrust structure (i.e., there are 2 packages of MDO that have been thrusted over the crystalline basement). Mapping along the southeast side of Deadman Creek also suggests the presence of a minor duplex structure (Plate 1). Although the fault trace in this area is inferred and shown as dashed on the map, a sliver of Proterozoic basement rock occurs between MDO units, supporting the interpretation of a small duplex geometry along this segment of the Deadman Creek thrust.

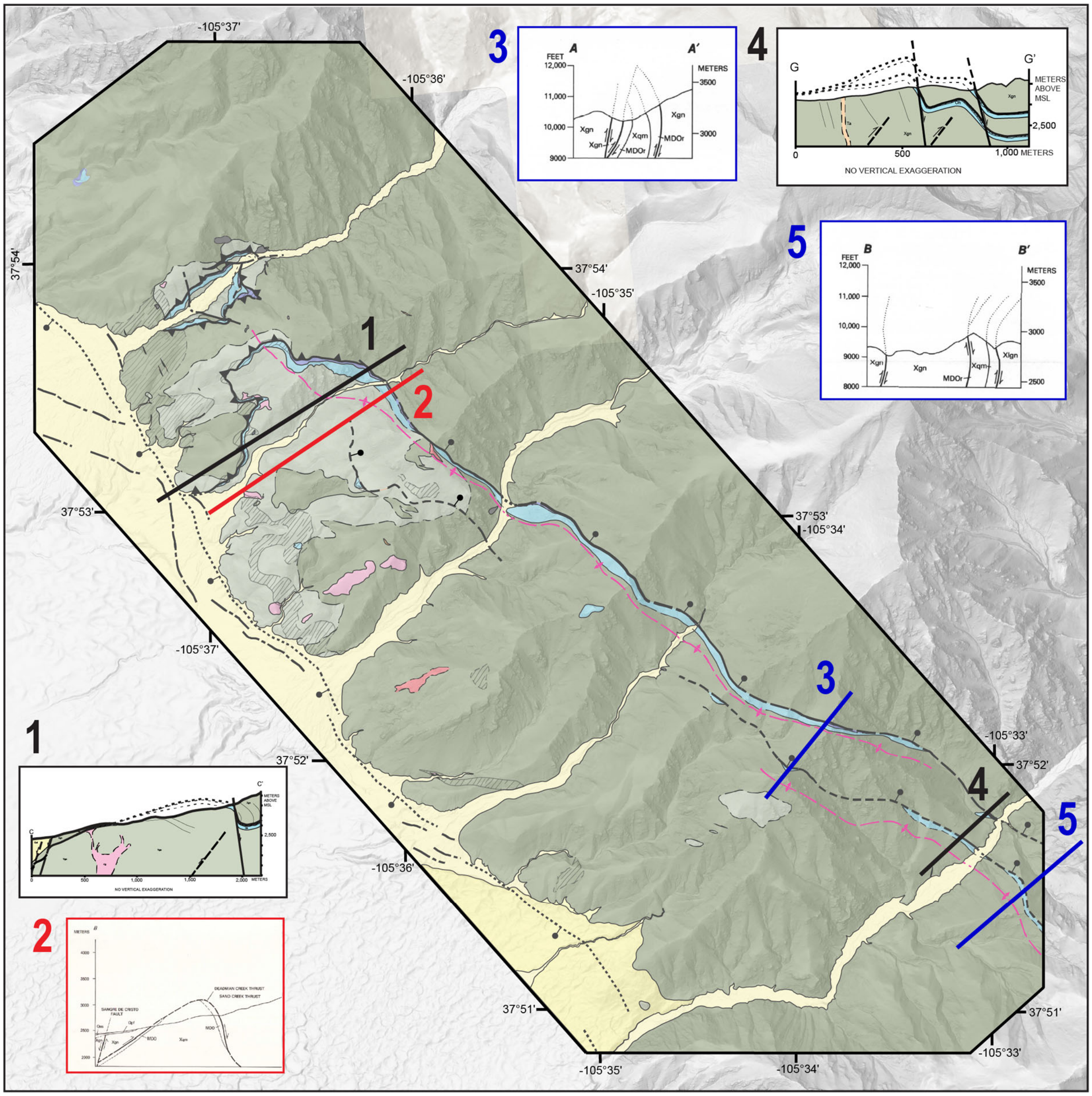

Figure 10: Comparison of cross section interpretations. Comparison of geologic cross sections from previously published USGS mapping (cross sections 2, 3, and 5) and the revised cross sections developed in this study (cross sections 1 and 4). The cross sections illustrate differences in structural interpretation and subsurface geometry resulting from increased mapping resolution and new structural data. Cross sections 3 and 5 are from the Medano Pass Quadrangle (Johnson et al., 1989) and show an isoclinal fold in the Deadman Creek thrust. Cross section 2 is from the Beck Mountain Quadrangle (Lindsey et al., 1986) and shows their interpretation of the folded geometry of the Deadman Creek thrust.

2.7.3 Duncan shear zone

As introduced in section 3.1.5, the Duncan shear zone is a laterally extensive, mylonitic zone located primarily in the northern portion of the study area, on the western range front of the Sangre de Cristo Range (Plate 1). This shear zone is hosted primarily in crystalline basement units (Yqm and Xgn), though near Short Creek it involves an Oligocene granodiorite intrusion, and in some areas includes Harding Formation below the Deadman Creek thrust. Some of the best exposures of this zone are located just NE of the historic mining settlement of Duncan, hence the naming of this zone. The thickness of the mylonite zone is variable, ranging from a few meters to more than 50 meters in some exposures. In several exposures, particularly north of the Pole Creek drainage and in the area between Deadman Creek and Alpine Creek, the mylonites are exceptionally well-exposed in protomylonitic to ultramylonitic quartzofeldspathic gneiss and quartz monzonite along a gently SW-dipping zone with consistent top-SW kinematics.

The Duncan shear zone is especially thick and high strain near Deadman Creek, where it is located in the hanging wall of the Deadman Creek thrust. It is also thick and well-developed between Alpine Creek and Pole Creek, although in this area the shear zone is hosted in the footwall rocks of the Deadman Creek thrust. The Duncan shear zone locally encompasses the Deadman Creek thrust and MDO strata below the thrust, indicating an overprinting relationship. Discontinuous exposures of similar mylonitic fabric, separate from the main Duncan shear zone occur farther south, near Short Creek and Sand Creek, where mylonitic quartzofeldspathic gneiss exhibit the same shallow SW dip and top-SW shear sense (Plate 1).

The mylonitic fabric in this zone is well developed and is defined by a gently dipping to subhorizontal mylonitic foliation and stretching lineations that trend generally NE-SW (Figure

8e) with a mean lineation trend of 246°. The mapped shear zone margins dip shallowly to the SW and locally contour topography, particularly between Pole Creek and Alpine Creeks. At the outcrop scale, as well as in thin section, numerous kinematic indicators confirm a consistent top-SW to top-W shear sense, which is a defining characteristic of the Duncan shear zone and contrasts with mylonitic fabrics associated with the Deadman Creek thrust (Figure 12). Kinematic indicators include S-C fabrics, sigmoidal foliation patterns, asymmetric feldspar and quartz oblique grain shape fabrics, and C' shear bands (section 3.3.2, Figure 12). Locally, the Duncan shear zone also contains symmetric structures, suggesting a coaxial component of deformation in addition to overall top-SW shear.

2.7.4 Short Creek fault system

The moderate- to steeply NE-dipping limb of the folded Deadman Creek thrust is cut by a series of brittle-plastic faults that collectively define the Short Creek fault system. The largest of these faults is best exposed on the north side of Short Creek, hence why we have termed this structural feature the Short Creek fault system. These faults were previously mapped as part of the Deadman Creek thrust by Lindsey et al. (1986) and Johnson et al.(1989), but new field observations and cross-cutting relationships demonstrate that they represent an Oligocene extensional fault system that in many places parallels the moderate to steep NE-dipping limb of the NE-vergent folds (as described in section 3.2.2). These normal faults strike NW-SE and are most continuous from Sand Creek in the south to Alpine Creek in the north (Plate 1). The Short Creek fault system is not exposed in the area around Deadman Creek. The faults are primarily localized parallel to bedding along the mechanically weaker lithologies of the MDO package.

The main strand of the Short Creek fault system is characterized by a zone of foliated Minturn Formation phyllite and MDO carbonate, with pressure-solution fabrics and brittle deformation including fault slickensided surfaces and cataclastic deformation (see section 3.3.3, Figure 13). The fault core is typically narrow (less than 5 m) and is often ochre to orange in color due to sulfide and Fe-oxide alteration (Figure 9j, k, l). The absence of this sulfide and Fe-oxide mineralization along the more gently dipping portions of the Deadman Creek thrust (section 3.2.1) further supports the interpretation that the Short Creek fault is a different structure. The foliation within the phyllite typically parallels the fault plane or dips more shallowly than the fault plane and defines a steep NE-dipping shear fabric, consistent with top-NE, normal-sense displacement. Two locations of NE-dipping phyllite preserve local top-SW reverse-sense shear, which may record flexural shear associated with the development of the NE-vergent folds. A secondary, subparallel strand of the Short Creek fault system occurs to the SW of the main fault strand. This strand is characterized by phyllitic foliation in the MDO adjacent to crystalline basement. At one outcrop along Pole Creek, MDO is absent along the interpreted continuation of the fault, and the fault core is characterized by a secondary, white mica and chlorite shear fabric in the crystalline basement units. This strand of the fault also involves deformation of a late Oligocene aplite dike that parallels the fault in the footwall (24-5-MP233b, see section 3.6.1). Along the principal slip plane of the fault this aplite dike has dynamically recrystallized quartz slickenfibers and a white-mica-defined oblique foliation consistent with NE-down normal shear (Figure 13c), indicating that brittle-ductile extension associated with the Short Creek fault system occurred in the late Oligocene.

Fault plane and slickenline measurements provide quantitative constraints on the geometry and kinematics of the Short Creek fault system. These measurements define a dominant NW strike and steep to moderate NE dip with a mean orientation of 318°/73° NE (Figure 8j). This distribution reflects a steeply NE-dipping fault set that is subparallel to the folded Deadman Creek thrust surface. Of the measured faults associated with the Short Creek fault system, 44 record sense of slip, which were used to evaluate the kinematics of the Short Creek fault system. Most slickenline measurements indicate normal slip/hanging wall-toward the NE, but locally slickenlines record minor oblique or left-lateral strike-slip (Dataset 4). The associated P- and T-axis orientations (Figure 8h & l) define a clear kinematic framework: P-axes (blue) plunge subvertically, whereas T-axes (red) plunge shallowly to the NE and SW, consistent with NE-SW directed extension in a normal fault regime. The linked Bingham axes define a mean extension direction of 35°/16° and a mean shortening direction of 258°/70°.

2.7.5 Sangre de Cristo fault system

The Sangre de Cristo fault system has limited exposures in the western part of the study area. Along the range front, chlorite-altered crystalline rocks and cataclastic deformation zones (Figure 5l) record brittle deformation adjacent to the Sangre de Cristo fault. These cataclastic zones are particularly prominent near Deadman Creek, where they are up to tens of meters wide and may represent exhumed portions of the Sangre de Cristo fault system. The zones occur mainly in the Proterozoic gneiss, though they also involve high strain mylonite from the Duncan shear zone.

Although outcrop-scale fault surfaces associated with the Sangre de Cristo fault system are rare within the mapped area, multiple Quaternary fault scarps are visible on aerial imagery and LiDAR (Plate 1), particularly in unconsolidated late Pleistocene and Holocene sediments west of the exposed bedrock (Ruleman and Machette, 2007). The alignment of these scarps with the regional trace of the Sangre de Cristo fault system confirms its continued activity through Quaternary time.

2.8 Microstructural and Kinematic Analysis

Microstructural and kinematic analyses were jointly applied to characterize the style, intensity, and spatial distribution of deformation across the Deadman Creek mapping area. Microstructural analysis of oriented thin sections reveals a spatially variable record of deformation conditions across the Deadman Creek mapping area. Results are summarized in terms of deformation category (1–3, where 1 is the lowest temperature deformation category and 3 is the highest; see section 2.3) and presented in Figure 14, with full microstructural sample descriptions in Dataset 6. Kinematic analysis focused on determining the sense and direction of deformation in the mapping area using field and petrographic observations of shear-sense indicators. Figure 16 records a spatial summary of kinematics in the mapping area, and a compilation of observed kinematics in the mapping area is available in Dataset 5. Microstructures and kinematics associated with the major structural features in the Deadman Creek thrust area (including the Short Creek fault system, the Duncan shear zone, and the Deadman Creek thrust itself) are described in the sections below.

2.8.1 Deformation fabrics along the Deadman Creek thrust

The Deadman Creek thrust records a zone of mylonitic deformation developed primarily within the MDO section in the footwall of the fault, with minor mylonitic fabric development in Proterozoic crystalline basement directly above the fault in some areas. The photomicrographs shown in Figure 10 are all samples of the MDO sequence associated with the Deadman Creek thrust. These samples show a variety of microstructures, including asymmetric mantled quartz porphyroclasts within a fine-grained calcite matrix (Figure 11a, b, c), oblique grain shape fabrics of dynamically recrystallized calcite (Figure 11d), and S-C fabrics recorded in mylonitic quartzite of the Harding Formation (Figure 11e & f). Some of the recrystallized quartz ribbons in these quartzite samples exhibit evidence of bulging (BLG) and subgrain rotation (SGR) recrystallization, indicating deformation accommodated by dislocation creep.

The microstructures recorded in the rocks along the Deadman Creek thrust, including the extent and mechanisms of quartz and calcite recrystallization, mainly represent deformation temperatures around 300–450°C, indicating lower greenschist-facies conditions, consistent with Category 2 deformation (see section 2.3). Locally, chloritically altered cataclastic rocks (as representative of Category 1) are present along the Deadman Creek thrust, but in many areas the sheared, mylonitic MDO rocks lie directly beneath the thrust surface and completely lack cataclastic deformation. For example, exposures along the north side of east Deadman Creek and Alpine Creek (e.g., quartzite sample 24-8-MP387a) show no evidence of cataclasis.

Most of the samples from the Deadman Creek thrust record top-NE kinematic indicators that are consistent with the NE-directed Laramide thrust direction. Top-NE directed kinematic indicators are most prevalent in calc-mylonites derived from the Leadville Limestone and other Paleozoic carbonates. The oblique grain shape fabrics in dynamically recrystallized polygonal calcite as well as tails on mantled quartz porphyroclasts are the best examples of top-NE kinematics in the Deadman Creek thrust area (Figure 11a, b, c, d). On the other hand, some thin sections of Harding Formation quartzite from the footwall of the thrust show finely foliated recrystallized quartz grains with interstitial white mica that define continuous to semicontinuous mylonitic foliation and S-C fabrics suggesting top-SW shear (Figure 11e, f). These top-SW directed S-C fabrics and asymmetric quartz ribbons within the quartzites along the Deadman Creek thrust may record overprinted strain associated with the Duncan shear zone.

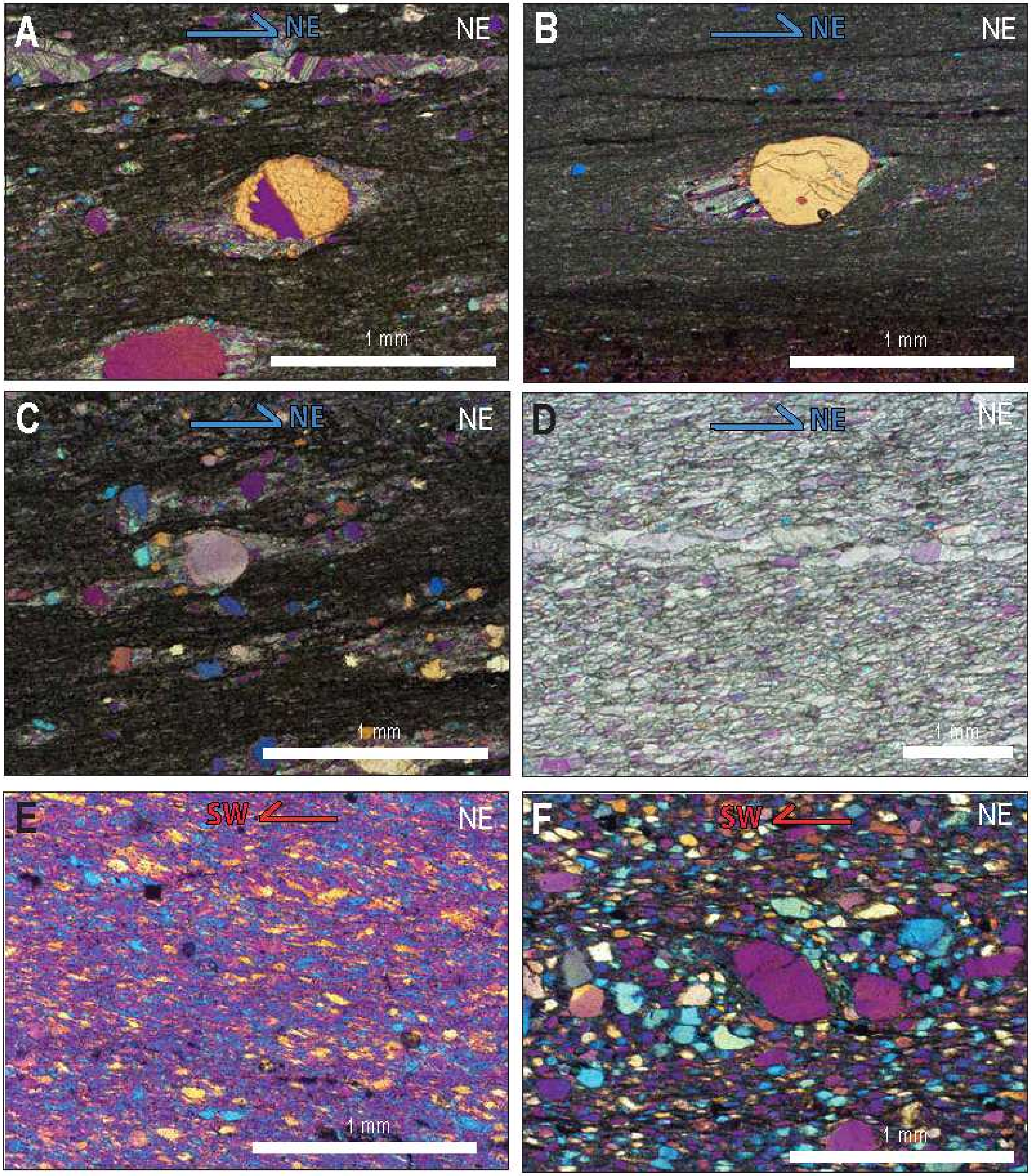

Figure 11: Photomicrographs of microstructures associated with the Deadman Creek thrust. Cross-polarized light (XPL) photomicrographs of deformation microstructures from samples associated with the Deadman Creek thrust, imaged with the accessory plate to enhance contrast and deformation fabrics. (a) Calc-mylonite (sample 24-5-MP470) at 5x magnification. A mantled quartz porphyroclast is surrounded by a fine-grained, dynamically recrystallized matrix and exhibits asymmetric calcite tails consistent with top-NE shear. (b) Calc-mylonite (sample 24-10-DC75) at 5x magnification. Mantled quartz porphyroclast within a foliated calcite-rich matrix showing asymmetric geometry indicative of top-NE shear. (c) Calc-mylonite (sample 24-5-MP470) at 5x magnification. Another example of a mantled quartz porphyroclast within a fine-grained calcite matrix, recording top-NE shear. (d) Calc-mylonite (sample 24-10-JS16) at 10x magnification. Fine-grained, polygonal calcite displays a well-developed oblique grain-shape fabric, consistent with top-NE shear. (e) Harding Formation quartzite (sample 24-5-MP240b) at 5x magnification. Quartz-rich fabric with asymmetric strain indicators and a weak foliation defined by recrystallized quartz, recording top-SW-shear. (f) Harding Formation quartzite (sample 24-8-MP333) at 5x magnification. Dynamically recrystallized quartz grains define a penetrative foliation and asymmetric fabric consistent with top-SW shear.

2.8.2 Mylonitic deformation in the Duncan shear zone

The Duncan shear zone records predominantly mylonitic deformation within Proterozoic basement rocks, but it locally encompasses the MDO sequence. Examples of mylonite samples from the Duncan shear zone are shown in Figure 12 and commonly contain strong S-C fabrics defined by white mica and recrystallized quartz, fractured and rotated feldspar porphyroclasts, and grain size reduction associated with mylonitization. Some thin sections, especially MDO quartzites, have ribbons of plastically deformed quartz that have undergone both bulging (BLG) and subgrain rotation (SGR) recrystallization (Figure 12e). In other samples, the quartz recrystallization is limited and feldspar porphyroclasts display pervasive brittle fracturing and evidence of chemical alteration and breakdown to white mica (Figure 12c, d, & f).

The majority of mylonite samples associated with the Duncan shear zone fall into deformation Category 2, which represents lower-greenschist facies conditions (~300–450°C). These samples are characterized by the development of quartz ribbons with moderate bulging (BLG) and subgrain rotation (SGR) recrystallization, as well as pervasively fractured feldspar grains. Many samples contain synkinematic chlorite and epidote, consistent with deformation at moderate temperatures and elevated fluid activity. These features are especially prevalent in samples of the Mesoproterozoic quartz monzonite (Figure 12c, d, & f). Several samples associated with the Duncan shear zone fall into Category 3, which represents the most highly deformed samples in the mapping area, reflecting temperatures of approximately 400–500 °C that are indicative of deformation under mid- to upper-greenschist facies conditions. These samples display pervasive quartz recrystallization by subgrain rotation (SGR) and bulging (BLG) mechanisms, forming well-developed S-C fabrics. Synkinematic chlorite, epidote, and locally biotite are present. These mylonitic fabrics represent the most plastic style of deformation preserved in the study area.

In samples of mylonites from the Duncan shear zone, the asymmetry of porphyroclasts and oblique alignment of S and C planes commonly indicate top-SW shear, consistent with the majority of kinematic indicators observed in the field in outcrops from the Duncan shear zone (Figure 16). Some samples in the Duncan shear zone also record symmetric structures such as Φ-type porphyroclasts and uniformly-orientated foliae indicative of coaxial strain.

Compared to the more brittle-plastic deformation in the Short Creek fault system (described in the next section), rocks within the Duncan shear zone exhibit more pervasive and higher-temperature ductile deformation and microstructures, resulting in more continuous and well-developed mylonitic fabrics developed under apparent mid- to upper-greenschist facies conditions. The microstructures recorded in these rocks indicate that the Duncan shear zone represents a hotter phase of deformation, accommodating significant shear before later brittle-plastic deformation associated with the Short Creek fault system.

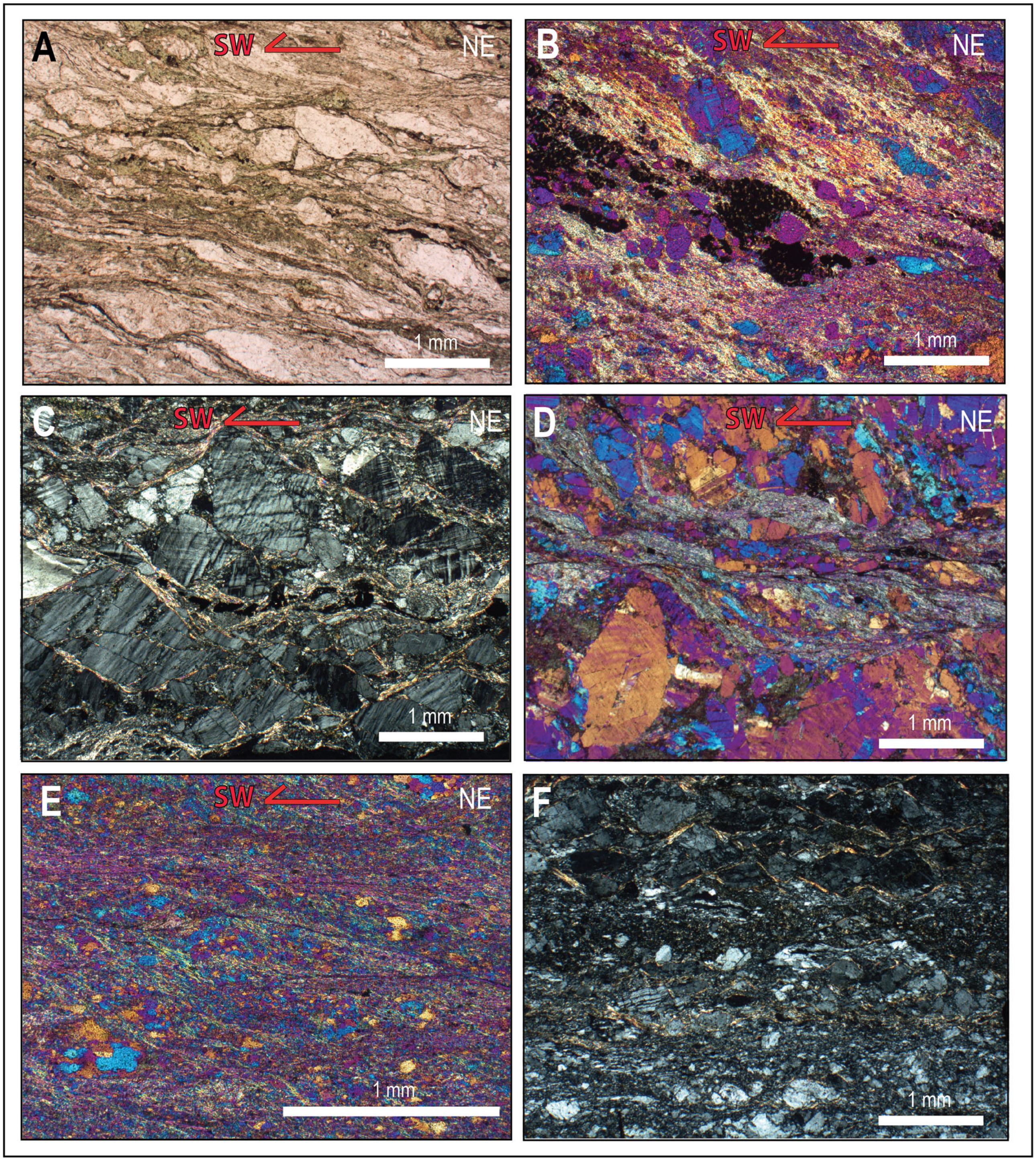

Figure 12: Photomicrographs of microstructures associated with the Duncan shear zone. Photomicrographs of deformation microstructures from samples collected within the Duncan shear zone, illustrating ductile fabrics developed in granodiorite and quartz monzonite protoliths. (a) Mylonitic granodiorite (sample 23-6-ShC1b) at 2.5x magnification, shown in PPL. The sample contains abundant secondary chlorite and white mica, feldspar breakdown to a fine-grained polyphase mixture, discontinuous recrystallized quartz ribbons, and brittlely deformed feldspar. An S-C fabric indicates top-SW shear. (b) Mylonitic quartz monzonite (sample 24-5-MP43b) at 2.5x magnification, shown in XPL with accessory plate. An S-C fabric defined by aligned and recrystallized mica grains indicates top-SW shear. (c) Protomylonitic quartz monzonite (sample 24-10-MP1231) at 2.5x magnification, shown in XPL. Pervasive feldspar fracturing, secondary white mica, and minor recrystallized quartz ribbons. Domino-style fractures in feldspar and an S-C fabric recorded dominantly in white mica indicate top-SW shear. (d) Quartz monzonite (sample 24-5-MP43b) at 2.5x magnification, shown in XPL with accessory plate. Brittlely fractured feldspar, minor quartz recrystallization, and abundant secondary white mica define an S-C fabric consistent with top-SW shear. (e) Fine-grained mylonite (sample 24-10-MP886) at 5x magnification, shown in XPL with accessory plate. The rock contains abundant secondary white mica, quartz ribbons, and minor twinned calcite. An S-C fabric indicates top-SW shear. (f) Proterozoic gneiss (sample 23-6-ShC6) at 2.5x magnification, shown in XPL without accessory plate. This sample shows coaxial kinematic indicators.

2.8.3 Brittle-plastic deformation in the Short Creek fault system

The Short Creek fault system exposes a range of fault rocks that record a predominantly brittle-plastic deformation within the Paleozoic sedimentary units in the footwall of the Deadman Creek thrust and brittle deformation of crystalline basement rocks in the hanging wall. Fault-related lithologies include cataclasites derived from quartzite and gneiss, sheared phyllite derived from the Minturn Formation, and carbonate mylonites derived from the MDO sequence. Photomicrographs of samples from the Short Creek fault are shown in Figure 13. Several photomicrographs of slickenlined surfaces with dynamic quartz recrystallization are pictured in Figure 13c, d, & e. Collectively, the fault system is characterized by a combination of phyllitic shear fabrics, localized zones of quartz plasticity, pressure solution in metasedimentary rocks, and cataclasite textures, consistent with deformation near the brittle-plastic transition. The dominant microstructural characteristics of each fault rock type are described in the following paragraphs.

Cataclasites derived from quartzite and gneiss exhibit pervasive grain-size reduction and angular clast fragmentation set within a fine-grained matrix (Figure 13a, e, h, i, j, k, & l.) Alteration minerals including chlorite and fine white mica are common and locally define a weak foliation wrapping rigid quartz and feldspar clasts as well as moderately defined S-C fabrics. Quartz preserves minor indicators of crystal-plastic accommodation, including sweeping extinction, deformation bands, and some subgrain development, suggesting minor ductile deformation during cataclasis. These features collectively suggest shear under conditions approaching the brittle-plastic transition.

Phyllitic fault rocks, mostly derived from the Minturn Formation, display a well-developed foliation defined by aligned white mica and other phyllosilicates, reflecting shear overprinted onto pre-existing sedimentary fabrics (Figure 13b, d, f, & g). In some quartzites along the fault, localized pressure-solution processes are indicated by dark seams concentrated along foliation surfaces around eye-shaped quartz grains. Minor crenulation, asymmetric mantled porphyroclasts, and sheared quartz grains provide evidence for shearing and brittle-ductile deformation in these clastic sedimentary protoliths. Additionally, several samples of carbonate mylonites from along the Short Creek fault display dynamically recrystallized polygonal calcite grains that form a distinct oblique grain-shape fabric.

Unlike the more ductile mylonitic fabrics associated with the Duncan shear zone and parts of the Deadman Creek thrust, deformation along the Short Creek fault system is marked by steep, discrete, brittle slickensided fault surfaces in addition to the brittle-plastic and cataclastic deformation described above. The deformation temperature for the Short Creek fault system is likely around 250–350°C (Category 1), near the quartz brittle-plastic transition (BPT).

Within the Short Creek fault system, the cataclastic S-C fabrics, recrystallized quartz slickenfibers, and asymmetric grain-shape fabrics typically record a top-NE slip sense, consistent with normal slip along NE-dipping faults planes associated with the Short Creek fault. Some samples record a top-SW slip sense (Figure 13b & f), perhaps associated with flexural slip on the NE-vergent folding of the Deadman Creek thrust. A clear top-NE shear sense fabric is particularly evident in recrystallized quartz slickenfibers and white mica shear fabrics in a sample taken from a synkinematic Oligocene aplite dike along the Short Creek fault (Figure 13c).

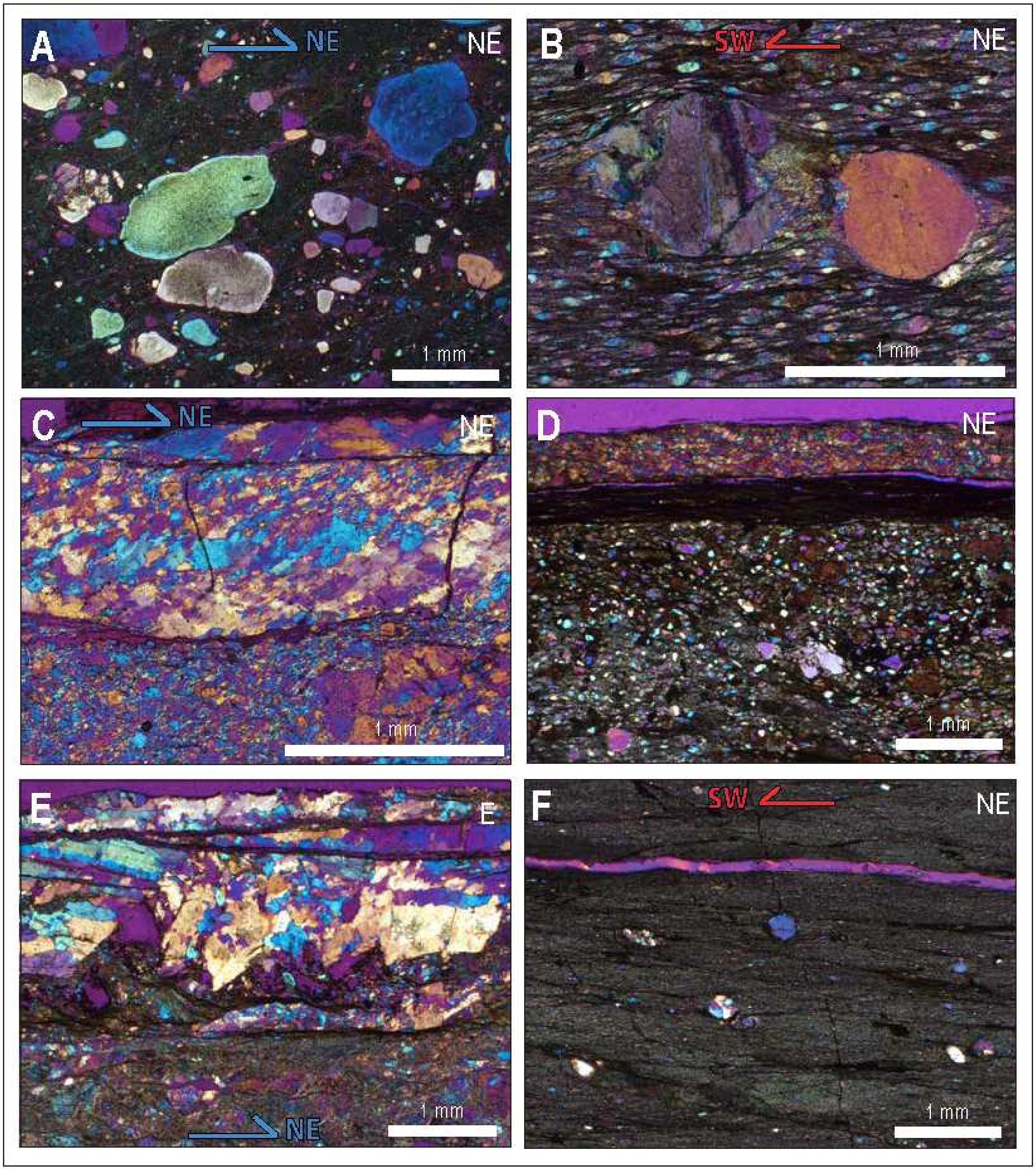

Figure 13: Photomicrographs of microstructures associated with the Short Creek fault system. Cross-polarized light (XPL) photomicrographs of deformation microstructures from samples collected within the Short Creek fault system, illustrating primarily brittle-plastic fabrics. All images are shown in XPL with the accessory plate except panels I, J, and L, which are shown in XPL only. (a) Quartz-rich protomylonite from a faut surface in the Harding Formation (sample 24-10-MP949) at 2.5x magnification. Rounded quartz grains with sweeping extinction are supported by a fine-grained, mica-rich matrix. The matrix appears strained with a subtle foliation, and an oblique fabric indicates top-SE shear. (b) Fine-grained, eye-shaped quartz grains in the Harding Formation (sample 24-5-MP114a) at 5x magnification. The sample contains pressure solution strain, some sigma-type asymmetry of quartz, and shear bands that indicate top-SW shear. (c) Aplite dike (sample 24-5-MP233a) at 5x magnification. Quartz slickenfibers along the top of the sample record top-NE shear. (d) Quartz-rich mylonite (sample 24-5-MP58b) at 2.5x magnification. Eye-shaped quartz grains and retrogressed porphyroclasts show heterogeneous shear sense: some domains indicate top-left (top-SW) shear, others top-right (top NE) shear. Unstrained quartz cores are bordered by dark seams interpreted as pressure solution. (e) Fault surface and fine-grained mylonite (sample 24-5-MP104) at 2.5x magnification. Recrystallized quartz, secondary white mica, and chlorite define an S–C fabric, with quartz slickenfibers and sheared mica/chlorite indicating top-left (top-SW) slip. Slickenfibers show SGR and BLG recrystallization. (f) Finely foliated protomylonite (sample 24-5-MP58a) at 2.5x magnification. White mica and clay-rich matrix with quartz (or possible cordierite) porphyroclasts display faint tails around porphyroclasts and a subtle S–C fabric indicating top-right (top-SW) shear.

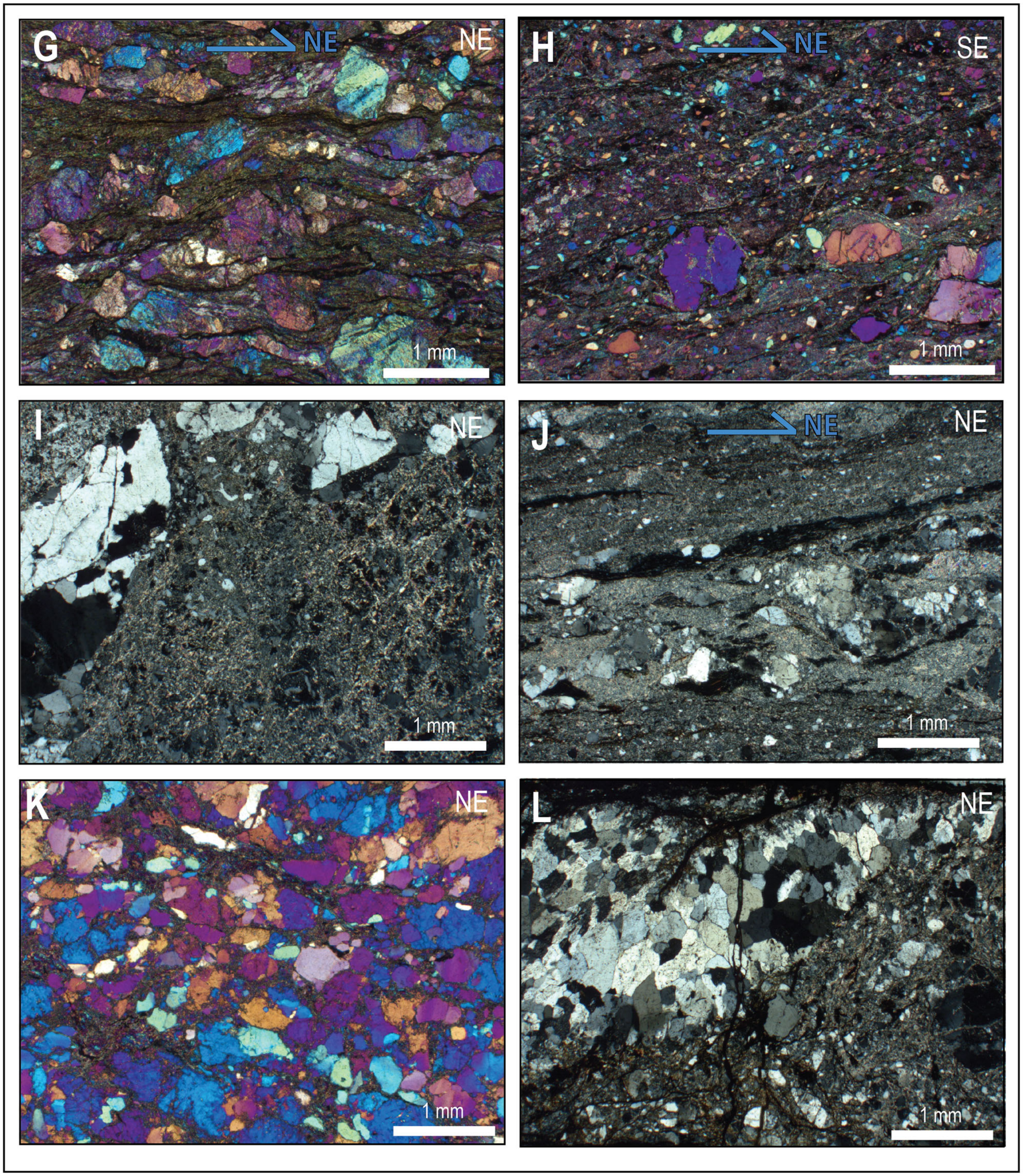

Figure 13 Cont: (g) Brittle-plastic mylonite/protomylonite (sample 24-5-MP158) at 2.5x magnification. Foliation is defined by chlorite; feldspar is brittlely deformed and altered to sericite. An S–C–C' fabric indicates top-right (top-NE) normal-sense shear, with abundant secondary epidote and minor dynamically recrystallized calcite and titanite. (h) Quartz-rich protomylonite (sample 24-10-MP827) at 2.5x magnification. Sub-rounded quartz grains in a fine-grained matrix and white mica define a S-C fabric that indicates top-NE shear. Field observations indicate a sinistral strike-slip sense, with chlorite fabric recording an oblique top-NE component. (i) Cataclasite (sample 23-6-ShC11) at 2.5x magnification, shown in XPL. Quartz, feldspar, secondary white mica, and chlorite exhibit patchy to sweeping extinction, but no recrystallization is observed. (j) Foliated cataclasitemylonite (sample 23-6-ShC13) at 2.5x magnification, shown in XPL. Brittlely fractured quartz clasts show minor plasticity while white mica and chlorite in the matrix define foliation. Foliation patterns and micro-offsets indicate top-right (top-NE) shear. (k) Sheared Harding Formation quartzite along a fault (sample 24-5-MP111b) at 2.5x magnification. Irregularly shaped quartz grains and interstitial white mica with sericitized plagioclase define a protomylonitic to cataclastic texture. Sense of shear is unclear. (l) Cataclastic quartz vein (sample 23-6-ShC12b) at 2.5x magnification, shown in XPL. Large, fractured quartz grains along with secondary white-mica alteration record localized brittle deformation along the vein.

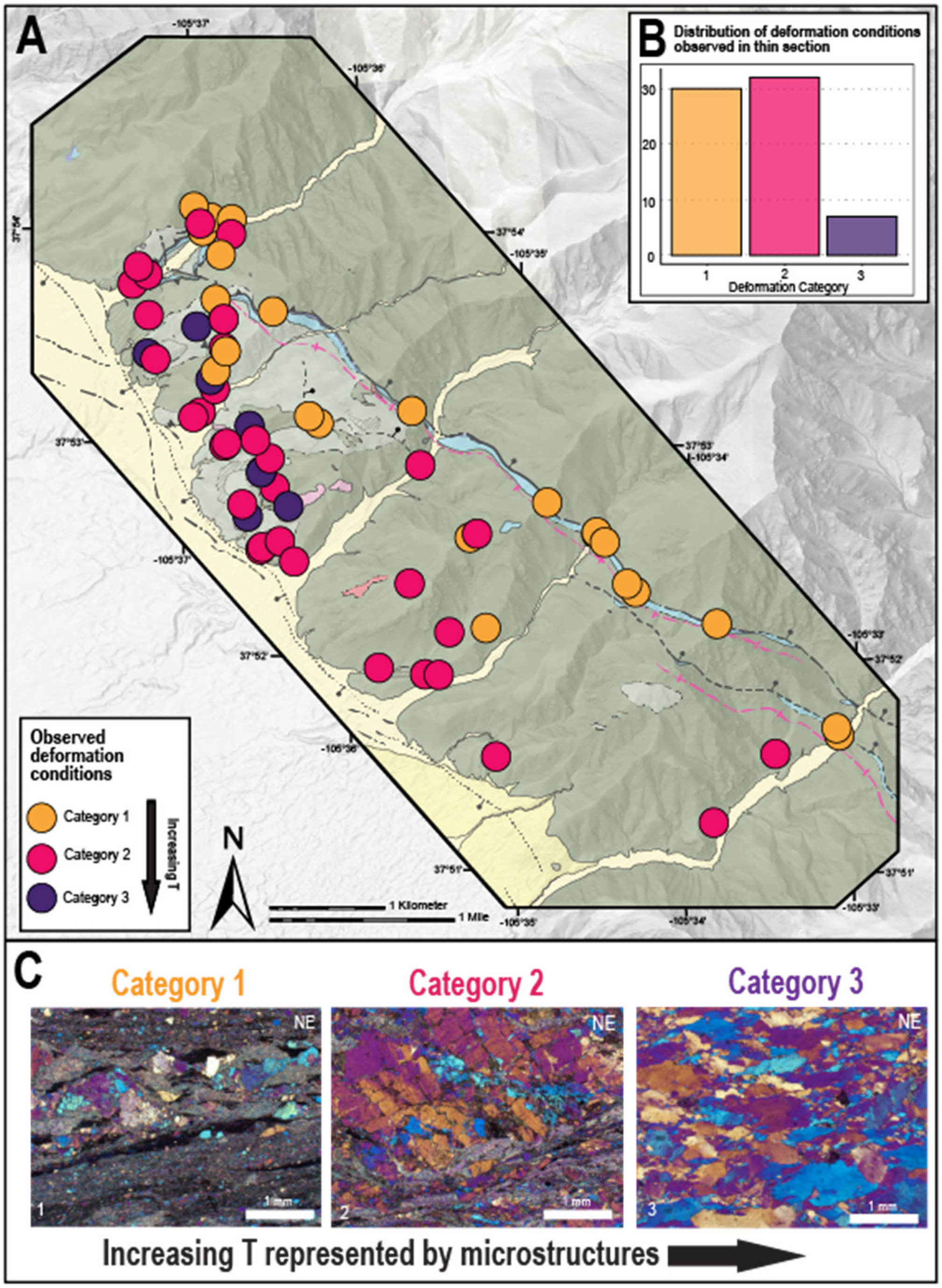

Figure 14: Simplified map of the study area with distribution of deformation conditions. (a) Simplified geologic map of the study area with circles showing the distribution of observed deformation conditions in thin sections of samples taken in the mapping area (see section 2.3 for description of categories). Category 1 (orange) samples display lower temperature deformation conditions and appear to be more prevalent in the eastern part of the mapping area and especially along faults within the Short Creek fault system. Category 2 (pink) samples record lower greenschist deformation conditions and are found throughout the map area. Category 3 (purple) samples represent higher temperature (mid- to upper- greenschist facies) deformation conditions and appear to be concentrated in the NW part of the mapping area. (b) Bar chart showing the amount of each deformation category recorded in thin section samples from the Deadman Creek thrust mapping area. (c) Photomicrographs showing key indicators of deformation categories 1-3. Approximate deformation temperature represented by microstructures increases to the right. Category 1 is dominated by brittle fracturing with pressure solution strain and/or minor quartz dislocation creep. Category 2 represents mid greenschist facies deformation conditions. Category 3 represents samples that formed under upper greenschist facies conditions.

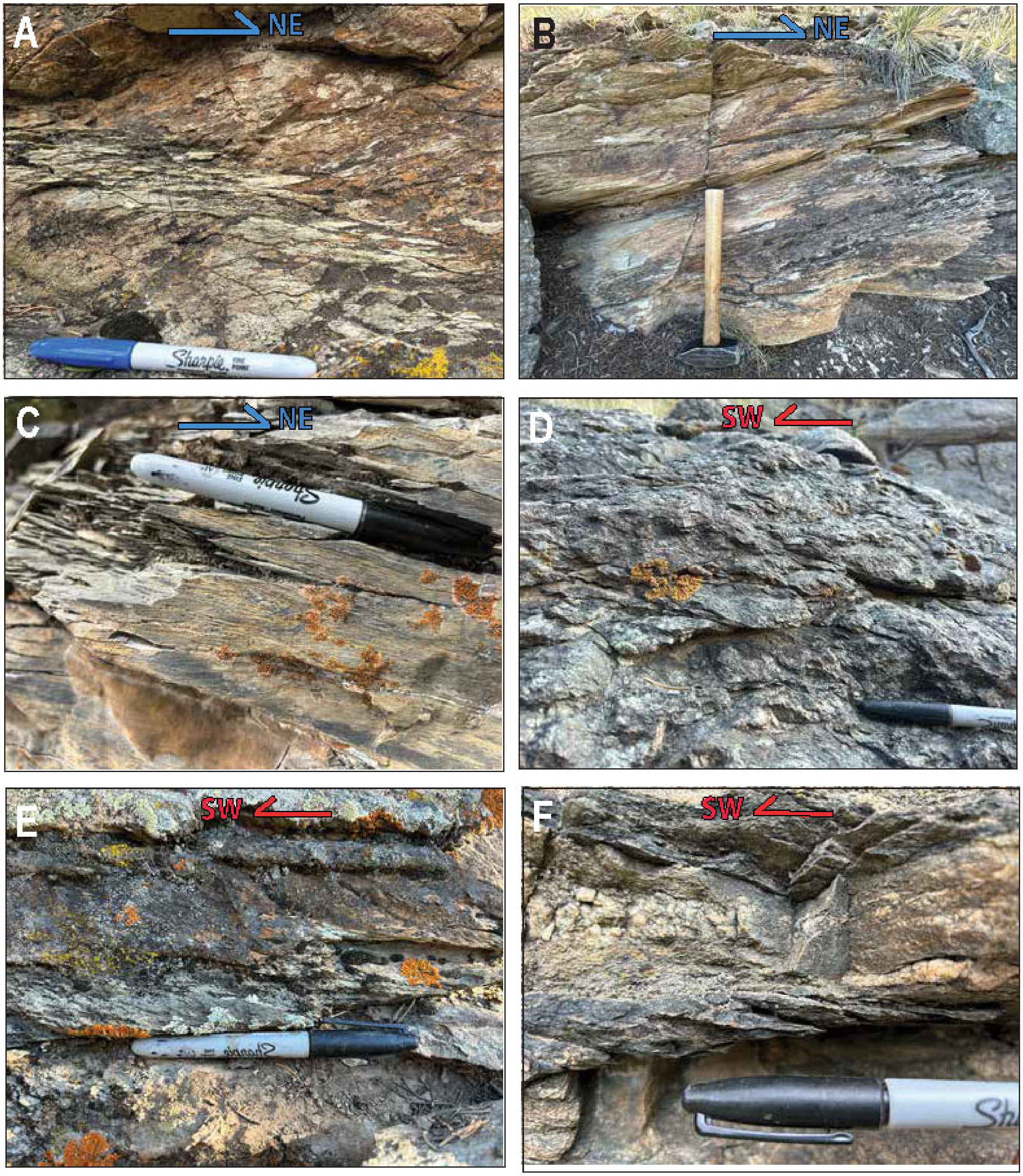

Figure 15: Field photographs of outcrop-scale kinematics in the study area. (a) Top-NE S–C fabric developed in MD carbonate. (b) Top-NE mylonitic fabric in marble mylonite, defined by a penetrative foliation. (c) Additional example of a top-NE shear fabric in marble mylonite. (d) Top-SW S-C fabric developed in Mesoproterozoic quartz monzonite. (e) Top-SW shear fabric observed at the outcrop scale. (f) Another example of a top-SW shear fabric in Proterozoic gneiss.

Figure 15 Cont: (g) Top-SW shear fabric developed in a granodiorite dike exposed along Short Creek, near the sampling locations of samples 23-6-ShC1a and 23-6-ShC1b. (h) Top-SW shear fabric in quartzo-feldspathic gneiss. (i) Top-NE shear fabric in deformed Paleozoic strata. (j) Top-SW shear fabric observed at the outcrop scale, illustrating asymmetric structures consistent with southwest-directed shear. (k) Top-SW shear fabric in Mesoproterozoic quartz monzonite. (l) Top-SW shear fabric in Proterozoic gneiss.

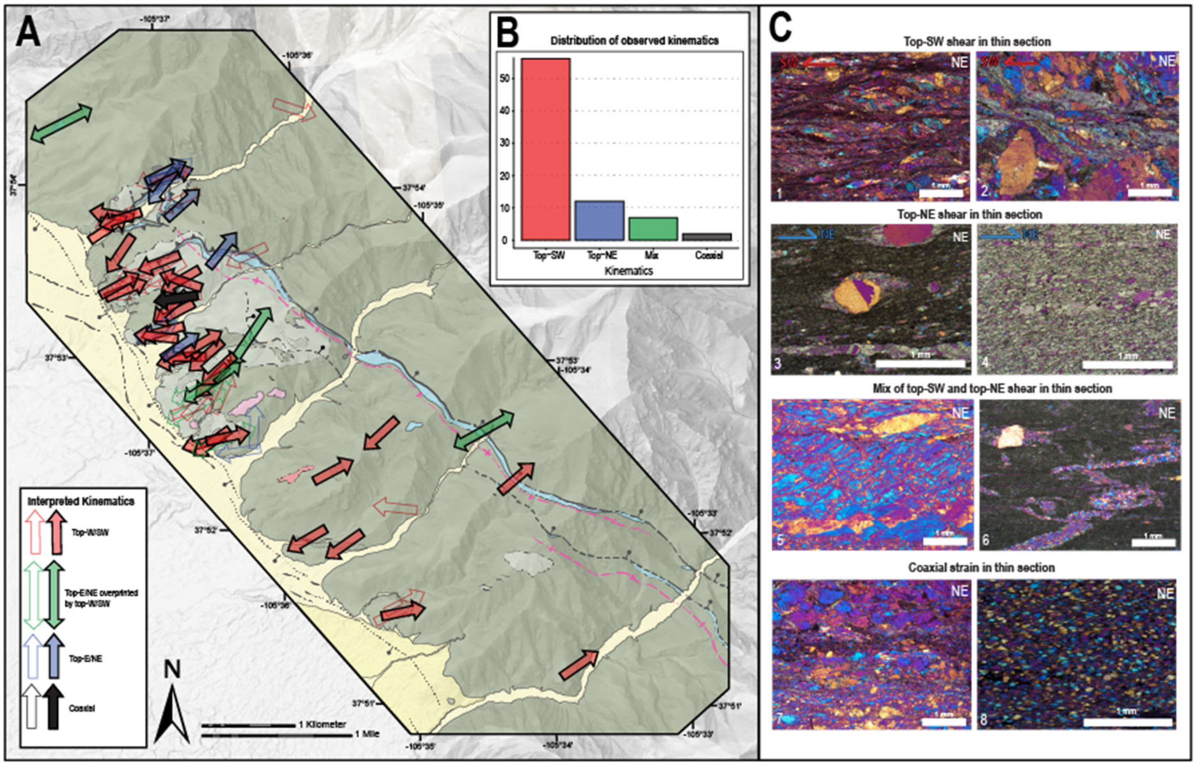

Figure 16: Simplified map of the study area with distribution of kinematics. (a) Simplified geologic map of the Deadman Creek thrust with arrows showing the distribution of observed kinematics in thin section and outcrop. Arrows are parallel to the lineation direction. Solid arrows represent measured lineations, hollow arrows represent outcrops where sense of shear was documented, but no lineation was measured. An average lineation trend of 246° (SW) was plotted for the outcrops where no lineation was measured. (b) Bar chart showing the amount of each kinematic regime observed in thin section and outcrops from the Deadman Creek thrust mapping area. Top-SW kinematics dominate throughout the study area. (c) Photomicrographs showing key example kinematic indicators for top-SW, top-NE, mixed top-NE and top-SW, and coaxial strain. 1: S-C fabric defining top-SW kinematics; 2: S-C fabric in recrystallized mica showing top-SW shear; 3: mantled quartz porphyroclast in calc-mylonite indicating top-NE kinematics; 4: oblique grain shape fabric in polygonal calcite in calc-mylonite indicating top-NE kinematics; 5: recrystallized quartz indicating top-NE shear, cut by fractures that indicate top-SW shearing; 6: top-NE oriented calcite veinlets, deformed and deflected by top-SW shearing; 7: mylonite displaying pure shear (no strong sense of shear indicators); 8: eye-shaped quartz grains in a quartzite, showing pure shear in pressure solution seams between the quartz grains.

2.9 EBSD Results

Thirteen oriented thin sections were analyzed by EBSD to characterize quartz crystallographic preferred orientations (CPOs), determine quartz slip systems, evaluate kinematics, and estimate deformation temperatures across the Deadman Creek thrust and Duncan shear zone using the quartz c-axis opening angle thermometer (e.g., Kruhl, 1998; Morgan and Law, 2004; Law, 2014; Faleiros et al., 2016; Figure 17). Analyses targeted dynamically recrystallized quartz domains from both mylonitic zones (Duncan shear zone, Deadman Creek thrust) and one sample of plastically deformed quartz slickenfibers from the Short Creek fault system. Each sample and associated EBSD results are shown in Figure 18-20, Table 1, and described in detail in Appendix A.

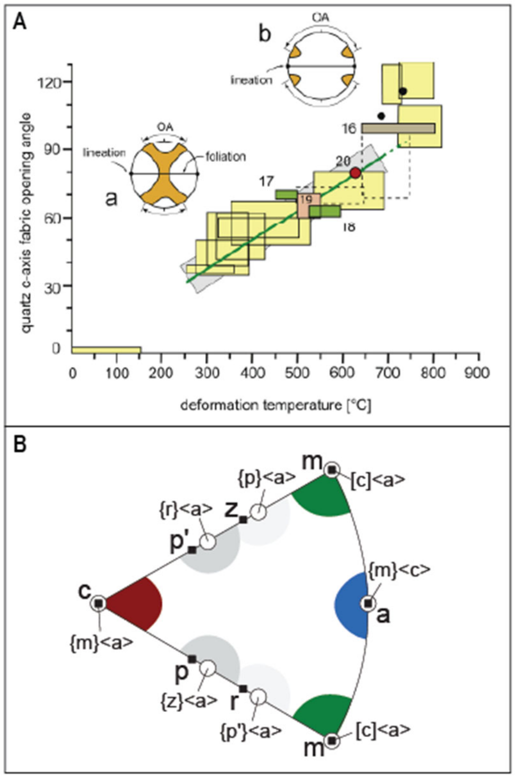

Figure 17: EBSD Reference Figures. (a) Quartz c-axis opening angle vs. deformation temperature plot used to calibrate the c-axis opening angle thermometer (from Faleiros et al., 2016). (b) Inverse pole figure showing quartz crystal directions (c, a, m, r, z, p, and p') and the slip systems of quartz (green = basal <a> slip, blue = prism <c> slip, gray = rhomb <a> slip, red = prism <a> slip). Modified from Zuo et al. (2021) and Neumann (2000).

2.9.1 CPOs and c-axis opening angle temperatures

Deadman Creek thrust

Eight samples of recrystallized quartz were collected from outcrops proximal to the Deadman Creek thrust (<10 m above or below the thrust) and analyzed with EBSD. Sample locations for the EBSD analyses are shown on Figure 20. Most samples were collected from the footwall of the Deadman Creek thrust and capture strain localized withing the Harding Formation beneath the thrusted contact (e.g. 24-8-MP288, 24-8-MP298, 24-8-MP326, 24-8-MP333, 24-8-MP394, and 24-10-MP1038). Many of these samples also overlap with the mapped area of the Duncan shear zone. Additionally, most of these samples were collected during mapping in Alpine Creek, apart from 24-10-1038 which was collected in Deadman Creek. The EBSD data from these samples (Figure 18a-f), complemented by thin section observations, reveal a range of shear senses and kinematic indicators. The CPOs show dominantly coaxial strain with minor components of top-SW and top-NE shear (e.g. 24-8-MP288, 24-8-MP298, 24-8-MP326) and some samples with mostly top-SW shear (e.g. 24-8-MP333). Overall, the recorded CPOs match the shear sense observed in thin section of these samples, though top-SW shear sense indicators were recorded in several thin sections that do not record top-SW oriented CPOs (e.g., 24-8-MP288, 24-8-MP326, and 24-10-MP1038).

Similarly, one sample, 24-10-MP1113 (Figure 18g), was taken from the hanging wall of the Deadman Creek thrust within a pod of Proterozoic quartzite in Deadman Creek. This sample exhibits conflicting shear indicators: thin section observations suggest top-W/SW shear, whereas EBSD measured CPO data indicate coaxial strain with a minor top-E/NE shear component. These discrepancies may reflect the overprinting of multiple shear regimes, with younger top-SW shear having a limited effect on the CPO. Another sample, 24-8-MP387a (Figure 18h), was collected directly from the thrusted contact of the Deadman Creek thrust in the Harding Formation. Thin section observations of this sample show subtle top-NE shear in recrystallized quartz, whereas EBSD measured quartz CPO data record top-SW shear. This sample likely records the overprinting of multiple tectonic regimes at the thrust contact.

C-axis opening angle thermometry of these samples indicate a range of quartz dislocation creep temperatures along the Deadman Creek thrust. Opening angles range from 35 to 74° (Figure 19a-g) and correlate to temperatures of 290 to 559°C ± 50°C according to the Faleiros (2016) opening angle thermometer (Table 1). These temperatures broadly corroborate microstructural deformation condition data (described in section 3.3.1). Several samples were determined to have unreliable temperature estimates (e.g. 24-8-MP394, 24-10-MP1038; Figure 19e & f) based on the quality of the CPO data and are not included in the range of opening angles and temperatures described above.

Duncan shear zone

Four samples (e.g. 24-10-MP1244, 24-9-MP662, 23-6-ShC1, and 23-6-ShC6) were collected from mylonites associated with the Duncan shear zone, located within the range of either 10 m below or above the Deadman Creek thrust (Figure 18i-l). Sample 23-6-ShC1 is a mylonite sample from the Oligocene granodiorite collected near Short Creek, and sample 23-6-ShC6 is mylonitized Proterozoic gneiss near Short Creek. Samples 24-9-MP662 and 24-10-MP1244 are mylonites derived from the Mesoproterozoic quartz monzonite near Deadman Creek and Pole Creek, respectively. The CPO data from recrystallized quartz in these samples show consistent top-SW shear, with the exception of sample 23-6-ShC6, which has dominantly symmetric CPOs indicative of coaxial strain (Figure 18). The kinematic indicators observed in thin section for these samples are consistent with the shear sense recorded in CPOs. Additionally, misorientation axes in inverse pole figures suggest that these samples record exclusively the prism <a> slip system (Figure 18i-l). C-axis opening angle measurements of these samples indicate opening angles of 45° to 57° (Figure 19i-l) which correlate to deformation temperatures of 359 to 441°C ± 50°C according to the Faleiros (2016) opening angle thermometer (Table 1). This temperature range agrees with microstructures observed in thin sections from mylonites in the Duncan shear zone (described in section 3.3.2).

Short Creek fault system

One sample of aplite with recrystallized quartz slickenfibers from Short Creek fault system (24-5-MP233a; Figure 18m) was analyzed with EBSD. This sample was collected from a NE-dipping normal fault surface north of Pole Creek and exhibits clear top-NE shear in oblique recrystallized quartz grains in slickenfibers along the fault, consistent with normal fault motion. The quartz c-axes in this sample are asymmetric and oriented at a relatively low angle with respect to foliation, potentially suggesting prism <c> slip and top-SW shear (Figure 18m). However, misorientation axes in the inverse pole figure suggest basal <a> and prism <a> slip systems in quartz rather than prism <c> slip, which typically only occurs at high temperatures (>600°C; e.g., Passchier and Trouw, 2005), and the microstructures clearly record top-NE shear with respect to the slickenfiber boundary. It is probable that minor recrystallization and dislocation creep was not sufficient to reset the CPO inherited from the original slickenfiber orientation.

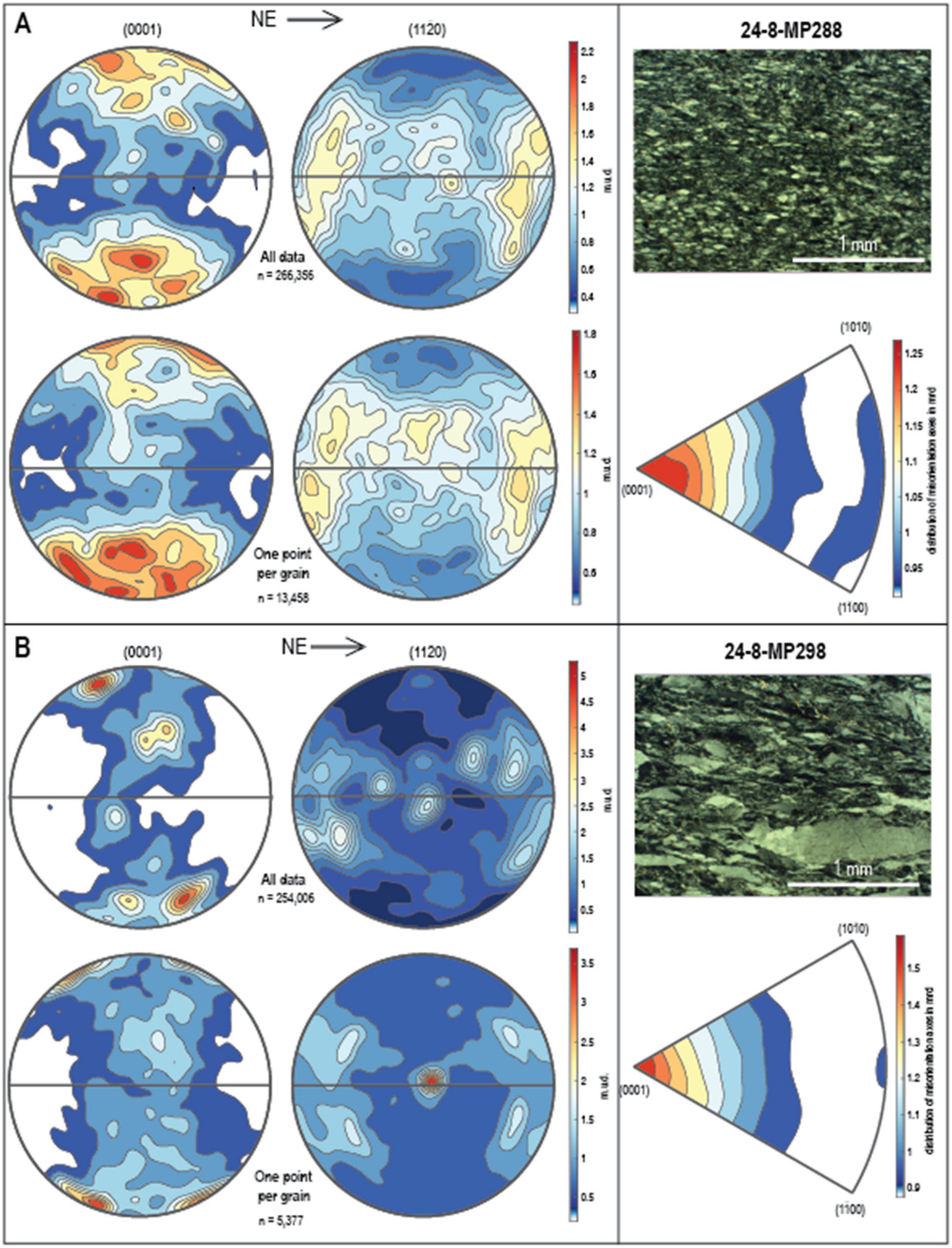

Figure 18: Quartz CPO c-axis and a-axis pole figures and inverse pole figures. Electron backscatter diffraction (EBSD) results (A-M) illustrating crystallographic fabrics across major structural domains. In each panel, c-axis (0001) and a-axis (1121) pole figures are shown, with pole figures constructed using all analyzed data displayed at the top and one point per grain shown at the bottom to emphasize grain-scale fabric development. On the right side of each panel, a cross-polarized light (XPL) photomicrograph of the sample is shown above the corresponding inverse pole figure. Panels A-H represent samples collected from within 10 m of the Deadman Creek thrust. Panels I-L show samples associated with the Duncan shear zone, reflecting fabrics developed during late Oligocene ductile shearing. Panel M corresponds to a sample from the Short Creek fault.

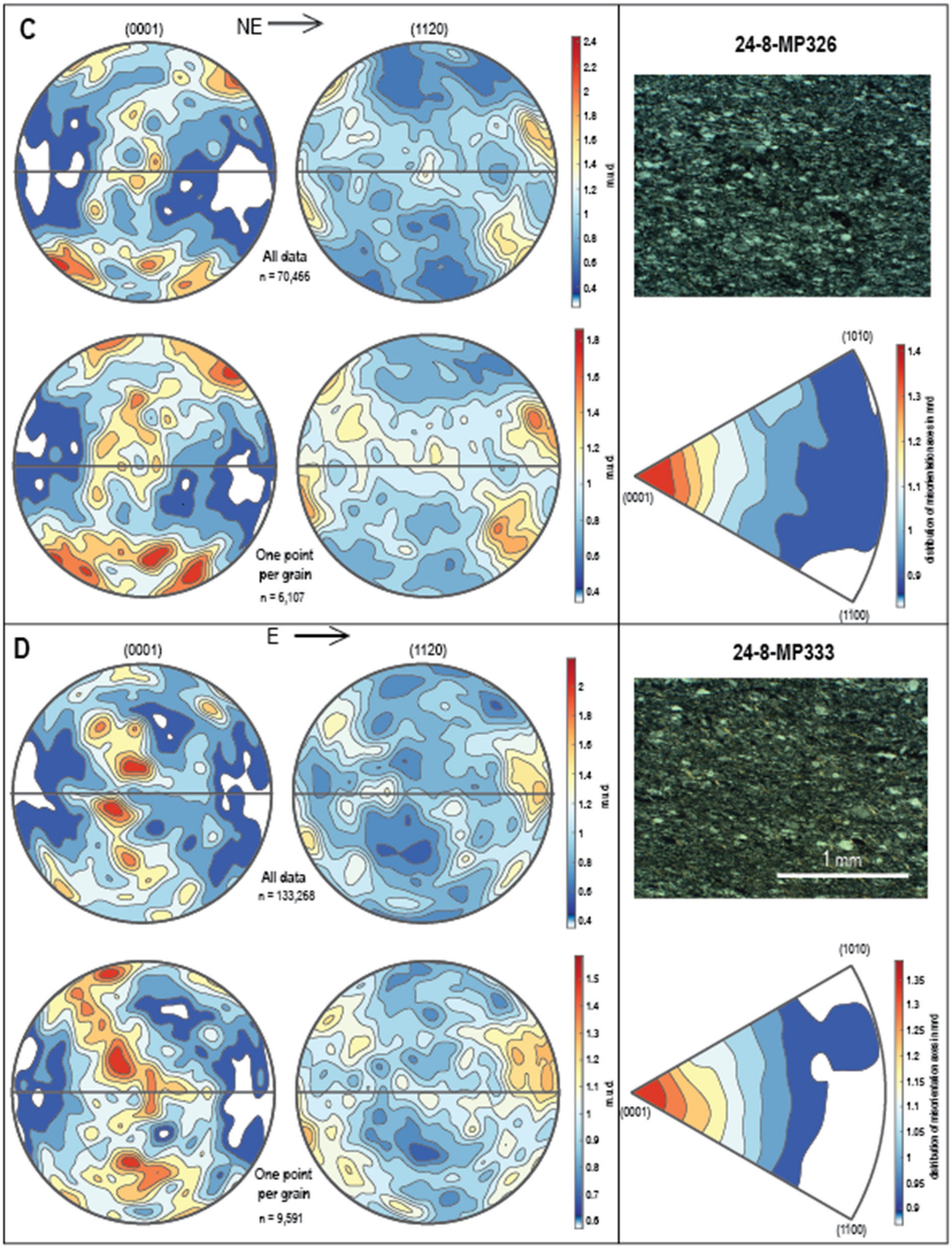
C
(0001)
NE
(1120)
All data
n = 70,466
One point
per grain
n = 6,107
m.u.d.
24-8-MP326
(1010)
(0001)
(1100)
distribution of misorientation axes in mrd
D
(0001)
E
(1120)
All data
n = 133,268
One point
per grain
n = 9,591
m.u.d.
24-8-MP333
1 mm
(1010)
(0001)
(1100)
distribution of misorientation axes in mrd

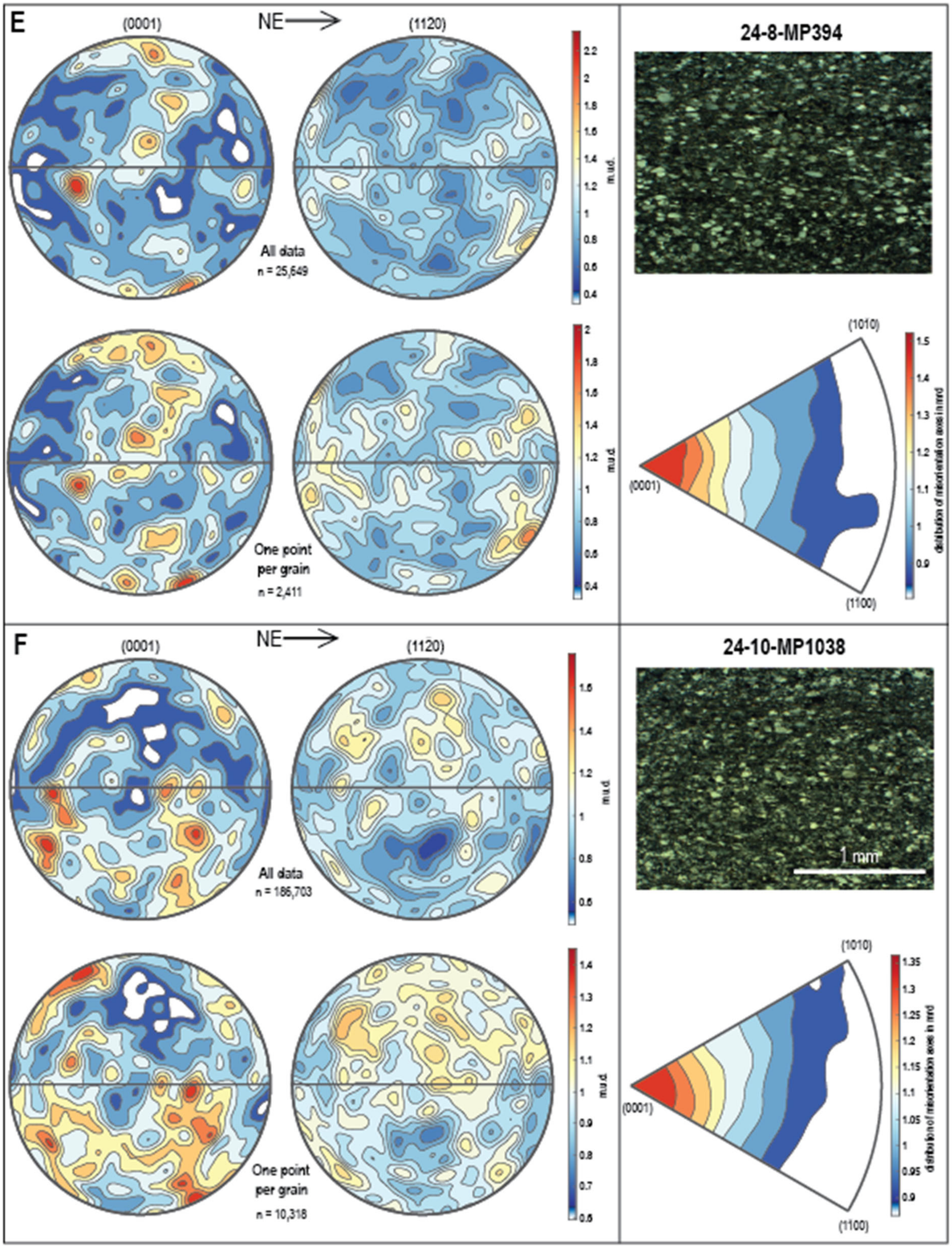

E
(0001)
NE
(1120)
m.u.d.
All data
n = 25,649
One point
per grain
n = 2,411
24-8-MP394
(1010)
(0001)
(1100)
distribution of misorientation axes in mrd
F
(0001)
NE
(1120)
m.u.d.
All data
n = 186,703
One point
per grain
n = 10,318
24-10-MP1038
1 mm
(1010)
(0001)
(1100)
distribution of misorientation axes in mrd

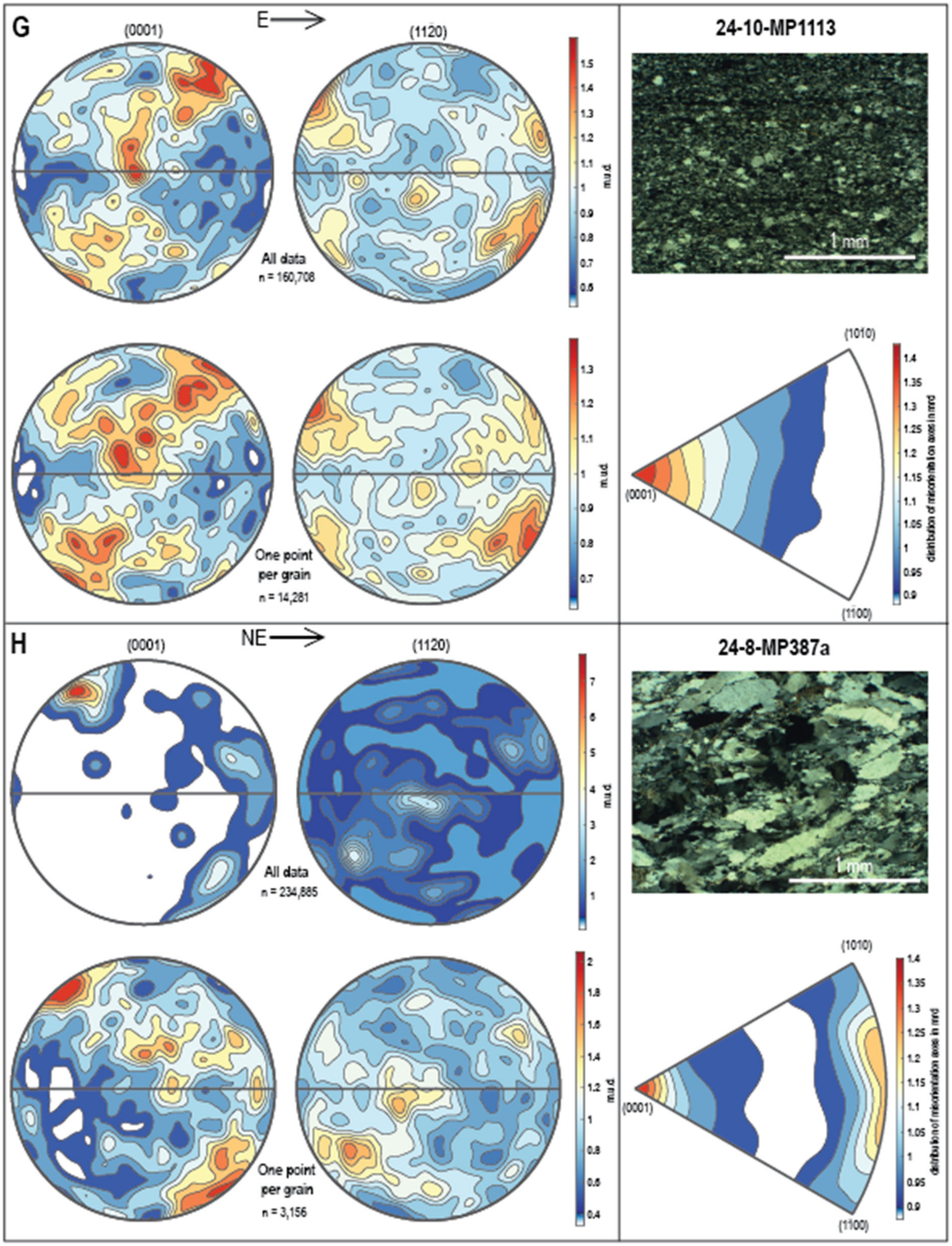
G
(0001)
E
(11$\bar{2}$0)
1.5
1.4
1.3
1.2
1.1
1
0.9
0.8
0.7
0.6
m.u.d.
All data
n = 160,708
1.3
1.2
1.1
1
0.9
0.8
0.7
m.u.d.
One point per grain
n = 14,281
24-10-MP1113
1 mm
(10$\bar{1}$0)
(0001)
(1$\bar{1}$00)
1.4
1.35
1.3
1.25
1.2
1.15
1.1
1.05
1
0.95
0.9
distribution of misorientation axes in mrd
H
(0001)
NE
(1120)
7
6
5
4
3
2
1
m.u.d.
All data
n = 234,885
2
1.8
1.6
1.4
1.2
1
0.8
0.6
0.4
m.u.d.
One point per grain
n = 3,156
24-8-MP387a
1 mm
(10$\bar{1}$0)
(0001)
(1$\bar{1}$00)
1.4
1.35
1.3
1.25
1.2
1.15
1.1
1.05
1
0.95
0.9
distribution of misorientation axes in mrd

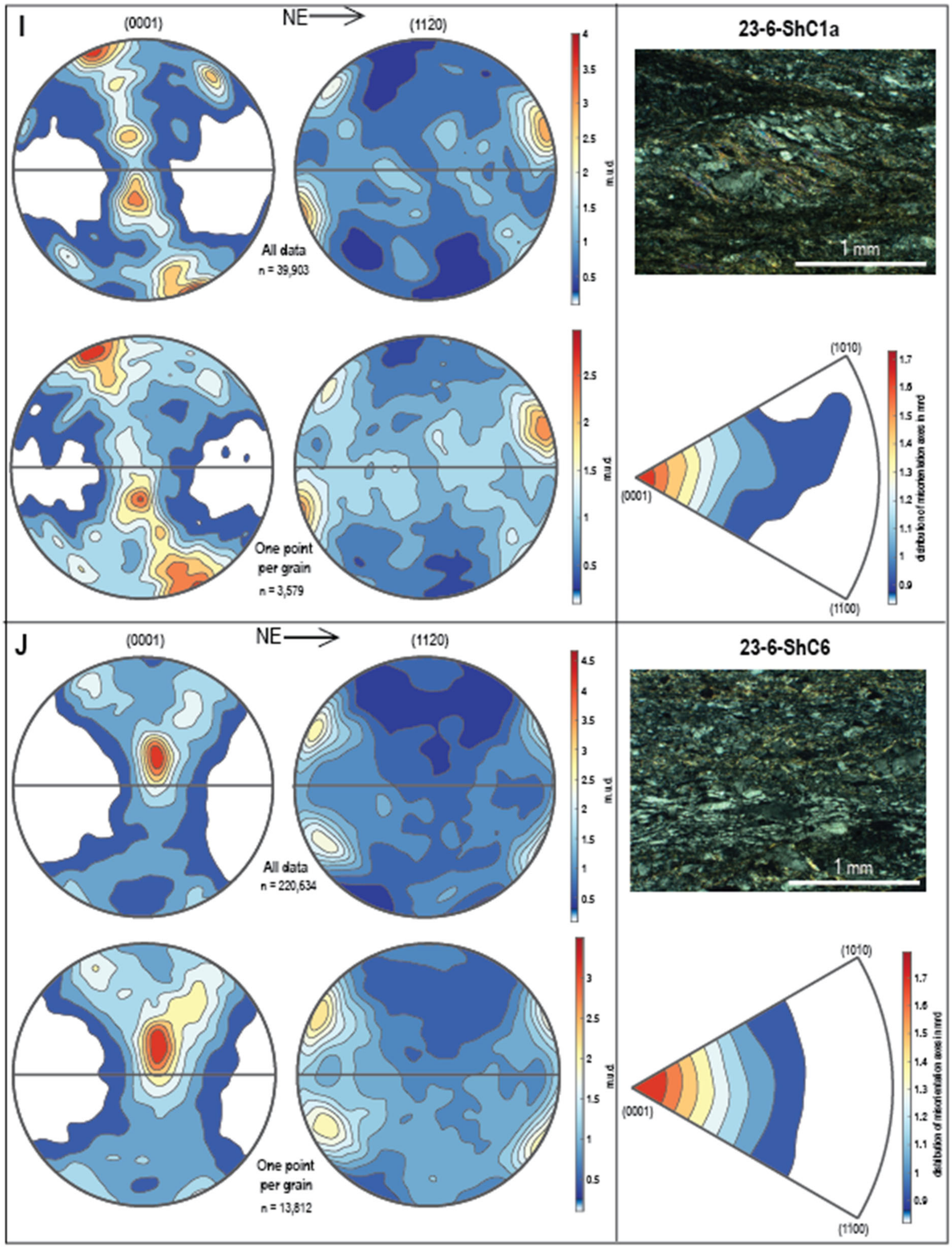
I
(0001)
NE
(1120)
m.u.d.
All data
n = 39,903
One point
per grain
n = 3,579
23-6-ShC1a
1 mm
(1010)
(0001)
(1100)
distribution of misorientation axes in mrd
J
(0001)
NE
(1120)
m.u.d.
All data
n = 220,634
One point
per grain
n = 13,812
23-6-ShC6
1 mm
(1010)
(0001)
(1100)
distribution of misorientation axes in mrd

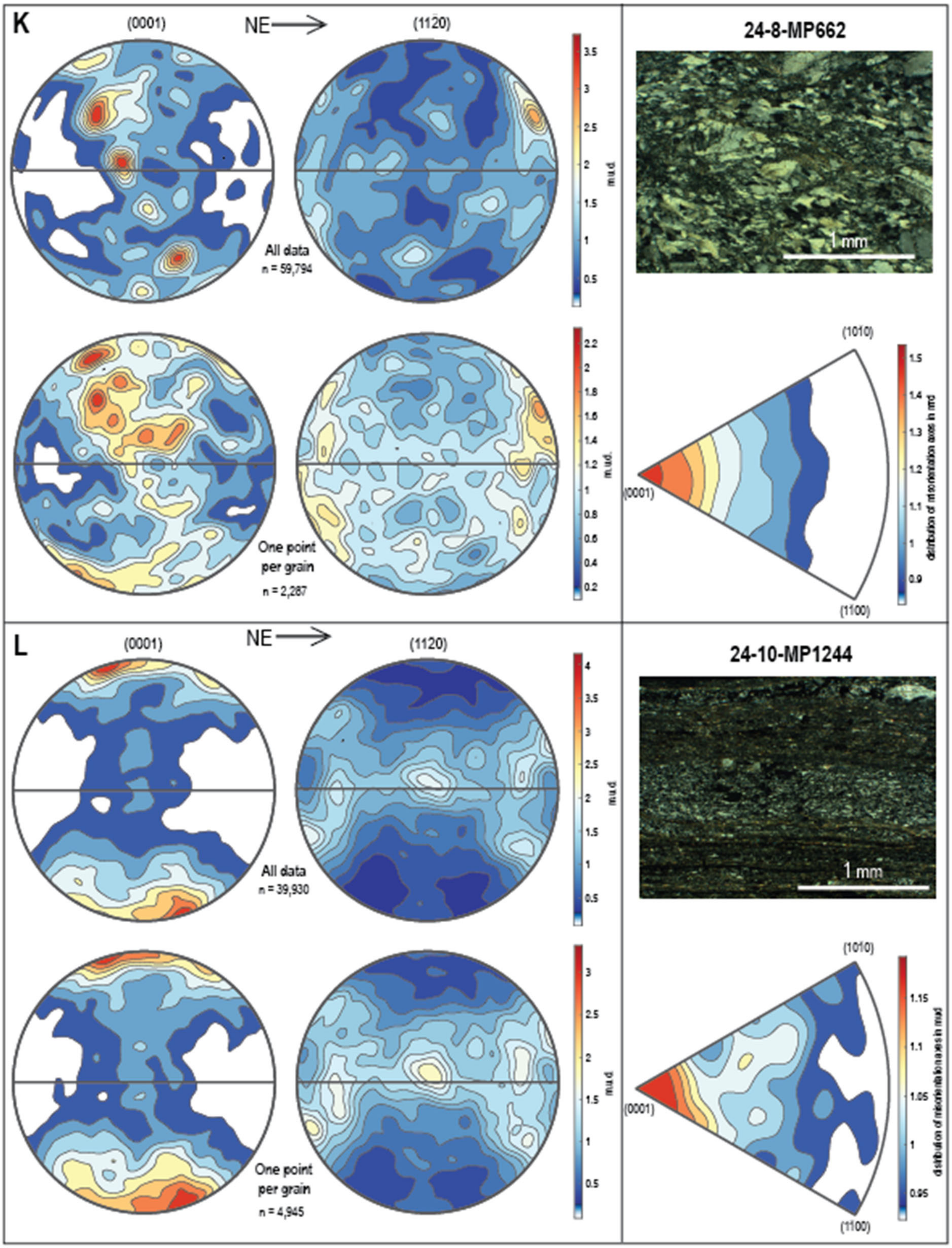
K
(0001)
NE
(1120)
m.u.d.
All data
n = 59,794
One point per grain
n = 2,287
24-8-MP662
1 mm
(1010)
(0001)
(1100)
distribution of misorientation axes in mrd
L
(0001)
NE
(1120)
m.u.d.
All data
n = 39,930
One point per grain
n = 4,945
24-10-MP1244
1 mm
(1010)
(0001)
(1100)
distribution of misorientation axes in mrd

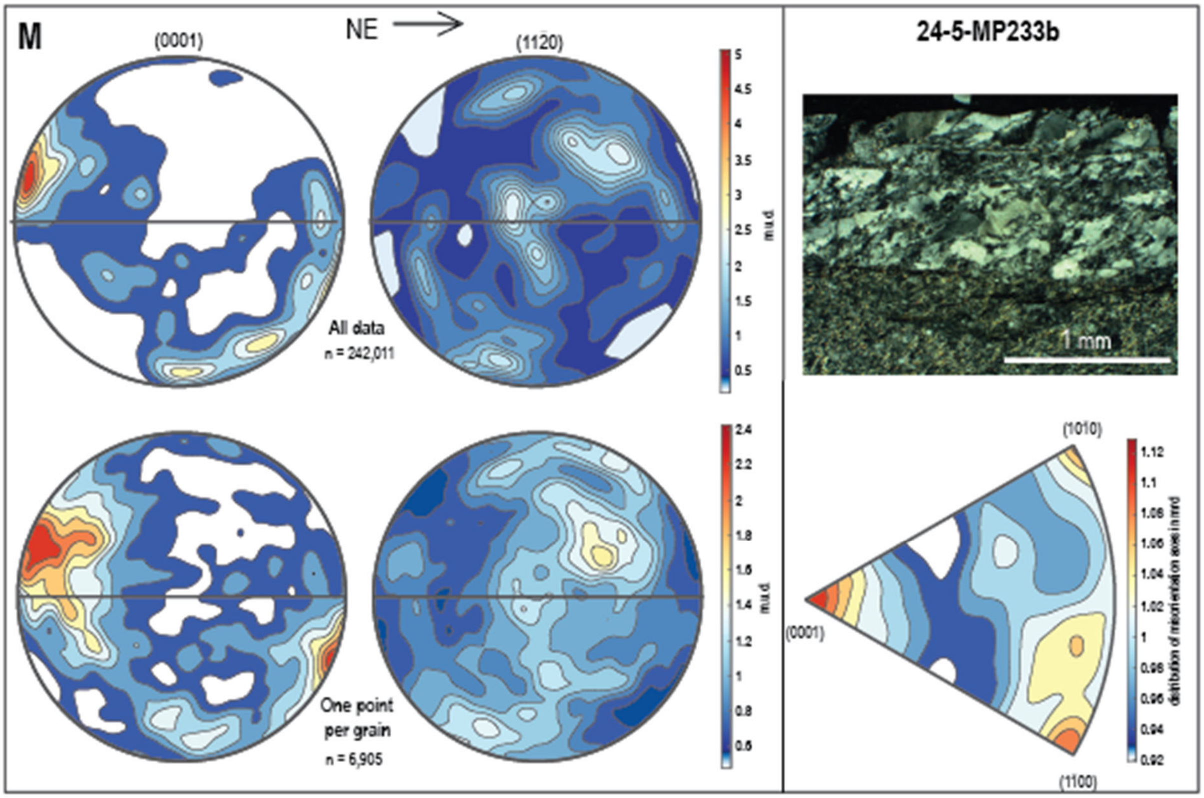
M
(0001)
NE →
(1120)
5
4.5
4
3.5
3
2.5
2
1.5
1
0.5
m.u.d.
All data
n = 242,011
2.4
2.2
2
1.8
1.6
1.4
1.2
1
0.8
0.6
m.u.d.
One point per grain
n = 6,905
24-5-MP233b
1 mm
(1010)
(0001)
(1100)
1.12
1.1
1.08
1.06
1.04
1.02
1
0.98
0.96
0.94
0.92
distribution of misorientation axes in mrd

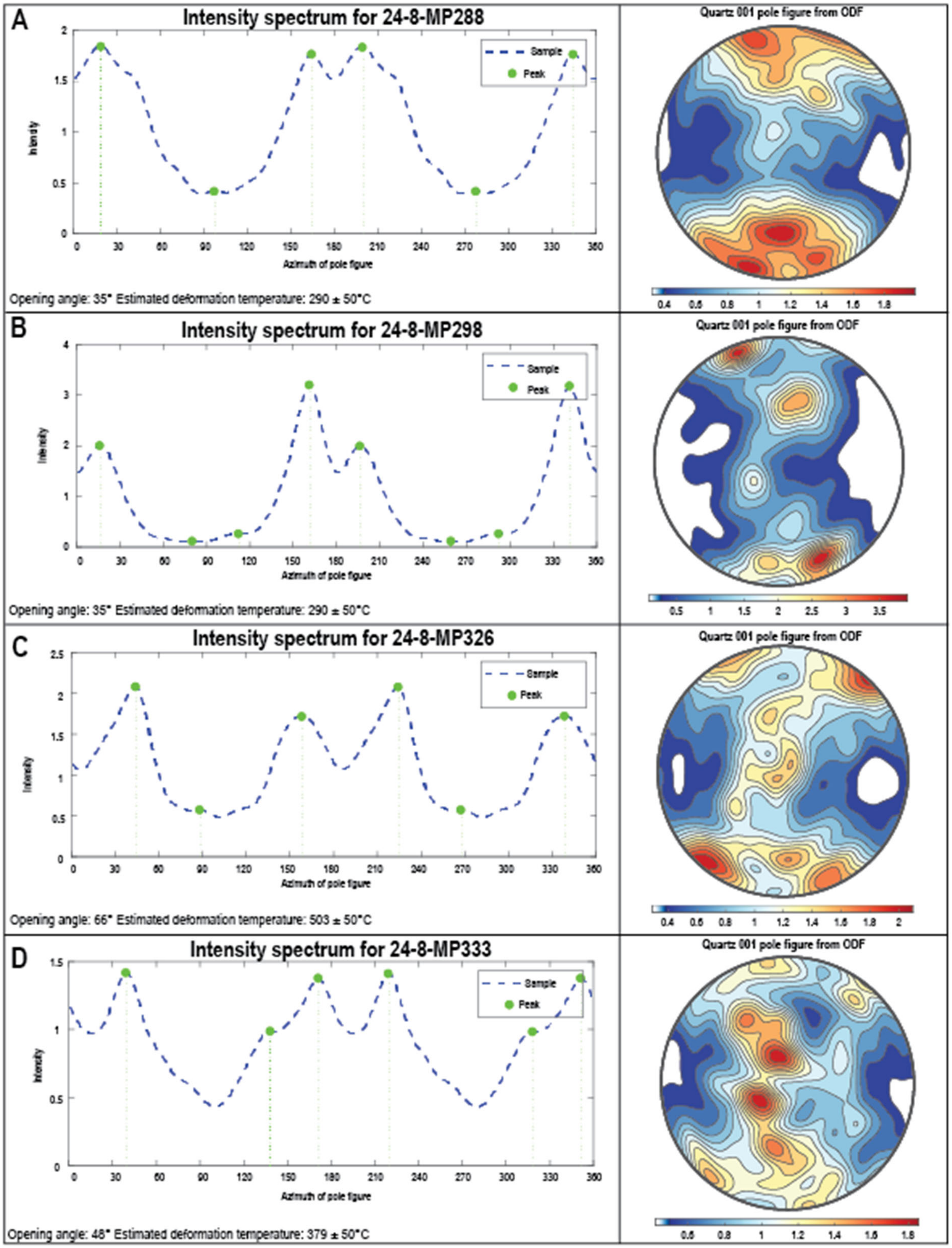

Figure 19: Quartz intensity spectrums and c-axis ODF pole figures. Orientation distribution function (ODF) pole figures (right) and ODF-derived intensity spectra samples A-M, corresponding to the same samples and panel arrangement shown in Figure 17. Estimated deformation temperatures are shown for each sample based on the opening angles, which are calculated using the methods in Hunter, et al., 2018.

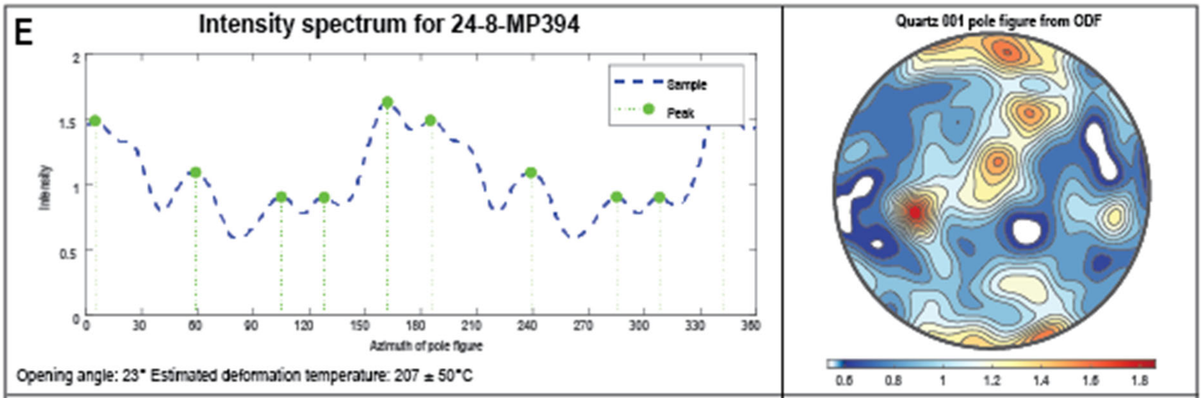

Opening angle: 23° Estimated deformation temperature: 207 ± 50°C

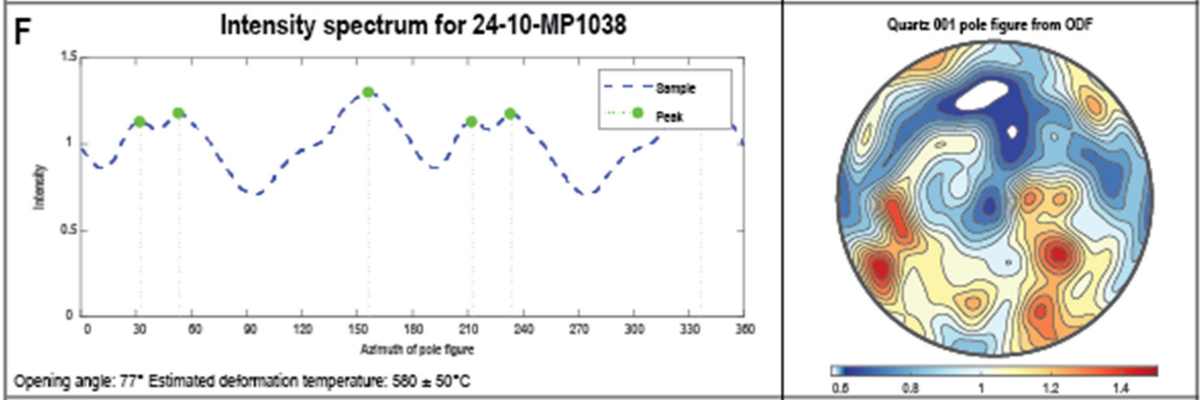

Opening angle: 77° Estimated deformation temperature: 580 ± 50°C

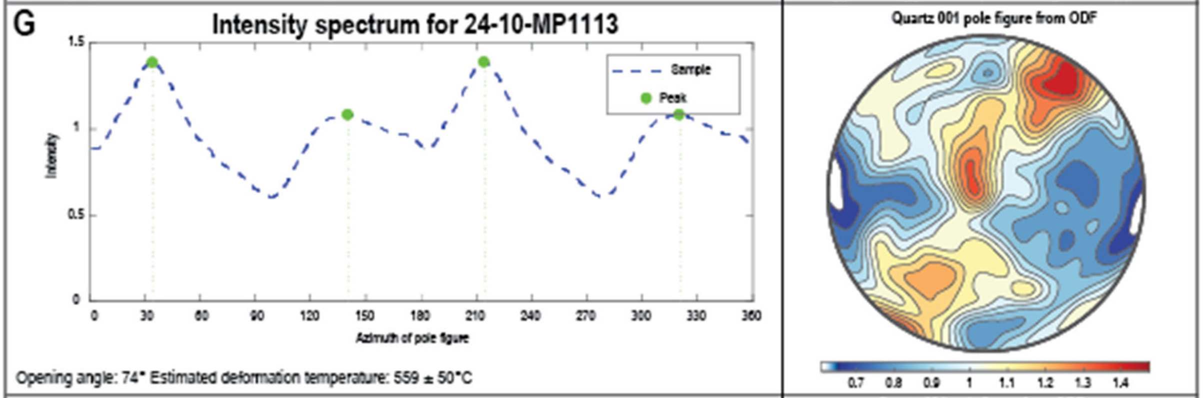

Opening angle: 74° Estimated deformation temperature: 559 ± 50°C

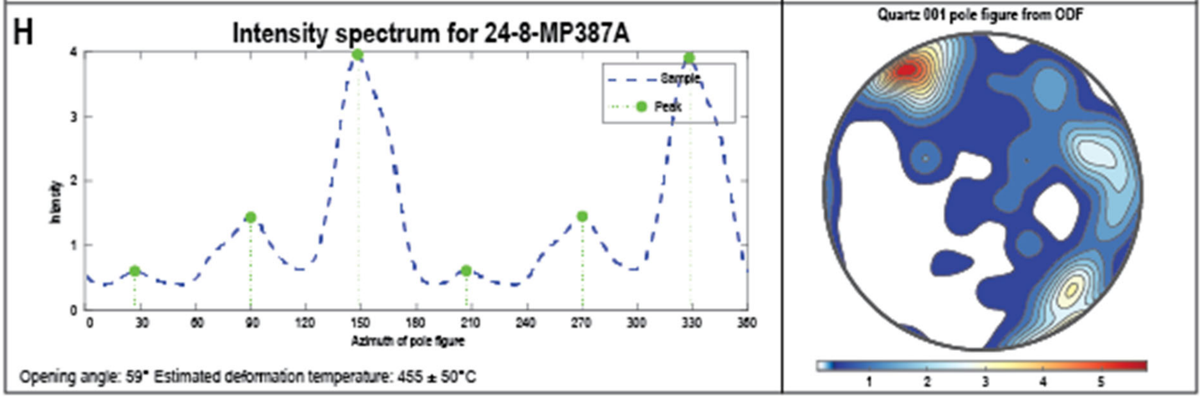

Opening angle: 59° Estimated deformation temperature: 455 ± 50°C

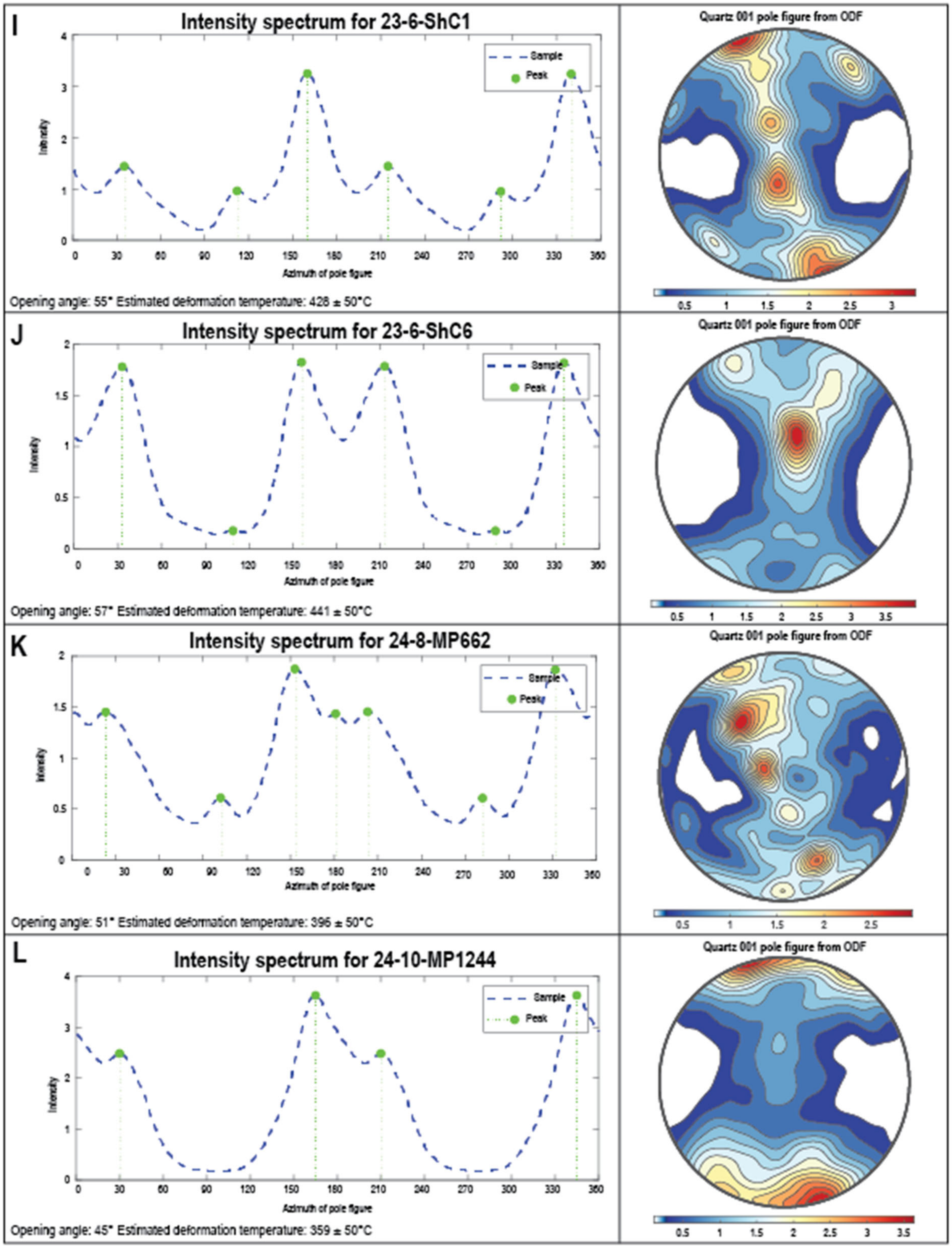
I
Intensity spectrum for 23-6-ShC1
Intensity
Azimuth of pole figure
Sample
Peak
Opening angle: 55° Estimated deformation temperature: 428 ± 50°C
Quartz 001 pole figure from ODF
0.5 1 1.5 2 2.5 3
J
Intensity spectrum for 23-6-ShC6
Intensity
Azimuth of pole figure
Sample
Peak
Opening angle: 57° Estimated deformation temperature: 441 ± 50°C
Quartz 001 pole figure from ODF
0.5 1 1.5 2 2.5 3 3.5
K
Intensity spectrum for 24-8-MP662
Intensity
Azimuth of pole figure
Sample
Peak
Opening angle: 51° Estimated deformation temperature: 396 ± 50°C
Quartz 001 pole figure from ODF
0.5 1 1.5 2 2.5
L
Intensity spectrum for 24-10-MP1244
Intensity
Azimuth of pole figure
Sample
Peak
Opening angle: 45° Estimated deformation temperature: 359 ± 50°C
Quartz 001 pole figure from ODF
0.5 1 1.5 2 2.5 3 3.5

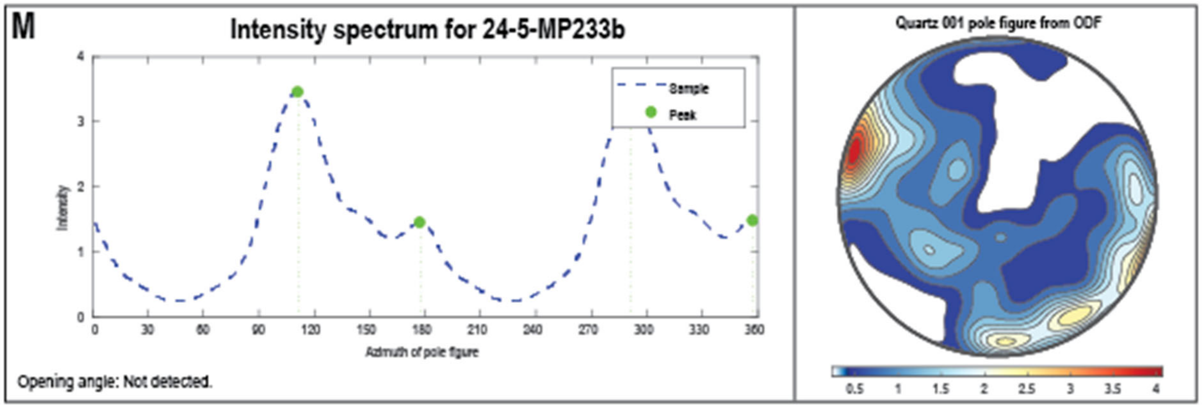
M
Intensity spectrum for 24-5-MP233b
Sample
Peak
Intensity
0
1
2
3
4
0
30
60
90
120
150
180
210
240
270
300
330
360
Azimuth of pole figure
Opening angle: Not detected.
Quartz 001 pole figure from ODF
0.5
1
1.5
2
2.5
3
3.5
4

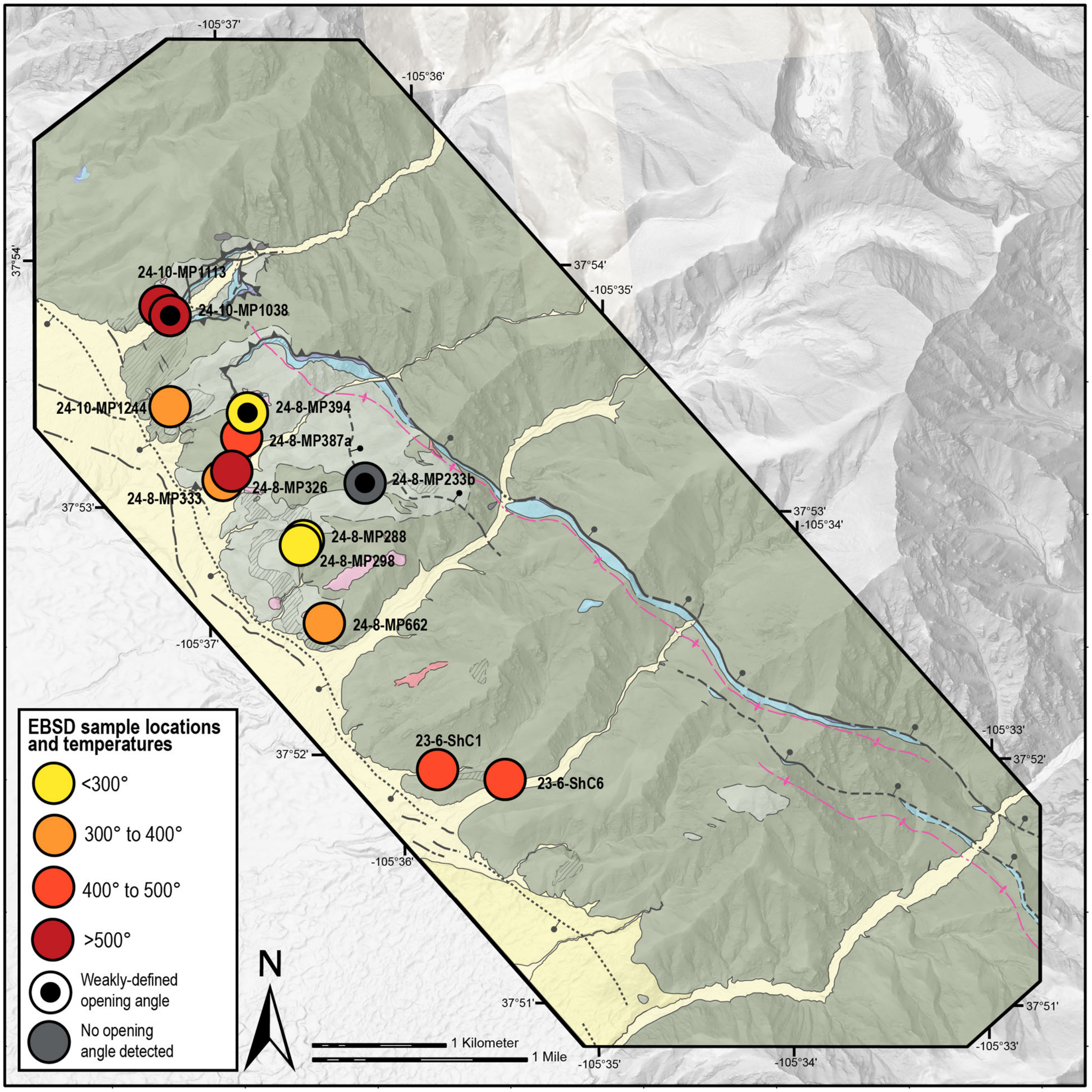

Figure 20: Simplified map of the study area with distribution of deformation temperatures derived from quartz c-axis opening angles. Simplified geologic map of the Deadman Creek thrust with circles showing the spatial distribution of EBSD data (A-M) as well as the interpreted deformation temperature for each sample based on quartz c-axis opening angles and the Faleiros et al. (2016) calibration. Data points with black center points have weakly defined opening angles. Grey circles indicate samples in which no opening angle was detected. The color of the circles indicates approximate deformation temperature (red >500° to yellow <300°).

2.10 Geochronology

2.10.1 Zircon U-Pb Geochronology

LA-ICP-MS U-Pb analysis of zircon grains separated from granodiorite sample 23-6-ShC1, collected from a drainage along the range front ~350 m northwest of Short Creek, yielded 18 concordant ages that cluster within the middle Oligocene, with a weighted mean age of 27.92 ± 0.32 Ma (at 2σ with MSWD = 4.1; Figure 21, Table 2). The granodiorite is mylonitic to protomylonitic, records top-SW sense of shear and intrudes Proterozoic gneiss. Both the granodiorite and gneiss are chloritized and are difficult to distinguish from each other.

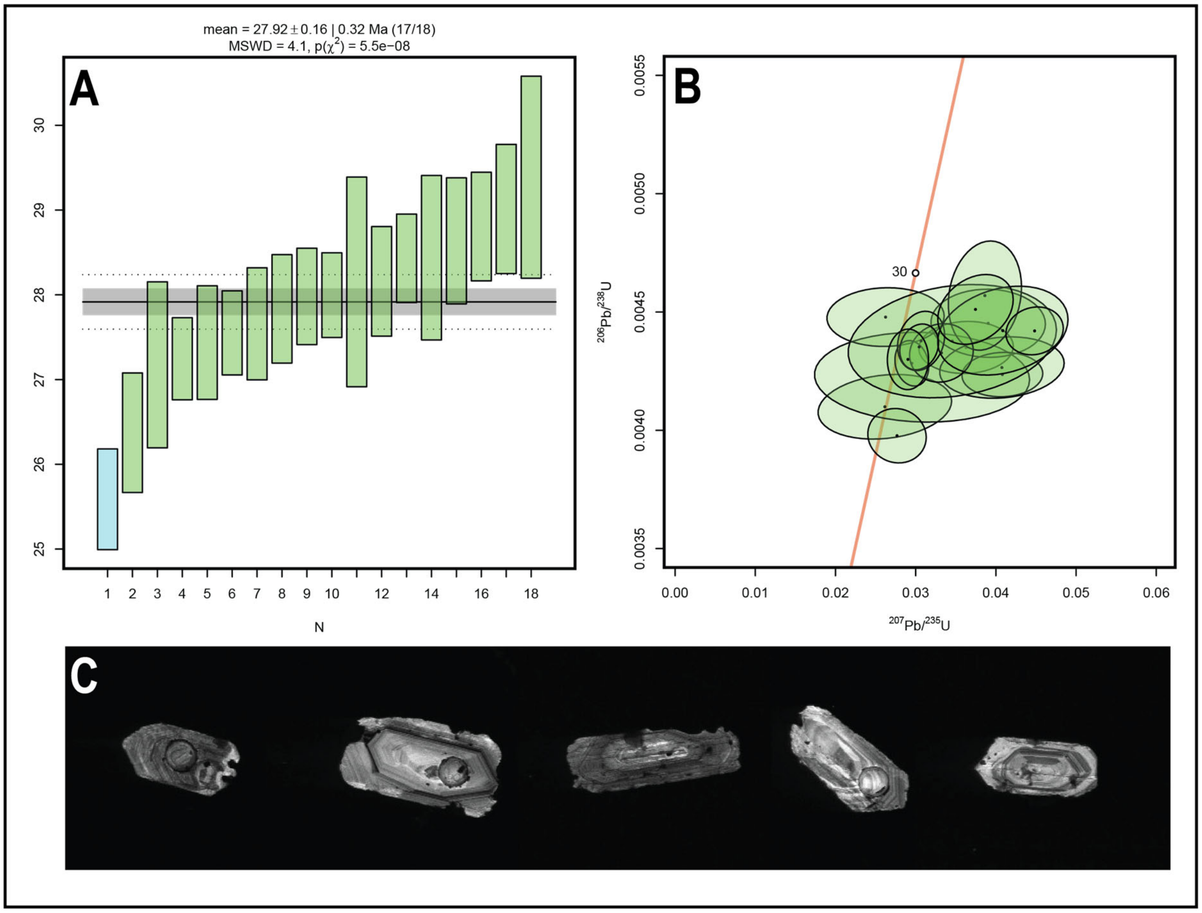

Figure 21: U-Pb zircon geochronology of granodiorite (Tgd). U-Pb zircon geochronology results for sample 23-6-ShC1. (a) Weighted mean $^{206}Pb/^{238}U$ age plot of *n* = 18 concordant zircons, yielding a calculated age of 27.92 ± 0.32 Ma. The blue bar is the date rejected by the outlier algorithm. (b) Wetherill concordia plot of the analyzed grains. (c) Cathodoluminescence (CL) images of representative zoned zircons; rims reflect igneous rather than metamorphic growth. Analysis spots are 40 µm in diameter.

Cathodoluminescence (CL) imaging of zircon grains from this sample reveals clear oscillatory igneous zoning (Figure 21c), confirming that the zircons are igneous origin, and dates from ablated spots record igneous crystallization rather than metamorphic zircon growth (Corfu et al.,

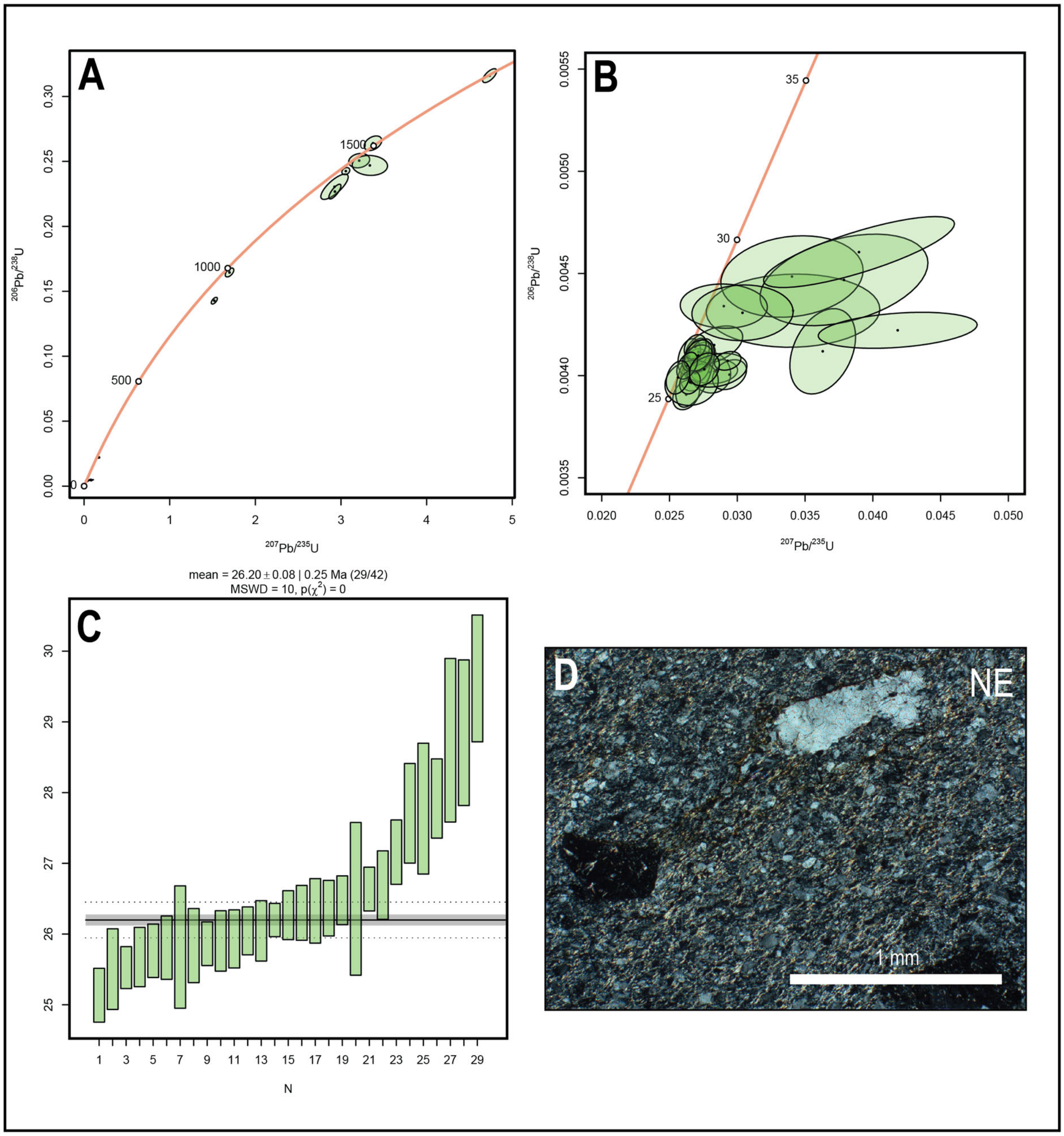

Figure 22: U-Pb zircon geochronology of aplite (Ta). U-Pb zircon geochronology results for sample 24-5-MP233b. (a) Wetherill concordia diagram showing all zircon analyses (n = 42). (b) Concordia diagram showing filtered analyses after exclusion of inherited grains (n = 10) and analyses with error ellipses that plot significantly off the concordia curve (n = 3). (c) Weighted mean ^{206}Pb/^{238}U age plot for the remaining zircon analyses (n = 29), yielding a crystallization age of 26.20 ± 0.25 Ma. (d) Photomicrograph of aplite dike at 5x magnification, showing feldspar phenocrysts within a fine-grained matric of quartz, feldspar, and white mica.

2003). The presence of well-zoned zircons and the concordant Oligocene U-Pb zircon ages collectively provide a ~28 Ma upper age constraint on mylonitization of the intrusion.

LA-ICP-MS U-Pb analysis of zircon grains separated from sample 24-5-MP233b, an aplite dike along a strand of the NE-dipping Short Creek fault system, yielded 29 concordant Oligocene dates. There are also populations of discordant Proterozoic grains that are interpreted as inherited zircons and were not included in the age calculation for this sample. The weighted mean age of included grains is 26.20 ± 0.25 Ma (at 2σ with MSWD = 10; Figure 22, Table 2). The weighted mean zircon age is characterized by a relatively high MSWD (10), indicating that the analyzed zircons do not statistically represent a single age population. Despite this scatter, the majority of analyses define a coherent population between ~25 and 27 Ma, interpreted to reflect the primary crystallization age. A tail of older ages extends from ~27 to 30 Ma; however, these analyses are not rejected by the outlier algorithm in IsoPlotR. If these older ages are removed from the dataset, it results in a slightly younger weighted mean age of 26.0 ± 0.17 Ma and a lower MSWD of 3.9. Because removing the older grains from the dataset does not significantly change the weighted mean age of the analyses, the weighted mean including all the grains is presented here, with the older discordant grains interpreted as possibly reflecting a minor component of antecrystic zircon or protracted zircon crystallization rather than a distinct magmatic event. The northeastern contact between the dike and Yqm is a well-developed normal fault surface with quartz slickenfibers that record oblique grain shape fabrics consistent with top-NE crystal-plastic deformation (Figure 22d). Emplacement of the dike along this fault zone and involvement in brittle-plastic normal-sense shear strongly suggests that the dike was emplaced synkinematic with motion along this strand of the Short Creek fault and thus the ~26 Ma zircon U-Pb date overlaps with development of this fault system.

2.10.2 USGS Zircon U-Pb Geochronology Data

A 2019 USGS data release (Holm-Denoma et al., 2019) includes LA-ICP-MS U-Pb zircon analyses from 10 samples collected in the Deadman Creek thrust area. Eight of these samples are of igneous or metamorphic origin and include four aplites (“felsites” in the USGS dataset), two rhyolitic porphyries, one chlorite-quartz mylonite, and one sample of augen gneiss. The interpreted ages from these units provide important temporal constraints on the crystalline basement, magmatism, and related structures in the Deadman Creek thrust area and are shown in Figure 23 and Table 2. Two of the samples (91113-13A and 52014-14A) from the 2019 data release are quartzites with detrital zircon signatures (Figure 25, Table 3).

Crystalline Basement Rocks

The sample of augen gneiss in the USGS dataset yielded a Mesoproterozoic age of 1439 ± 13 Ma (at 2σ with MSWD = 0.43; Figure 23e, Table 2). This confirms the correlation of this gneissic unit with the regional Music Pass pluton, which was emplaced around ~1.43 Ga (Jones and Connelly, 2006).

Aplite Intrusions and Rhyolitic Porphyries

The majority of aplites in the dataset yielded late Oligocene crystallization ages (Figure 23c, d, f, and g), which agree with our dated aplite sample (24-5-MP233b). Many inherited zircon grains are present in these samples, but the youngest zircon populations reflect magmatic crystallization ages between ~27–30 Ma, consistent with late Oligocene intrusive activity. Sample 91113-6B yielded a weighted mean age of 28.26 ± 1.44 Ma (at 2σ with MSWD = 7; Figure 23c, Table 2) from a population of 4 Oligocene zircons. The zircon grains in this sample that were used for the weighted mean age for sample 91113-6B exhibit high discordance (outside of the range of < −5% and > 20% discordance) but they were retained in the dataset for age calculations. Sample 91213-22A similarly yielded an age of 29.6 ± 2.6 Ma (at 2σ with MSWD = 8; Figure 23d, Table 2) from a population of 2 concordant zircons. Sample 52015-6A yielded an age of 26.7 ± 0.09 Ma (at 2σ with MSWD = 1.2; Figure 23f, Table 2) from a population of 30 zircons. This sample recorded many more Oligocene zircons than the other aplite/felsite samples in the USGS dataset. Sample 91917-3A is sample of felsite, though it appears to record only inherited zircons from the Proterozoic gneiss and yielded a weighted mean age of 1657 ± 13 Ma (at 2σ with MSWD = 0.7; Figure 23g, Table 2) from a population of 17 zircons.

The samples of rhyolitic porphyries from the USGS dataset both record Proterozoic ages, possibly documenting inherited zircon ages from the Proterozoic basement. Sample 91013-5A yielded an age of 1616 ± 29 Ma (at 2σ with MSWD = 90; Figure 23b, Table 2) from a population of 44 zircons. Sample 91917-5B yielded an age of 1681 ± 11 Ma (at 2σ with MSWD = 2; Figure 23h, Table 2) from a population of 22 zircons.

Chlorite-quartz mylonite

Notably, the sample of chlorite-quartz mylonite (90913-3A) yielded a wide range of zircon ages (Figure 23a), with at least three distinct age populations: ~1.38–1.46 Ga, ~1.60–1.74 Ga, and ~27–31 Ma. The Oligocene zircons (concordant, n=2) yielded an average age of 27.8 ± 3.1 Ma (at 2σ with MSWD = 30; Figure 23a, Table 2). The $^{238}U/^{206}Pb$ ages of the individual grains are 27 ± 1 Ma and 31 ± 1 Ma. These zircons have U/Th ratios of 0.9–1.1, suggesting igneous, not metamorphic, crystallization ages (Kirkland et al., 2018). These Oligocene zircons may represent an Oligocene intrusion in an otherwise Proterozoic and Mesoproterozoic mylonite protolith. Because the range of ages in this sample spans from Proterozoic to Oligocene, this sample reflects the complex history of protolith emplacement followed by later magmatism and mylonitic deformation.

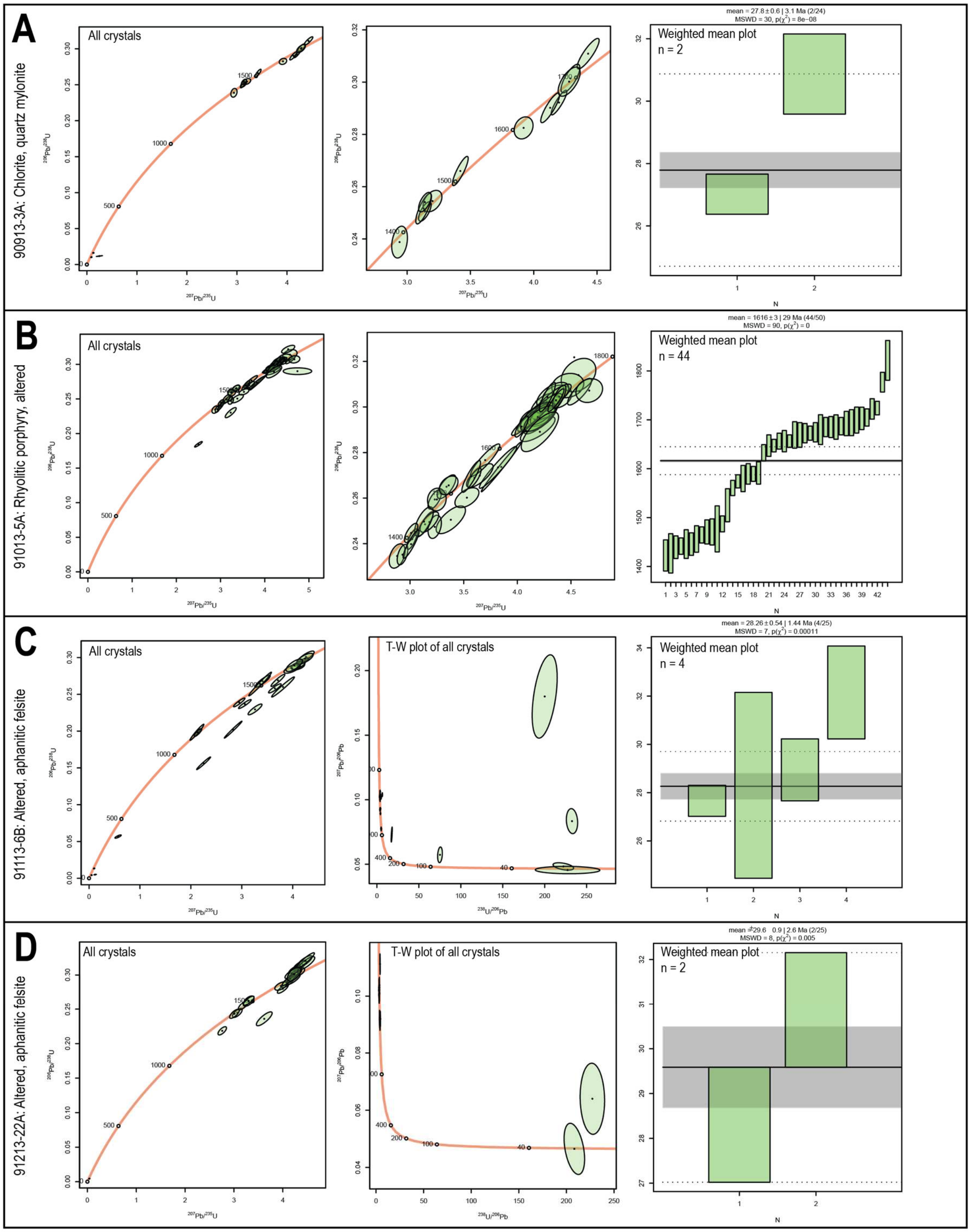

Figure 23: U–Pb zircon geochronologic data from the USGS Deadman Creek data release (Holm-Denoma et al., 2019). Sample locations and interpreted ages are reported in Table 2. (a) Sample 90913-3A, chlorite-quartz mylonite. Wetherill concordia plot showing all analyses, a concordia plot highlighting the inherited populations, and a weighted mean ^{206}Pb/^{238}U age calculated from n = 2 concordant Oligocene grains. (b) Sample 91013-5A, altered rhyolitic porphyry. Wetherill concordia plot of all analyses, a concordia plot showing the dominant popuation, and a weighted mean plot with n = 44 analyses. (c) Sample 91113-6B, altered aphanitic felsite/aplite. Wetherill concordia plot of all zircon analyses, a Tera-Wasserburg plot of all analyses, and a weighted mean ^{206}Pb/^{238}U age calculated from n = 4 concordant Oligocene grains. (d) Sample 91213-22A, altered aphanitic aplite. Weighted mean plot of all analyses, a Tera-Wasserburg plot of all analyses, and a weighted mean ^{206}Pb/^{238}U age based on n = 2 concordant Oligocene grains.

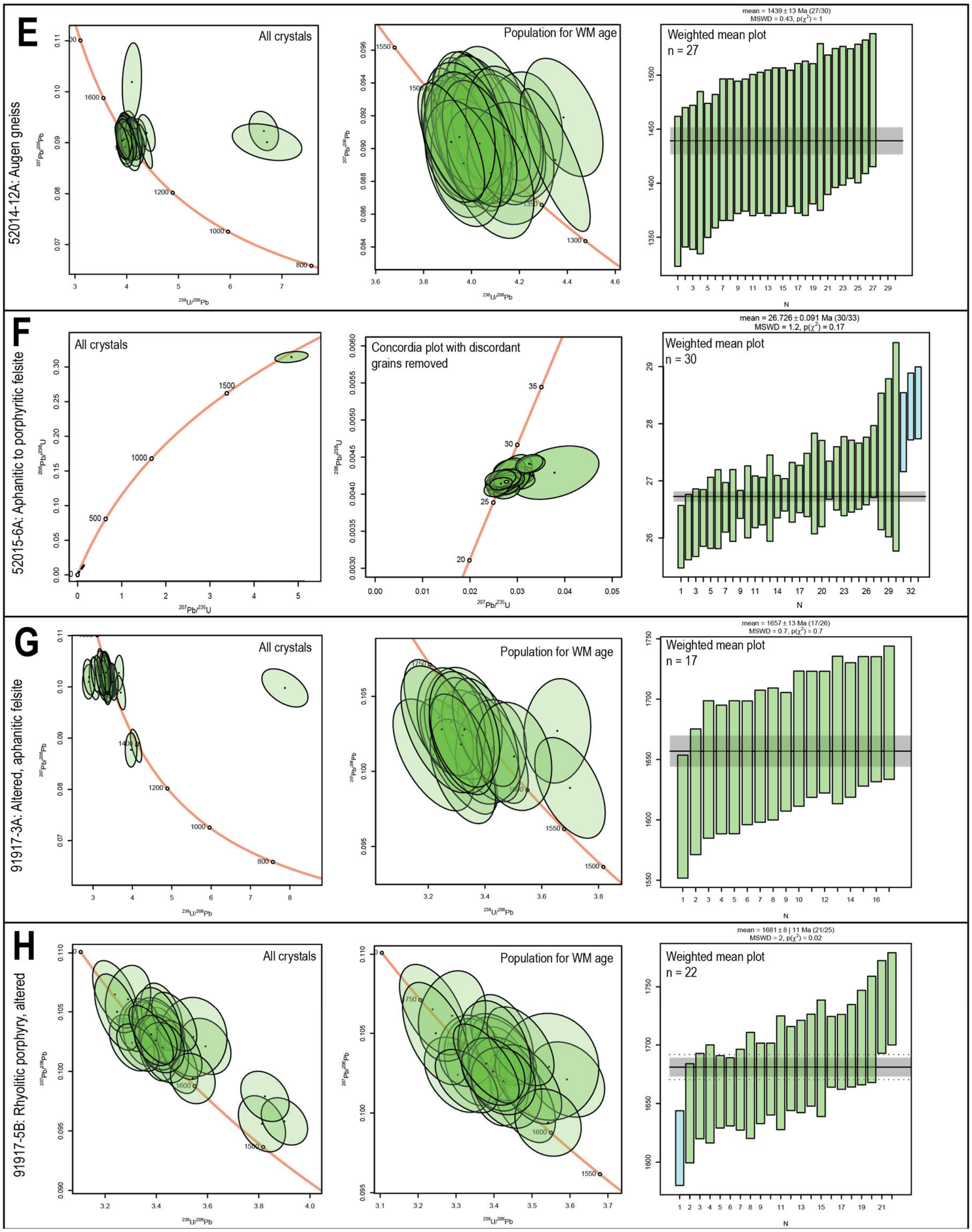

Figure 23 Cont: (e) Sample 52014-12A, augen gneiss. Tera-Wasserburg plot showing all zircon analyses, a Tera-Wasserburg plot highlighting the population used to calculate the weighted mean age, and a weighted mean ^{206}Pb/^{238}U age based on n = 27 grains. (f) Sample 52015-6A, aphanitic to porphyritic felsite. Wetherhill concordia plot showing all zircon analyses and a condordia plot with discordant analyses removed. A weighted mean plot with n = 30 condordant grains. (g) Sample 91917-3A, altered aphanitic felsite. Tera-Wasserburg plot of all zircon analyses, a Tera-Wasserburg plot highlighting the population used to calculate the weighted mean age, and a weighted mean ^{206}Pb/^{238}U age based on n = 17 grains. (h) Sample 91917-5B, altered rhyolitic porphyry. Tera-Wasserburg plot showing all zircon analyses, a Tera-Wasserburg plot highlighting the population used to calculate the weighted mean age, and a weighted mean ^{206}Pb/^{238}U age based on n = 22 grains.

Quartzite Detrital Zircon Data

Two quartzite samples from the 2019 USGS data release were analyzed for detrital zircon signatures (Figure 24). The results of the analyses for sample 91113-13A from the south side of Deadman Creek (see Figure 4) clearly matches the detrital zircon provenance signature for the Ordovician Harding Formation, with peaks at ~1.8 Ga and ~2.7 Ga (see Figure 6e in Holm-Denoma et al., 2022). On the other hand, the detrital zircon results for 52014-14A from quartzite on the north side of Deadman Creek (Figure 4) are more ambiguous but suggest a detrital zircon signature similar to Cambrian sandstone units, such as the Sawatch Formation, which contains detrital zircon provenance peaks at ~1.4 Ga and ~1.7 Ga (see Figure 6e in Holm-Denoma et al., 2022). Similar to the Harding Formation quartzite, this Cambrian quartzite unit depositionally overlies the Mesoproterozoic quartz monzonite and is currently mapped as the Harding Formation. However, its detrital zircon signature suggests that at least locally, Cambrian strata

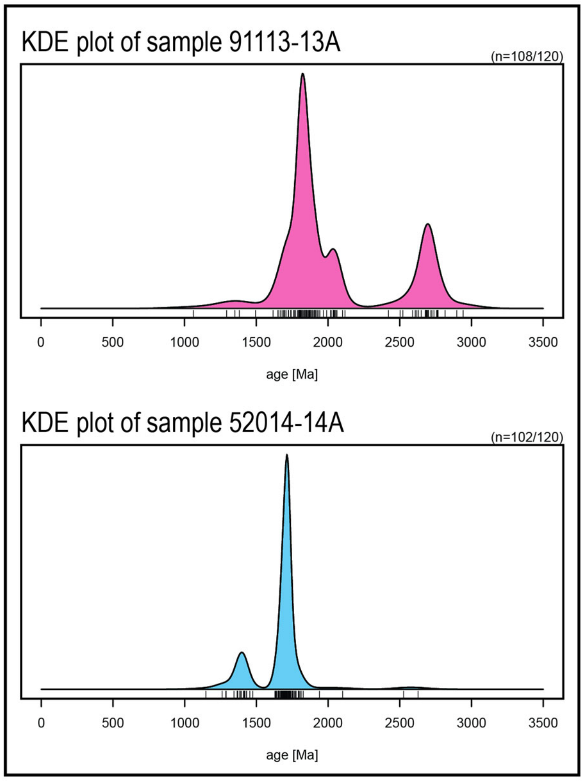

Figure 24: KDE plots of detrital zircon data from quartzites in the study area. Kernel density estimate (KDE) plots of U-Pb detrital zircon ages comparing samples 91113-13A and 52014-14A from Holm-Denoma et al., 2019. KDEs are constructed from concordant analyses (-5 to ≤ 20% discordance; n = 107 and 102, respectively). The age distribution for 91113-13A is characterized by prominent peaks at ~1.8 Ga and ~2.7 Ga, closely matching the established detrital zircon provenance signature of the Ordovician Harding Formation. The KDE plot for 52014-14A displays a more ambiguous provenance signature. The distribution includes dominant peaks at ~1.4 Ga and ~1.7 Ga, similar to those documented in Cambrian sandstone units such as the Sawatch Formation. Although this unit depositionally overlies Mesoproterozoic quartz monzonite and is currently mapped as Harding Formation, its detrital zircon signature suggests that Cambrian strata may be locally preserved in the study area.

may be preserved. These units are lithologically similar and cannot be reliably distinguished in the field.

2.10.3 Apatite U-Pb Geochronology

One bulk sample (SLM_D64) was collected from a dark green to black, medium- to coarse-grained gabbro body that intrudes the Proterozoic gneiss and locally has a finer-grained, quenched margin near the contact. This sample did not yield any zircons, so we dated apatite via U-Pb LA-ICP-MS. The apatites from this sample yielded a Terra-Wasserburg lower intercept date of 485 ± 86 Ma (Figure 25, Table 2). This low-precision date overlaps with Cambrian-Ordovician intrusions that have been documented in the Wet Mountains, ~35 km to the N and NE (Magnin et al., 2023; Smith et al., 2023), suggesting this gabbro is also associated with a cryptic rifting event that may have extended from southern Oklahoma to southern Colorado. In another location in the field area, between Alpine Creek and Deadman Creek, this gabbro appears to be depositionally overlain by the Middle Ordovician Harding Formation rather than intruding into the Harding Formation. The gabbro displays well-defined intrusive contacts with the surrounding basement gneiss, and no evidence of contact metamorphism was observed in the

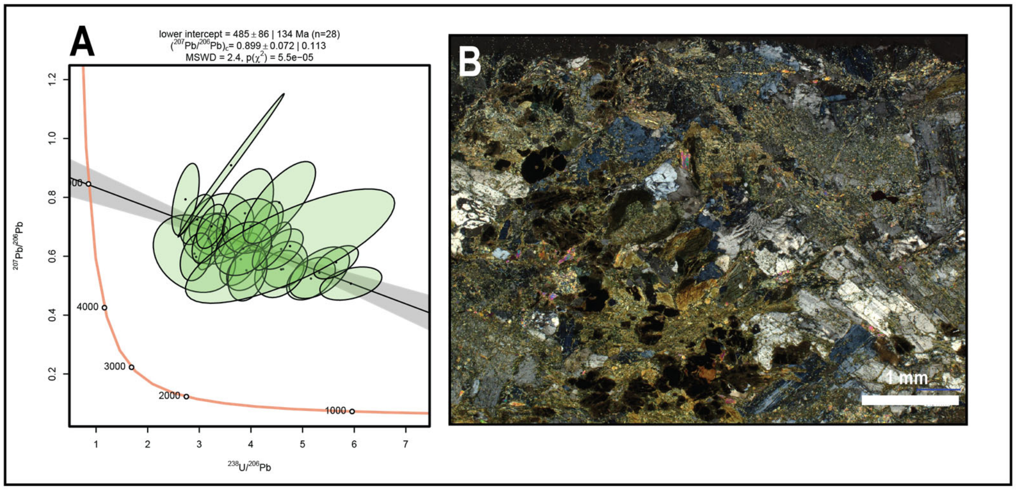

Figure 25: U-Pb apatite geochronology of gabbro (Cg). (a) Terra-Wasserburg concordia diagram showing apatite U–Pb analyses from gabbro sample SLM_DM64. A total of 29 apatite grains were analyzed, yielding a lower intercept age of 485 ± 85 Ma, interpreted as the timing of apatite crystallization and/or subsequent thermal resetting associated with gabbro emplacement. (b) Cross-polarized light (XPL) photomicrograph of the gabbro (sample SLM_DM64).

overlying Harding Formation, supporting the interpretation that the intrusion predates its deposition and is Cambrian-Ordovician in age. Cambrian-age magmatism has not previously been documented in the Sangre de Cristo Mountains.

4. DISCUSSION

2.11 Structural evolution of the Deadman Creek thrust

The structural framework of the Deadman Creek area records a complex deformational history involving multiple tectonic episodes, including Proterozoic magmatism, Laramide contraction, and Rio Grande rift-related extension and magmatism. The Deadman Creek thrust represents the dominant contractional structure in the region, placing Proterozoic crystalline basement over Paleozoic metasedimentary rocks (MDO). The thrust is associated with mylonitic foliation and top-NE shear sense indicators, supporting a NE-directed transport direction during Laramide shortening. In the eastern portion of the exposure along Deadman Creek, the thrust records exclusively the top-NE strain within a relatively thin (<10 m) mylonitic shear zone in the footwall developed primarily within carbonate-rich MDO strata. Here, top-NE shear fabrics are well-developed, whereas overlying Proterozoic rocks in the hanging wall exhibit only weak protomylonite directly above the thrust. These field relationships suggest that strain was strongly partitioned into carbonate-rich units during thrust motion and that penetrative deformation of the hanging wall basement was limited.

The Deadman Creek thrust was later modified by NE-vergent folding, best seen in the geometry of the thrust surface and the orientation of foliations in both the hanging wall and footwall. Cross section profiles and stereographic projections confirm that this folding occurred along a shallow NW-trending axis, producing an asymmetric antiform where the thrust dips steeply to the NE. At least two distinct NE-vergent folds are recognized, locally characterized by near-vertical to overturned (steeply SW-dipping) NE limbs. These folds are interpreted as fault-propagation folds that reflect continued contraction accommodated by structurally lower, SW-dipping reverse faults that are not exposed at the surface but are likely present at depth (Figure 26). Such relationships are consistent with development of an in-sequence imbricate thrust system that propagated northeastward, with the Deadman Creek thrust representing one of the uppermost and more exposed structural levels within that system.

Overprinting these contractional structures is a system of normal faults, collectively termed the Short Creek fault system. These NE-dipping faults commonly localize along the steeply-dipping NE limb of the thrust and consistently exhibit top-NE (and locally oblique left-lateral/normal) brittle-plastic kinematic indicators, suggesting that they accommodated extensional strain. Notably, NE-dipping normal faults of this orientation are not observed elsewhere in the Sangre de Cristo Range, where the dominant Rio Grande rift fault system is characterized by moderately to steeply WSW-dipping, range-bounding normal faults. The anomalous dip direction and structural position of the Short Creek fault system therefore suggests that the pre-existing folded Deadman Creek thrust geometry (i.e., NE-dipping limbs of the folded Deadman Creek thrust) exerted a strong mechanical influence on the localization and orientation of rift-related extension. The extension direction represented by the Short Creek fault system (35°/16° from linked Bingham analysis) is at a high angle to the trend of the modern range front and consistent with regional Rio Grande rift strain patterns. The reactivation of older contractional features by these faults highlights a significant structural inheritance component in the earliest phases of rift development within the study area.

The Duncan shear zone, exposed discontinuously within Proterozoic basement and locally within the MDO, represents a younger episode of ductile deformation that overprints the earlier thrust fabric and associated contractional structures. It is most prominently developed in the northern part of the study area, particularly between Pole Creek and Deadman Creek, with an additional isolated exposure of similar mylonites just north of Sand Creek. The zone is characterized by a southwest-dipping geometry that locally shallows and appears to follow the contours of modern topography. Microstructural observations (e.g., SGR and BLG recrystallized quartz, fractured feldspar porphyroclasts, mica-defined S-C fabrics) as well as c-axis opening angle temperatures from Duncan shear zone samples (~359 to 441°C), as well as Deadman Creek thrust associated samples with top-SW shear (290° to 559°C), indicate deformation primarily at lower to upper greenschist-facies conditions. Thermochronology data suggest that the western flank of the range was ~200–270°C prior to Miocene exhumation (Singleton et al., 2024), and there is no evidence for significant rift-related unroofing before that time. Therefore, rocks in the Duncan shear zone were likely at ~7–9 km depth during Oligocene deformation and required thermal input from nearby magmatism to raise temperatures by several hundred degrees to produce greenschist facies microstructures and deformation temperatures.

Pervasive chlorite alteration within the shear zone suggests fluid-assisted deformation, potentially linked to syn-tectonic magmatism or hydrothermal circulation during shear zone development. Kinematic indicators record dominantly top-SW shear with some coaxial strain, reflecting overall general shear and subhorizontal WSW-ENE stretching during shear zone evolution. Although the shear zone appears to have locally nucleated along the preexisting Deadman Creek thrust, its overall distribution and geometry suggest that the location and emplacement of synkinematic magmatism exerted the primary control on deformation associated with the Duncan shear zone. The discontinuous nature of the exposures and variable thickness of mylonitic fabrics also suggests that the Duncan shear zone is structurally influenced by an intrusion at depth. Notably, the thickest and most continuous exposures of the shear zone differ throughout the study area: near Deadman Creek they occur in the hanging wall of the thrust, whereas near Duncan they lie within the footwall. This pattern contrasts strongly with the thrust-related top-NE fabrics in Deadman Creek, which are clearly localized along the thrust surface itself, further emphasizing that the geometry and location of the Duncan shear zone are more governed by magmatic emplacement than reactivation of the Deadman Creek thrust.

2.12 Timing of Magmatism and Deformation

Geochronologic data from U-Pb zircon analyses provide key constraints on the timing of magmatism and deformation in the Deadman Creek area. Oligocene zircon crystallization ages from granodioritic and aplitic intrusions (~28–26 Ma) indicate that magmatism occurred during the early stages of Rio Grande rift extension. The mylonitic granodioritic dike intruded into mylonitic Proterozoic gneiss near Short Creek (sample 23-6-ShC1) yielded a crystallization age of 27.9 ± 0.32 Ma, and cathodoluminescence imaging confirms oscillatory zoning consistent with primary igneous crystallization. Mylonitic deformation microstructures of this unit, as well as a c-axis opening angle temperature of 428 ± 50°C, indicate upper greenschist facies deformation conditions, which would only have been present shortly after emplacement due to elevated heat flow associated with magmatism. These relationships demonstrate synkinematic magmatic activity and indicate that ductile shearing was active in the late Oligocene. Additionally, one of the published samples from the USGS 2019 data release (90913-3A) is a chlorite mylonite derived from the Proterozoic gneiss but with several Oligocene zircons. Therefore it is likely that there is an Oligocene intrusive component in that sample, which is from one of the thickest and highest strain parts of the Duncan shear zone near the western end of Deadman Creek. The presence of mylonitic Oligocene intrusions in this area further supports a close spatial and temporal link between magmatism and formation of the Duncan shear zone. Given the elevated deformation temperatures and kinematics observed in the Duncan shear zone, we interpret the mylonites in this shear zone to be associated with proximal magmatic intrusions at depth. Heat from these intrusions would locally elevate the geothermal gradient, facilitating higher-temperature deformation and generation of mylonitic fabrics surrounding the intrusion, with the orientations of these fabrics influenced by their position relative to the magma body (e.g., Lister and Baldwin, 1993).

An aplite dike (24-5-MP233b) along a normal fault strand in the Short Creek fault system yielded a U-Pb zircon age of 26.2 ± 0.25 Ma. The dike contains well-developed top-NE shear fabrics and slickenfibers, suggesting synkinematic emplacement during active slip on the fault. These results collectively imply that faulting was already underway during or immediately after Oligocene magmatism, supporting a late Oligocene onset of the Short Creek fault system. Quartz microstructures along the Short Creek fault system record brittle-plastic strain (~250–300°C); however, the most pronounced quartz plasticity (prism + basal <a> slip and subgrain rotation dynamic recrystallization) occurs in slickenfibers along the aplite dike, suggesting that thermal input from the intrusion locally elevated deformation temperatures and facilitated crystal plastic strain. This relationship further ties the timing of brittle-plastic deformation along the Short Creek fault system to ~26 Ma. Additionally, aplite/felsite dikes near Deadman Creek from the USGS data release (Holm-Denoma et al. 2019) record ages of ~26–30 Ma, with the most well constrained sample yielding an age of 26.7 ± 0.09 Ma (52015-6A, Figure 23F). These aplites locally cut the high-strain, top-SW mylonitic fabrics of the Duncan shear zone. This indicates that ductile shearing in the Duncan shear zone had largely ceased by ~26–27 Ma and perhaps shortly after emplacement of ~28 Ma intrusions.

The timing of normal slip on the Short Creek fault system timing differs from the broader Sangre de Cristo fault system, where thermochronology data indicate that the rocks near the western range front of the Sangre de Cristo Range were at temperatures of ~200–270°C at the ~13–11 Ma onset of rapid cooling associated with the Sangre de Cristo fault system (e.g., Singleton et al., 2024; Malavarca et al., 2024). Thus, deformation on the Short Creek fault system (~26 Ma based on the aplite dike U-Pb geochronology data described above) predates major range-bounding fault activity by at least 13 million years and reflects an earlier phase of extensional reactivation localized on inherited Laramide structures.

2.13 Synthesis and Tectonic History

The integrated structural, geochronologic, and microstructural data suggest a multi-stage tectonic evolution for the Deadman Creek thrust area, described below and shown in Figure 26:

1. Proterozoic basement formation and polyphase deformation associated with the Yavapai Orogeny (~1.8–1.7 Ga; Jones and Connelly, 2006), emplacement of Mesoproterozoic (~1.43 Ga) quartz monzonite, with later Cambrian or early Ordovician gabbroic intrusions emplaced prior to Middle Ordovician sedimentation.
2. Middle Ordovician and later Paleozoic sedimentation on Proterozoic basement and deposition of the Ordovician Harding Formation, Leadville Limestone, Minturn Formations, and other sedimentary units.
3. Laramide shortening created the Deadman Creek thrust, including a duplex structure, placing basement over Paleozoic strata and producing top-NE mylonitic fabrics along a narrow (<10 m thick) zone, primarily focused in Mississippian-Devonian calcareous units.

4. Laramide development of NE-vergent folds associated with SW-dipping reverse faults at depth, which could represent progressive deformation associated with an imbricate Deadman Creek thrust system.
5. Late Oligocene magmatism (~28 Ma) and development of coaxial and top-SW mylonites in the Duncan shear zone.
6. Formation of the Short Creek normal fault system and brittle-plastic deformation on the NE-dipping limbs of the Deadman Creek thrust, locally coeval with aplite dike emplacement at ~26 Ma.
7. Slip on the Sangre de Cristo fault system likely initiated in the middle Miocene, as suggested by regional thermochronology (Singleton et al., 2024). Activity continued after the Last Glacial Maximum into the Quaternary, as evidenced by fault scarps preserved in young sediments west of the range front.

Overall, the Deadman Creek area illustrates how contractional structures were overprinted by early stages of extension during Rio Grande rift initiation. The results show that the earliest phases of rifting were dominated by plastic deformation at temperatures significantly higher than those associated with later, cooler stages of extension along the Sangre de Cristo fault system. Early extensional strain was strongly localized and guided by thermal weakening from synkinematic Oligocene magmatism as well as by structural reactivation of preexisting weaknesses, specifically the top-SW/general-shear reactivation of the Deadman Creek thrust and brittle-plastic reactivation of the NE-dipping limb of the folded thrust by the Short Creek fault system.

These observations align with patterns documented elsewhere in the Rio Grande rift, where early rift deformation was similarly localized by synkinematic magmatism and structural inheritance.

For example, mylonitic early-rift deformation was localized by synkinematic magmatism in the ~30 Ma Chokecherry granite (Malavarca et al., 2024), and ~26–23 Ma extensional SW-directed shearing along the Independence Mine shear zone reactivated older reverse faults (Sitar et al., 2025). Together with these regional examples, the Deadman Creek area provides an important window into the structurally guided nature of early Rio Grande rift extension, bridging the gap between Laramide basement-involved shortening and the onset of later, cooler and more brittle rift-related faulting.

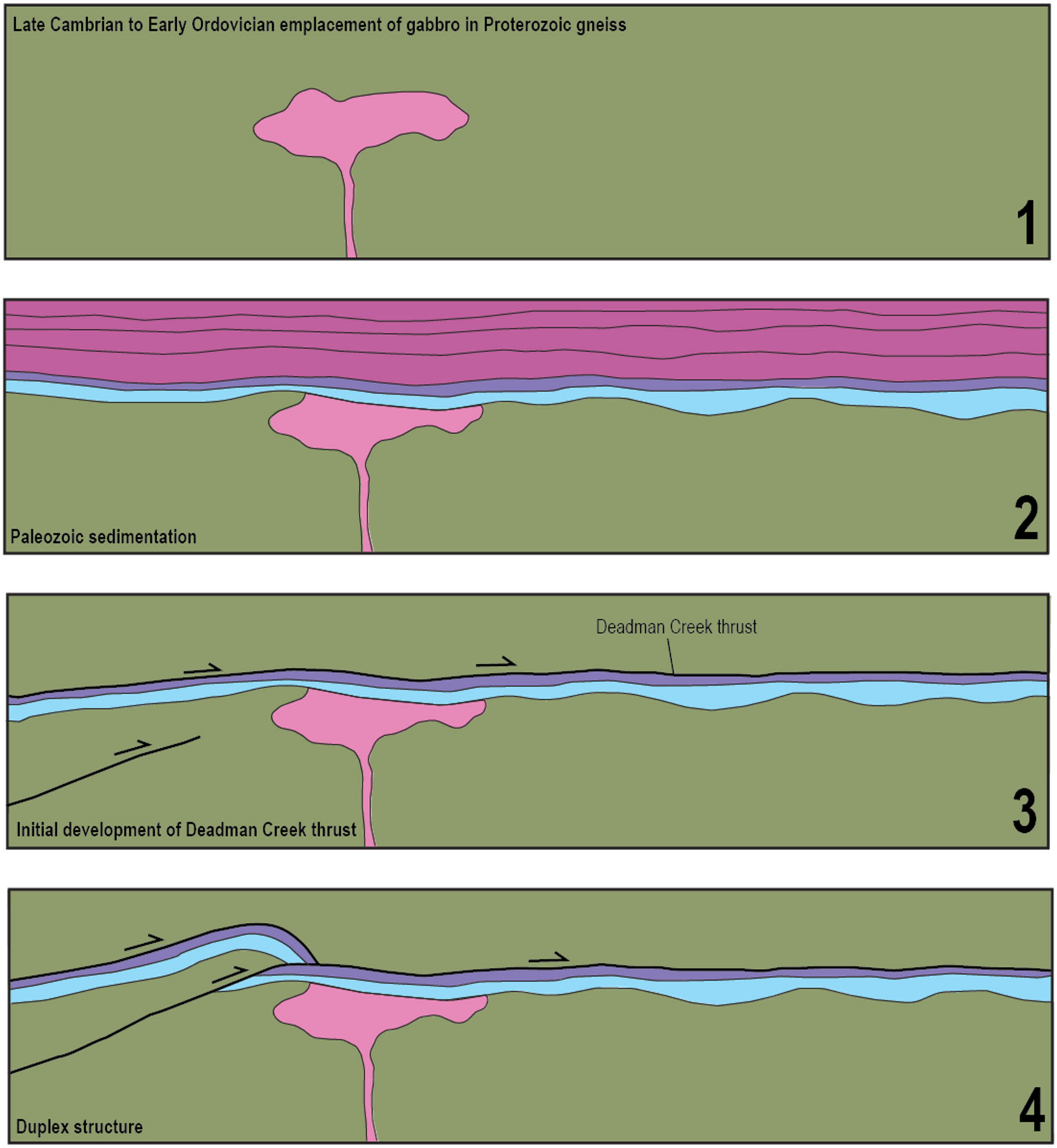

Figure 26: Sequential cross sections showing tectonic evolution of the Deadman Creek thrust. (1) Proterozoic basement (green) formation and emplacement of Cambrian to early Ordovician gabbroic intrusions (pink). (2) Middle Ordovician marine sedimentation on Proterozoic basement and gabbroic intrusion, including deposition of the Ordovician Harding Formation (light blue), Mississippian and Devonian carbonates (purple), and Pennsylvanian Minturn Formation (magenta). (3) Laramide contraction resulting in initial development of the Deadman Creek thrust, placing Proterozoic basement over Paleozoic strata and producing top-NE mylonitic fabrics localized within a narrow (<10 m thick) shear zone, primarily in Mississippian-Devonian carbonate units. The Minturn formation is mostly cut out by the thrust. (4) Continued Laramide deformation including onset on duplex structure linked to SW-dipping reverse faults at depth, potentially representing progressive deformation within an imbricate Deadman Creek thrust system.

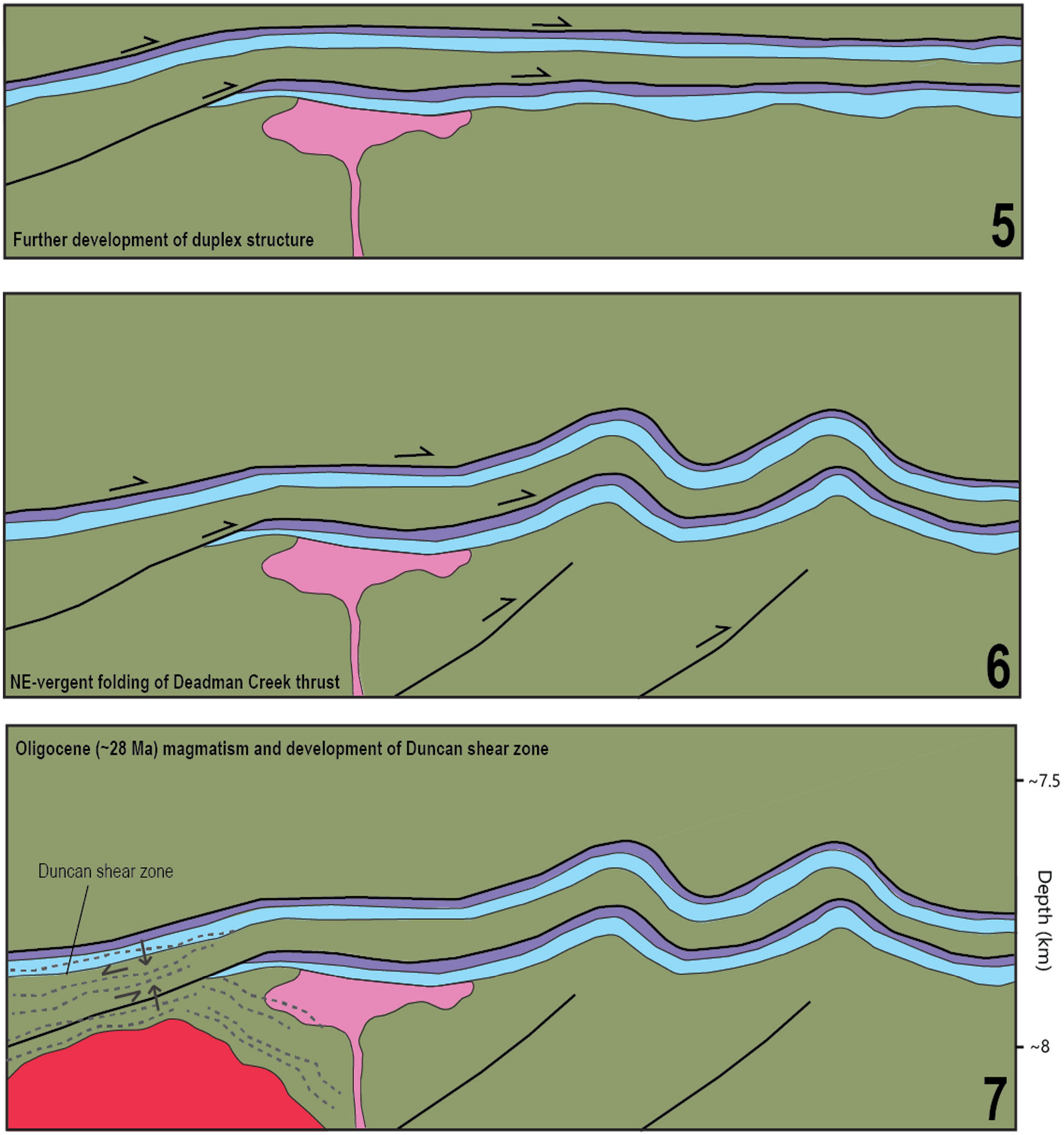

Figure 26 Cont: (5) Further development of duplex structure producing a repeated sequence of Paleozoic units on crystalline basement. (6) NE-vergent folding of the Deadman Creek thrust duplex structure associated with additional SW-dipping reverse faults at depth. (7) Late Oligocene magmatism (~28 Ma) and development of coaxial and top-SW mylonitic fabrics within the Duncan shear zone.

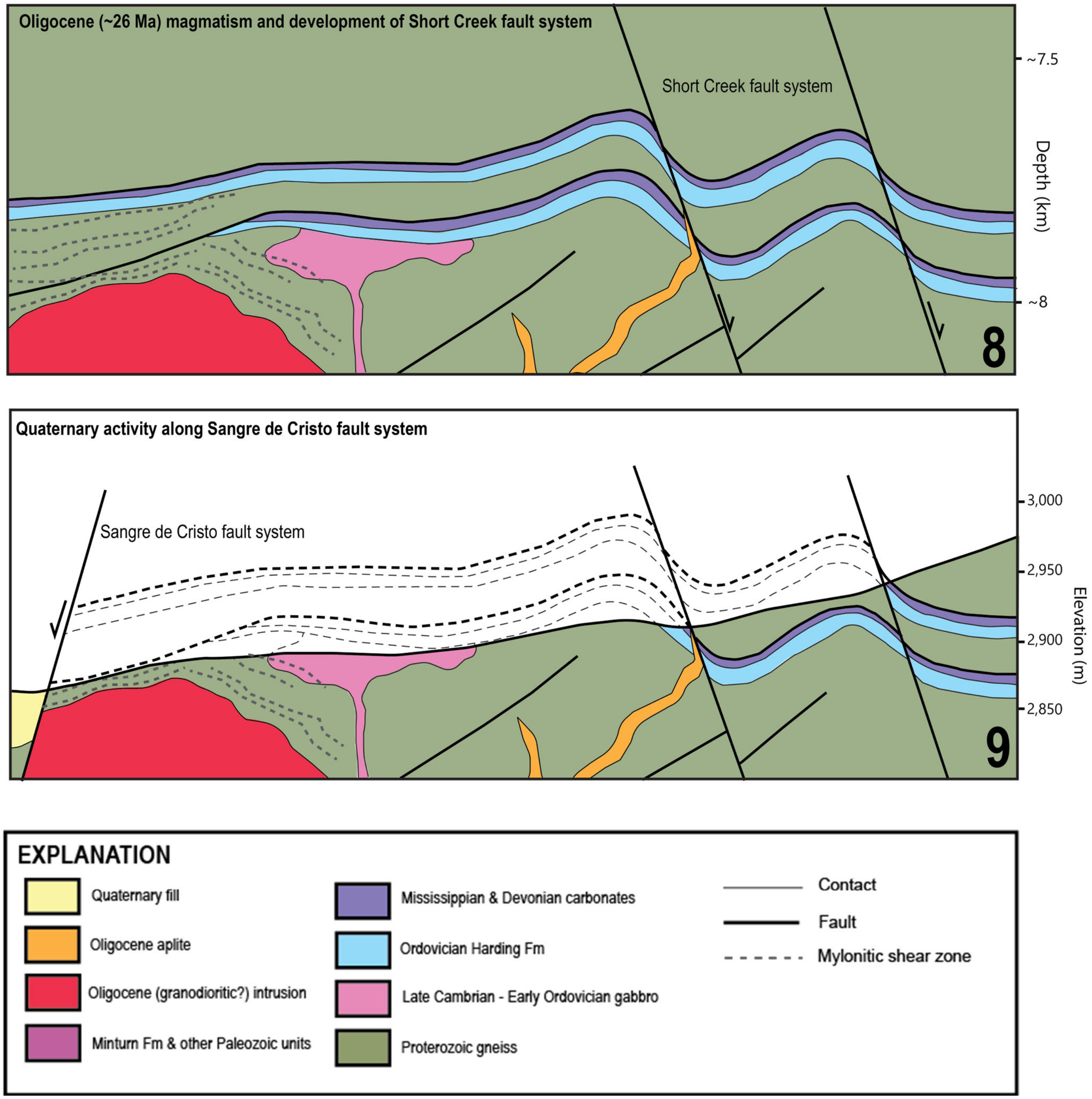

Figure 26 Cont: (8) Formation of the Short Creek normal fault system and associated brittle–plastic deformation along the NE-dipping limbs of the Deadman Creek thrust, locally coeval with emplacement of ~26 Ma aplite dikes. (9) Initiation of slip on the Sangre de Cristo fault system in the middle Miocene, as suggested by regional thermochronology (Singleton et al., 2024).

5. CONCLUSION

This study provides new structural, stratigraphic, and geochronologic constraints on the tectonic evolution of the Deadman Creek thrust area in the Sangre de Cristo Range. Detailed mapping and analysis reveal a complex history of basement deformation, early Paleozoic magmatism, Laramide contraction, and subsequent Rio Grande rift-related extension and magmatism. The Deadman Creek thrust places Proterozoic basement over Paleozoic strata and was later folded into a NE-vergent antiform consistent with late-stage Laramide shortening. This contractional structure was subsequently overprinted by Late Oligocene normal faulting and ductile shearing during the onset of rifting.

More broadly, the results show that early Rio Grande rift deformation in this region was strongly guided by structural inheritance and synextensional magmatism. Reactivation of the Deadman Creek thrust, both through top-SW general-shear overprinting in the Duncan shear zone and brittle-plastic reactivation of its NE-dipping limb by the Short Creek fault system (Figure 27), demonstrates that preexisting weaknesses exerted some control on the localization of strain. At the same time, synkinematic Oligocene intrusions thermally weakened the crust and focused mylonitic deformation during the earliest stages of extension, reinforcing patterns observed elsewhere in the Rio Grande rift.

These findings underscore that the transition from Laramide shortening to rift-related extension was neither simple nor uniform, but instead shaped by inherited structures, magmatic input, and spatially variable rheology. The overprinting of contractional and extensional regimes in the Deadman Creek area highlights the importance of structural inheritance in the evolution of the continental crust and serves as a reminder of the humbling complexity inherent in deciphering the geologic history of the Sangre de Cristo Range.

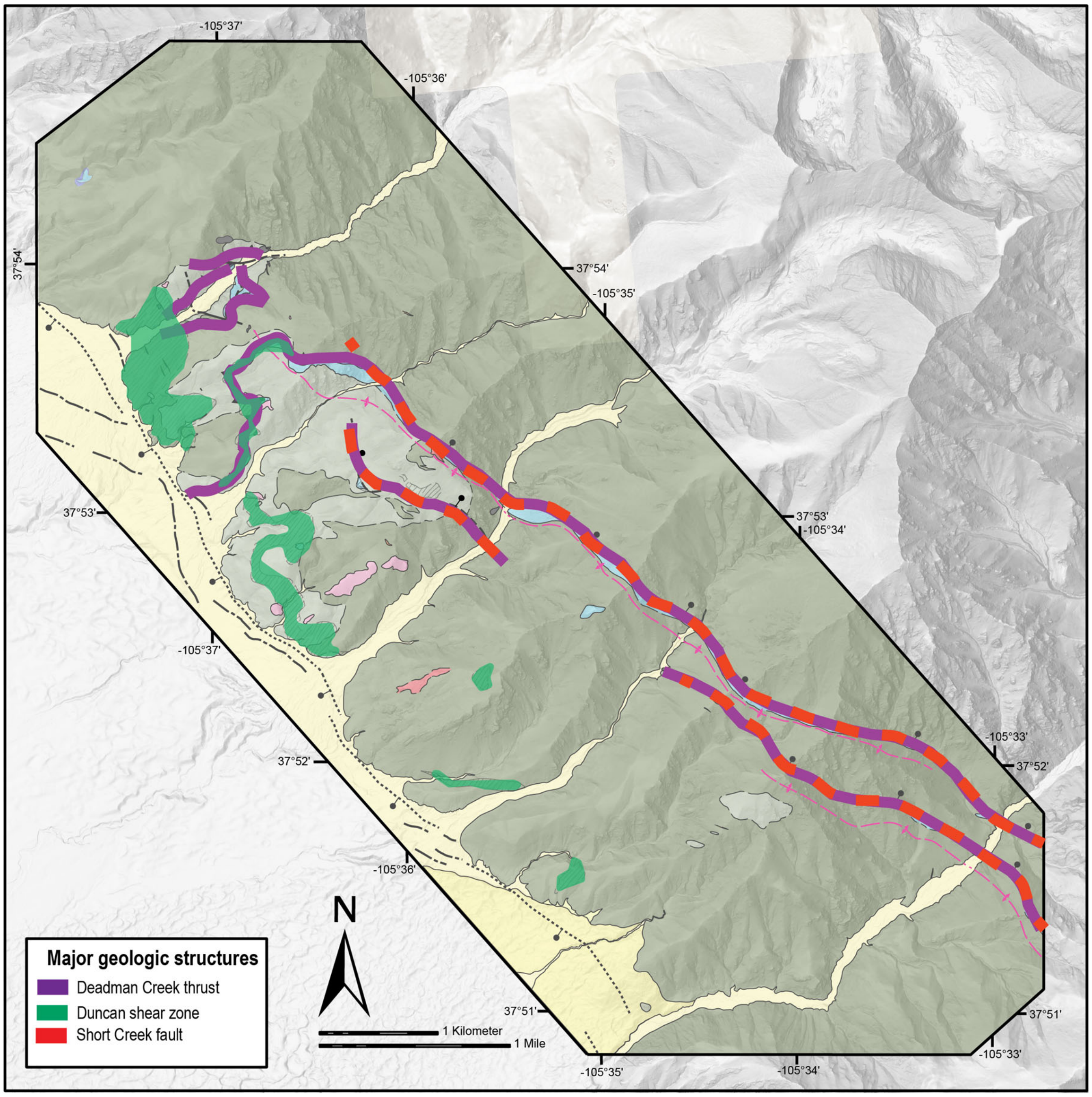

Figure 27: Simplified map of the study area with major identified geologic structures. The Duncan shear zone is shown in green, the Deadman Creek thrust in purple, and the Short Creek fault in red. These structures define the primary structural framework of the study area and highlight the spatial relationships between major zones of deformation.

TABLE 1: Electron backscatter diffraction (EBSD) quartz CPO and temperature data

Pole figures	Sample ID	Unit of deformed rock	General Location	UTM Easting	UTM Northing	Thin section sense of shear	Shear indicated by pole figure	Slip system(s) active	Opening angle	Estimated quartz deformation temperature (± 50°C)	Notes
A	24-8-MP288	Harding Quartzite (Oh)	North of Pole Creek	446429.62	4192791.83	Top-SW	Coaxial, minor top-NE	Prism <a>	35°	290°	
B	24-8-MP298	Harding Quartzite (Oh)	North of Pole Creek	446422.94	4192778.67	Mix of top-SW and top-NE	Coaxial, minor top-SW	Prism <a>	35°	290°	
C	24-8-MP326	Harding Quartzite (Oh)	Alpine Creek	445896.97	4193301.84	Top-SW	Coaxial, minor top-NE	Prism <a>	66°	503°	
D	24-8-MP333	Harding Quartzite (Oh)	Alpine Creek	445832.32	4193260.55	Top-SW	Top-SW	Prism <a>	48°	379°	
E	24-8-MP394	Harding Quartzite (Oh)	Alpine Creek	446026.93	4193661.15	Coaxial	Coaxial	Prism <a>	23°	207°	Unreliable temperature estimates
F	24-10-MP1038	Harding Quartzite (Oh)	Deadman Creek	445433.61	4194503.46	Top-W/SW	Coaxial	Prism <a>	77°	580°	Unreliable temperature estimates
G	24-10-MP1113	Proterozoic Quartzite (Xq)	Deadman Creek	445352.49	4194574.24	Top-W	Coaxial, minor top-E	Prism <a>	74°	559°	
H	24-8-MP387a	Harding Quartzite (Oh)	Alpine Creek	445982.19	4193584.55	Top-NE	Top-SW	Prism <a>, Prism <c>	58°	455°	
I	23-6-ShC1	Granodioritic intrusion (Tgd)	Short Creek	447452.34	4191077.16	Top-SW	Top-SW	Prism <a>	55°	428°	
J	23-6-ShC6	Proterozoic gneiss (Xgn)	Short Creek	447976.46	4191015.02	Coaxial	Coaxial	Prism <a>	57°	441°	
K	24-8-MP662	Quartz Monzonite (Yqm)	Mouth of Pole Creek	446588.42	4192179.20	Top-SW	Top-SW	Prism <a>	51°	396°	
L	24-10-MP1244	Quartz Monzonite (Yqm)	South of Deadman Creek	445432.19	4193813.98	Top-SW	Top-SW	Prism <a>	45°	359°	
M	24-5-MP233b	Aplite intrusion (Ta)	North of Pole Creek	446928.57	4193206.78	Top-NE normal slip	N/A	Prism <a>, Basal <a>	N/A	N/A	Normal fault surface. No opening angle recognized.

TABLE 2: Isotopic ages of rocks in the Deadman Creek thrust area

Sample ID	**Unit**	**UTM Easting**	**UTM Northing**	**Method**	**Interpreted age**	**Representation**	**General Location**	**Notes** N = # of crystals included in age measurement
23-6-ShC1	Tonalitic intrusion	447452.34	4191077.16	U-Pb Zircon	27.92 ± 0.16 Ma	Crystallization of intrusion	Short Creek	N = 18. Source: CU TRaiL Lab, this study.
24-5-233b	Aplitic dike	446928.57	4193206.78	U-Pb Zircon	26.2 ± 0.08 Ma	Crystallization of aplite	Pole Creek	N = 29. Source: CU TRaiL Lab, this study.
SLM_DM64	Gabbroic intrusion	446267.639	4192349.95	U-Pb Apatite	487 ± 86 Ma	Crystallization of gabbro	Pole Creek	N = 28. Source: CU TRaiL Lab, this study.
90913-3A	Chlorite, quartz mylonite	445295.83	4194424.16	U-Pb Zircon	27.8 ± 0.6 Ma	Age of metamorphism of mylonite	Deadman Creek	N = 2. Source: USGS 2023 data release.
91013-5A	Rhyolitic Porphyry, altered	445357.01	4194368.27	U-Pb Zircon	1616 ± 3 Ma	Average age of inherited zircon crystals in rhyolite	Deadman Creek	N = 44. Source: USGS 2023 data release.
91113-6B	Altered, aphanitic felsite	445250.76	4194258.02	U-Pb Zircon	28.3 ± 0.54 Ma	Crystallization of aplite	Deadman Creek	N = 4. Source: USGS 2023 data release.
91213-22A	Altered, aphanitic felsite	445110.89	4194381.01	U-Pb Zircon	29.6 ± 0.9 Ma	Crystallization of aplite	Deadman Creek	N = 2. Source: USGS 2023 data release.
52014-12A	Augen Gneiss	445569.50	4194588.77	U-Pb Zircon	1439 ± 13 Ma	Crystallization of gneiss	Deadman Creek	N = 27. Source: USGS 2023 data release.
52015-6A	Aphanitic to porphyritic felsite, likely rhyolite	447221.25	4194534.70	U-Pb Zircon	N/A	N/A	Deadman Creek	Source: USGS 2023 data release.
91917-3A	Altered, aphanitic felsite	445110.89	4194381.01	U-Pb Zircon	1675 ± 13 Ma	Age of inherited zircon crystals in rhyolite	Deadman Creek	N = 17. Source: USGS 2023 data release.
91917-5B	Rhyolitic porphyry, altered	447473.32	4194354.44	U-Pb Zircon	1681 ± 8 Ma	Age of inherited zircon crystals in rhyolite	Deadman Creek	N = 22. Source: USGS 2023 data release.

TABLE 3: Detrital zircon data from quartzites in the Deadman Creek thrust area

Sample ID	Lithology	UTM Easting	UTM Northing	Method	Discordance Filter	n Analyses	n Accepted	Age Population (Ma)	Major Age Peaks (Ma)	Interpretation	Notes
91113-13A	Quartzite	445541.14	4194423.63	Detrital Zircon	± 20% or < –5%	120	108	~900-3000	1700, 2700	Harding (Ordovician)	Source: USGS 2023 data release.
52014-14A	Quartzite	445596.39	4194666.26	Detrital Zircon	± 20% or < –5%	120	102	~1000-2500	1400, 1700	Sawatch (Cambrian)	Source: USGS 2023 data release.

6. REFERENCES

Abbey, A.L., and Niemi, N.A., 2020, Perspectives on Continental Rifting Processes From Spatiotemporal Patterns of Faulting and Magmatism in the Rio Grande Rift, USA: Tectonics, v. 39, p. e2019TC005635, doi:10.1029/2019TC005635.

Abbott, L.D., Flowers, R.M., Metcalf, J., Falkowski, S., and Niazy, F., 2022, Post-Laramide, Eocene epeirogeny in central Colorado—The result of a mantle drip? Geosphere, v. 18, p. 1223–1246, doi:10.1130/GES02434.1.

Allmendinger, R.W., Siron, C.R., and Scott, C.P., 2017, Structural data collection with mobile devices: Accuracy, redundancy, and best practices: Journal of Structural Geology, v. 102, p. 98–112, doi:10.1016/j.jsg.2017.07.011.

Behr, W.M., and Platt, J.P., 2014, Brittle faults are weak, yet the ductile middle crust is strong: Implications for lithospheric mechanics: Geophysical Research Letters, v. 41, p. 8067–8075, doi:10.1002/2014GL061349.

Benson, R.G., and Jones, D.M., 1990, Geology Of The San Luis Gold Deposit, Costilla County, Colorado: OneMine, https://www.onemine.org/documents/geology-of-the-san-luis-gold-deposit-costilla-county-colorado (accessed December 2025).

Brister, B.S., and Gries, R.R., 1994, Tertiary stratigraphy and tectonic development of the Alamosa basin (northern San Luis Basin), Rio Grande rift, south-central Colorado, *in* Keller, G.R. and Cather, S.M. eds., Basins of the Rio Grande Rift: Structure, Stratigraphy, and Tectonic Setting, Geological Society of America, p. 0, doi:10.1130/SPE291-p39.

Bush, M.A., Horton, B.K., Murphy, M.A., and Stockli, D.F., 2016, Detrital record of initial basement exhumation along the Laramide deformation front, southern Rocky Mountains: Tectonics, v. 35, p. 2117–2130, doi:10.1002/2016TC004194.

Cather, S.M., 2004, Laramide orogeny in central and northern New Mexico and southern Colorado: The Geology of New Mexico, A Geologic History, p. 203–248, doi:https://www.researchgate.net/publication/291806142_Laramide_orogeny_in_central_and_northern_New_Mexico_and_southern_Colorado.

Clement, J.F., 1952, Geology of the northeastern Baca Grant area, Saguache County, Colorado, The:

Corfu, F., Hanchar, J.M., Hoskin, P.W.O., and Kinny, P., 2003, Atlas of Zircon Textures: Reviews in Mineralogy and Geochemistry, v. 53, p. 469–500, doi:10.2113/0530469.

Faleiros, F.M., Moraes, R., Pavan, M., and Campanha, G.A.C., 2016, A new empirical calibration of the quartz c-axis fabric opening-angle deformation thermometer: Tectonophysics, v. 671, p. 173–182, doi:10.1016/j.tecto.2016.01.014.

Grauch, V.J.S., Bedrosian, P.A., and Drenth, B.J., 2013, Advancements in understanding the aeromagnetic expressions of basin-margin faults—An example from San Luis Basin, Colorado: The Leading Edge, v. 32, p. 882–891, doi:10.1190/tle32080882.1.

Hayden, F.V., 1877, HM-01-04 Hayden 1877 General Geologic Map of Colorado: U.S. Government Printing Office.

Hielscher, R., and Schaeben, H., 2008, A novel pole figure inversion method: specification of the MTEX algorithm: Journal of Applied Crystallography, v. 41, p. 1024–1037, https://doi.org/10.1107/S0021889808030112.

HOLDSWORTH, R.E., BUTLER, C.A., and ROBERTS, A.M., 1997, The recognition of reactivation during continental deformation: Journal of the Geological Society, v. 154, p. 73–78, doi:10.1144/gsjgs.154.1.0073.

Holm-Denoma, C.S., Caine, J.S., and Pianowski, L.S., 2019, U-Pb zircon data for: The Poncha Pass and Deadman Creek areas, northern Sangre de Cristo mountains of south-central Colorado:, doi:10.5066/P96HNSNL.

Holm-Denoma, C.S., Matthews, W.A., Soar, L.K., Longman, M.W., and Hagadorn, J.W., 2022, Provenance of Devonian–Carboniferous strata of Colorado: The influence of the Cambrian and the Proterozoic: Rocky Mountain Geology, v. 57, p. 1–21, doi:10.24872/rmgjournal.57.1.1.

Hoy, R.G., and Ridgway, K.D., 2002, Syndepositional thrust-related deformation and sedimentation in an Ancestral Rocky Mountains basin, Central Colorado trough, Colorado, USA: GSA Bulletin, v. 114, p. 804–828, doi:10.1130/0016-7606(2002)114%3C0804:STRDAS%3E2.0.CO;2.

Hurtado, C., and Gallen, S.F., 2024, Exploring the impact of deglaciation on fault slip in the Sangre de Cristo Mountains, Colorado, USA: Geology, v. 53, p. 150–154, doi:10.1130/G52661.1.

Johnson, B.R., Lindsey, D.A., Bruce, R.M., and Soulliere, S.J., 1987, Reconnaissance geologic map of the Sangre de Cristo Wilderness Study Area, south-central Colorado: Miscellaneous Field Studies Map Report 1635B, doi:10.3133/mf1635B.

Johnson, B.R., Lindsey, D.A., Ellis, C.E., Hannigan, B.J., and Thompson, J.R., 1984, Mineral resource potential map of the Sangre de Cristo Wilderness study area, south-central Colorado: Miscellaneous Field Studies Map Report 1635A, doi:10.3133/mf1635A.

Jones, J.V., III, and Connelly, J.N., 2006, Proterozoic tectonic evolution of the Sangre de Cristo Mountains, southern Colorado, U.S.A.: Rocky Mountain Geology, v. 41, p. 79–116, doi:10.2113/gsrocky.41.2.79.

Jones, J.V., III, Connelly, J.N., Karlstrom, K.E., Williams, M.L., and Doe, M.F., 2009, Age, provenance, and tectonic setting of Paleoproterozoic quartzite successions in the southwestern United States: GSA Bulletin, v. 121, p. 247–264, doi:10.1130/B26351.1.

Julyan, R., 1998, The Place Names of New Mexico: University of New Mexico Press.

Kirkland, C.L., Slagstad, T., and Johnson, T.E., 2018, Zircon as a metamorphic timekeeper: A case study from the Caledonides of central Norway: Gondwana Research, v. 61, p. 63–72, doi:10.1016/j.gr.2018.05.005.

Kluth, C.F., and Schaftenaar, C.H., 1994, Depth and geometry of the northern Rio Grande rift in the San Luis Basin, south-central Colorado, *in* Keller, G.R. and Cather, S.M. eds., Basins of the Rio Grande Rift: Structure, Stratigraphy, and Tectonic Setting, Geological Society of America, p. 0, doi:10.1130/SPE291-p27.

Kohlstedt, D.L., Evans, B., and Mackwell, S.J., 1995, Strength of the lithosphere: Constraints imposed by laboratory experiments: Journal of Geophysical Research: Solid Earth, v. 100, p. 17587–17602, doi:10.1029/95JB01460.

Kruhl, J.H., 1998, Reply: prism- and basal-plane parallel subgrain boundaries in quartz: a microstructural geothermobarometer: Journal of Metamorphic Geology, v. 16, p. 142–146, http://dx.doi.org/10.1046/j.1525-1314.1996.00413.x.

Law, R.D., 2014, Deformation thermometry based on quartz c-axis fabrics and recrystallization microstructures: A review: Journal of Structural Geology, v. 66, p. 129–161, doi:10.1016/j.jsg.2014.05.023.

Leonard, E.M., Laabs, B.J.C., Plummer, M.A., Kroner, R.K., Brugger, K.A., Spiess, V.M., Refsnider, K.A., Xia, Y., and Caffee, M.W., 2017, Late Pleistocene glaciation and deglaciation in the Crestone Peaks area, Colorado Sangre de Cristo Mountains, USA – chronology and paleoclimate: Quaternary Science Reviews, v. 158, p. 127–144, doi:10.1016/j.quascirev.2016.11.024.

Lindsay, D.A., Andriessen, P. a. M., and Wardlaw, B.R., 1986, Heating, cooling, and uplift during Tertiary time, northern Sangre de Cristo Range, Colorado (USA): Geological Society of America Bulletin, v. 97, p. 1133–1143, doi:10.1130/0016-7606(1986)97%3C1133:HCAUDT%3E2.0.CO;2.

Lindsey, D.A., 2010, The geologic story of Colorado's Sangre de Cristo range: US Department of the Interior, US Geological Survey, v. 1349.

Lindsey, D.A., and Caine, J.S., 2024, Thick- and thin-skinned contractional styles and the tectonic evolution of the northern Sangre de Cristo Mountains, Colorado, USA: Geosphere, v. 20, p. 678–710, doi:10.1130/GES02635.1.

Lindsey, D.A., Clark, R.F., and Soulliere, S.J., 1986a, Minturn and Sangre de Cristo Formations of Southern Colorado: A Prograding Fan Delta and Alluvial Fan Sequence Shed from the Ancestral Rocky Mountains, *in* Peterson, J.A. ed., Paleotectonics and sedimentation in the Rocky Mountain Region, United States, American Association of Petroleum Geologists, v. 41, p. 0, doi:10.1306/M41456C26.

Lindsey, D.A., Johnson, B.R., and Andriessen, P.A.M., 1984a, Laramide and Neogene Structure of Northern Sangre de Cristo Range, South-Central Colorado: ABSTRACT: AAPG Bulletin, v. 68, p. 941, doi:10.1306/AD461548-16F7-11D7-8645000102C1865D.

Lindsey, D.A., Johnson, B.R., Soulliere, S.J., Bruce, R.M., and Hafner, K., 1986b, Geologic map of the Beck Mountain, Crestone Peak, and Crestone quadrangles, Custer, Huerfano, and Saguache counties, Colorado: Miscellaneous Field Studies Map Report 1878, doi:10.3133/mf1878.

Lindsey, D.A., Scott, G.R., Soulliere, S.J., and De Angelis, B.L., 1984b, Geologic map of the Horn Peak Quadrangle, Custer and Saguache counties, Colorado: Miscellaneous Field Studies Map Report 1623, doi:10.3133/mf1623.

Lister, G.S., and Baldwin, S.L., 1993, Plutonism and the origin of metamorphic core complexes: Geology, v. 21, p. 607–610, doi:10.1130/0091-7613(1993)021%3C0607:PATOOM%3E2.3.CO;2.

Machette, M.N., Coates, M.-M., and Johnson, M.L., 2007, 2007 Rocky Mountain section Friends of the Pleistocene field trip - Quaternary geology of the San Luis basin of Colorado and New Mexico, September 7-9, 2007: U.S. Geological Survey 2007–1193, doi:10.3133/ofr20071193.

Madole, R.F., Romig, J.H., Aleinikoff, J.N., VanSistine, D.P., and Yacob, E.Y., 2008, On the origin and age of the Great Sand Dunes, Colorado: Geomorphology, v. 99, p. 99–119, doi:10.1016/j.geomorph.2007.10.006.

Magnin, B.P., Kuiper, Y.D., and Anderson, E.D., 2023, Ediacaran-Ordovician Magmatism and REE Mineralization in the Wet Mountains, Colorado, USA: Implications for Failed Continental Rifting: Tectonics, v. 42, p. e2022TC007674, doi:10.1029/2022TC007674.

Malavarca, S., Singleton, J., Hudson, M., Wong, M., Rahl, J, Primus, M., Broeder, H., Moscati, R.J., 2024, Early stages of Rio Grande rift deformation recorded by the Oligocene Chokecherry granite, southern Colorado: GSA Connects Meeting (Anaheim, CA), https://gsa.confex.com/gsa/2024AM/webprogram/Paper402949.html (accessed April 2026).

Malavarca, S., Singleton, J., Sitar, M., Rahl, J., and Magloughlin, J.F., 2023, Cenozoic Metamorphism and Along-Strike Peak Temperatures in the Pennsylvanian Minturn Formation in the Sangre de Cristo Range: Unraveling the Complex Thermal History of the Rio Grande Rift in Southern Colorado: Geological Society of America Abstracts, v. 55, p. 387928, doi:10.1130/abs/2023RM-387928.

Marrett, R., and Allmendinger, R.W., 1990, Kinematic analysis of fault-slip data: Journal of Structural Geology, v. 12, p. 973–986, doi:10.1016/0191-8141(90)90093-E.

McCalpin, J., 1981, Quaternary Geology and Neotectonics of the West Flank of the Northern Sangre de Cristo Mountains, South-Central Colorado, doi:10.13140/RG.2.2.25742.77129.

Morgan, S.S., and Law, R.D., 2004, Unusual transition in quartzite dislocation creep regimes and crystal slip systems in the aureole of the Eureka Valley-Joshua Flat-Beer Creek pluton, California: a case for anhydrous conditions created by decarbonation reactions: Tectonophysics, v. 384, p. 209–231, doi:10.1016/j.tecto.2004.03.016.

Passchier, C.W., and Trouw, R.A.J. (Eds.), 2005, Deformation Mechanisms, *in* Microtectonics, Berlin, Heidelberg, Springer Berlin Heidelberg, p. 25–66, doi:10.1007/3-540-29359-0_3.

Ricketts, J.W., Kelley, S.A., Karlstrom, K.E., Schmandt, B., Donahue, M.S., and van Wijk, J., 2016, Synchronous opening of the Rio Grande rift along its entire length at 25–10 Ma supported by apatite (U-Th)/He and fission-track thermochronology, and evaluation of possible driving mechanisms: GSA Bulletin, v. 128, p. 397–424, doi:10.1130/B31223.1.

Ruleman, C.A., and Brandt, T.R., 2021, Surficial geology of the northern San Luis Valley, Saguache, Fremont, Custer, Alamosa, Rio Grande, Conejos, and Costilla Counties, Colorado: U.S. Geological Survey 3475, doi:10.3133/sim3475.

Ruleman, C., and Machette, M., 2007, An Overview of the Sangre de Cristo Fault System and New Insights to Interactions Between Quaternary Faults in the Northern Rio Grande Rift.

Şengör, A.M.C., Lom, N., and Sağdıç, N.G., 2019, Tectonic inheritance, structure reactivation and lithospheric strength: the relevance of geological history, *in* Wilson, R.W., Houseman, G.A., McCaffrey, K.J.W., Doré, A.G., and Buiter, S.J.H. eds., Fifty Years of the Wilson Cycle Concept in Plate Tectonics, Geological Society of London, v. 470, p. 0, doi:10.1144/SP470.8.

Sibson, R.H., 1983, Continental fault structure and the shallow earthquake source: Journal of the Geological Society, v. 140, p. 741–767, doi:10.1144/gsjgs.140.5.0741.

Singleton, J., Ghamedi, O., Malavarca, S., Sitar, M., Wong, M., Rahl, J., and O'Sullivan, P., 2024, NEW INSIGHTS INTO LARAMIDE CONTRACTION, OLIGOCENE METAMORPHISM, AND RIO GRANDE RIFT EXTENSION IN THE SANGRE DE CRISTO RANGE (SOUTHERN COLORADO) FROM MID- AND LOW-TEMPERATURE THERMOCHRONOLOGY, doi:10.1130/abs/2024AM-402844.

Singleton, J.S., Rahl, J.M., and Befus, K.S., 2020, Rheology of a coaxial shear zone in the Virginia Blue Ridge: Wet quartzite dislocation creep at ~250–280 °C: Journal of Structural Geology, v. 140, p. 104109, doi:10.1016/j.jsg.2020.104109.

Sitar, M.C., 2023, Geologic mapping and kinematic analysis of the Independence Mine shear zone in the Sangre de Cristo Range, southern Colorado: extensional reactivation of a Laramide reverse fault: M.S. Thesis, https://hdl.handle.net/10217/236597 (accessed December 2025).

Sitar, M.C., Singleton, J.S., Rahl, J.M., Caine, J.S., King, J., Kylander-Clark, A., and O'Sullivan, P., 2025, Structural analysis of brittle-plastic shear zones in the Sangre de Cristo Range, southern Colorado, USA: Superposition of Rio Grande rift extension on Laramide contraction: Geosphere, v. 21, p. 446–469, doi:10.1130/GES02772.1.

Smith, T.M., Saylor, J.E., Lapen, T.J., Hatfield, K., and Sundell, K.E., 2023, Identifying sources of non-unique detrital age distributions through integrated provenance analysis: An example from the Paleozoic Central Colorado Trough: Geosphere, v. 19, p. 471–492, doi:10.1130/GES02541.1.

Stipp, M., Stünitz, H., Heilbronner, R., and Schmid, S.M., 2002, The eastern Tonale fault zone: a 'natural laboratory' for crystal plastic deformation of quartz over a temperature range from 250 to 700 °C: Journal of Structural Geology, v. 24, p. 1861–1884, doi:10.1016/S0191-8141(02)00035-4.

Sweet, D.E., and Soreghan, G.S., 2010, Late Paleozoic tectonics and paleogeography of the ancestral Front Range: Structural, stratigraphic, and sedimentologic evidence from the Fountain Formation (Manitou Springs, Colorado): GSA Bulletin, v. 122, p. 575–594, doi:10.1130/B26554.1.

Tweto, O., 1979, Geologic Map of Colorado: Colorado Geological Survey, Department of Natural Resources Miscellaneous Investigations 16.:

U.S. Geological Survey, 2021, 3D Elevation Program 1-Meter Resolution Digital Elevation Model:, https://apps.nationalmap.gov/downloader/.

Vermeesch, P., 2018, IsoplotR: A free and open toolbox for geochronology: SPECIAL ISSUE: Frontiers in geoscience:A tribute to Prof. Xuanxue Mo, v. 9, p. 1479–1493, doi:10.1016/j.gsf.2018.04.001.

Wallace, A.R., 2004, Evolution of the southeastern San Luis Basin margin and rthw Culebra Embayment, Rio Grande Rift, Southern Colorado:, https://nmgs.nmt.edu/publications/guidebooks/details.cfml?ID=117411 (accessed December 2025).

Watkins, T.A., 1996, Geology of the Northeastern San Luis Basin, Saguache County, CO: Geological Society of America, Field Trip Guides.

Weigel II, J.F., 2014, Evaluation of thrusting and folding of the Deadman Creek Thrust Fault, Sangre de Cristo range, Saguache County, Colorado: Colorado School of Mines.

Weil, A.B., and Yonkee, A., 2023, The Laramide orogeny: Current understanding of the structural style, timing, and spatial distribution of the classic foreland thick-skinned tectonic system, *in* Whitmeyer, S.J., Williams, M.L., Kellett, D.A., and Tikoff, B. eds., Laurentia: Turning Points in the Evolution of a Continent, Geological Society of America, v. 220, p. 0, doi:10.1130/2022.1220(33).

7. LIST OF SUPPLEMENTARY DATA INCLUDED SEPARATELY

Plate 1: Geologic Map of the Deadman Creek thrust area, Sangre do Cristo Range, southern Colorado

Dataset 1: Waypoints in Study Area

Dataset 2: Raw Structural Orientation Data from Study Area

Dataset 3: Per-Station Per-Structure Structural E1 Eigenvector Orientations

Dataset 4: Fault Orientation Data from Study Area

Dataset 5: Observed Kinematics Compilation

Dataset 6: Sample and Petrographic Section List with Kinematics

Dataset 7: Zircon and Apatite U-Pb Analytical Data

Supplementary File: U-Pb Geochronology R Script

Supplementary File: EBSD MATLAB Code

8. APPENDIX: DETAILED QUARTZ EBSD DATA

A. 24-8-MP288

Sample 24-8-MP288 is strained Harding quartzite (Oh) located in the footwall of the Deadman Creek thrust, just south of Alpine Creek. The outcrop where this quartzite mylonite was taken records gently NE-dipping mylonitic fabrics and NE-plunging lineations. The thin section from 24-8-MP288 records a clear top-SW foliation pattern defined by interstitial micas and slightly oblique quartz grains. The pole figures for this sample (Figure 18a) indicate a relatively symmetric CPO indicative of coaxial-dominated strain (c-axes are not rotated in a preferred direction) with a minor component of top-NE shear. This sample could represent two superposed shearing regimes (top-NE shear related to Deadman Creek thrust direction and top-SW shear related to Rio Grande rift extension). Because the micas dominantly indicate the top-SW foliation pattern, the recrystallized quartz may not record the same deformation regime as the micas and may represent an earlier deformation scheme. The inverse pole figure (Figure 18a suggests that the prism <a> slip system was the dominant quartz slip system, and the intensity spectrum indicates an opening angle of 35° which correlates to an estimated deformation temperature of 290 ± 50°C (Figure 19a).

B. 24-8-MP298

Sample 24-8-MP298 is quartzite mylonite derived from strained Harding quartzite (Oh) located in the footwall of the Deadman Creek thrust, just south of Alpine Creek and proximal to sample 24-8-MP288. Similar to 24-8-MP288, the outcrop where this sample was taken records shallow NE-dipping mylonitic foliation and NE-plunging lineation. The thin section from sample 24-8-MP298 records a mix top-SW and top-NE shear in quartz ribbons with BLG and SGR recrystallization and interstitial white micas. Both shear regimes are defined by S-C fabrics in distinct areas in the thin section. The pole figures (Figure 18b) symmetrical distribution of c- and a- axes with respect to foliation and lineation, indicating coaxial-dominated strain with a minor top-SW shear (general shear). The maxima on the pole figures indicate a clear opening angle of 35° which corresponds to an estimated deformation temperature of 290 ± 50°C (Figure 19b). This is the same estimated temperature as sample 24-8-MP288, which was taken from a nearby outcrop.

C. 24-8-MP326

Sample 24-8-MP326 is a fine-grained, finely foliated quartzite mylonite from the Harding Formation (Oh) in the footwall of the Deadman Creek thrust, found in Alpine Creek. The outcrop where this sample was taken recorded gently NW-dipping mylonitic foliation and WSW-plunging lineation. The sample contains mostly fine-grained quartz and interstitial white micas with pervasive SGR and BLG quartz recrystallization. The sample has a slight oblique grain shape fabric in quartz and a subtle preferred orientation of micas, both of which suggest top-SW shear. The pole figures for this sample (Figure 18c) are symmetrical and do not have high intensity maxima, though there is a slight top-NE shear asymmetry indicated by the orientation of c- and a- axes. This is not consistent with the thin section observations, indicating that the plastic strain by dislocation creep may not have been sufficient enough to reset the crystal orientation of the quartz grains in the sample. The intensity spectrum and ODF diagram for this sample (Figure 19c) indicate an opening angle of 66° which correlates to a deformation temperature of 503 ± 50°C.

D. 24-8-MP333

24-8-MP333 is another quartzite mylonite from the Harding formation (Oh) from the footwall of the Deadman Creek thrust in Alpine Creek with W-dipping mylonitic fabric and W-plunging lineations. Similar to sample 24-8-MP326, 24-8-MP333 is finely foliated and contains mostly fine-grained quartz with interstitial white mica. The quartz is pervasively recrystallized with SGR and BLG. An oblique foliation in the quartz grains and slight S-C fabric in micas indicate top-WSW sense of shear. The pole figures for this sample (Figure 18d) indicate a top-WSW sense of shear, which is consistent with the thin section observations. The inverse pole figure indicates prism <a> slip as the dominant dislocation creep slip system. The intensity spectrum and ODF diagram for this sample (Figure 19d) indicate an opening angle of 48° which correlates to a deformation temperature of 379 ± 50°C.

E. 24-8-MP394

Sample 24-8-MP394 was taken from an outcrop of the Harding Formation (Oh) in the footwall of the Deadman Creek thrust on the northern side of Alpine Creek. The mylonitic foliation in the outcrop is shallowly SW-dipping with SW-plunging lineation. This sample is a quartzite mylonite that is fine-grained, finely foliated, and contains uniform eye-shaped symmetrical quartz grains throughout the thin section. The thin section does not have a clear sense of shear, though an S-C fabric in some areas of the thin section shows apparent top-NE shear. Many of the elliptical quartz grains look symmetric, indicating coaxial strain and possible low-temperature pressure solution recrystallization. The pole figures (Figure 18e) do not indicate a clear pattern which would indicate sense of shear in the sample. The inverse pole figure indicates prism <a> slip was the dominant slip system on which dislocation creep was occurring. The pattern captured in the pole figures may indicate that pressure solution rather than dislocation creep was the dominant mechanism. Based on the geometry of the pole figures and ODF, the opening angle, 23°, and the estimated deformation temperature, 207 ± 50°C (Figure 19e), are not reliable estimates.

F. 24-10-MP1038

Sample 24-10-MP1038 is a quartzite protomylonite that was taken from an outcrop of the Harding Formation on the north side of Deadman Creek. The sample location is within the footwall of the Deadman Creek thrust and contains mylonitic foliation that is dipping to the SW as well as SW-plunging lineations. The thin section consists of finely foliated, recrystallized quartz grains with no clear sense of shear. Similar to 24-10-MP1113 and 24-8-MP326, there is a slight preferred orientation in white mica that indicates top-W shear. The quartz is recrystallized by SGR. The pole figures (Figure 18f) do not indicate a clear sense of shear or clear pattern, and the inverse pole figure indicates prism <a> slip. The pattern captured in the pole figures may indicate that pressure solution rather than dislocation creep was the dominant mechanism that was reorienting the crystals. Based on the geometry of the pole figures and ODF, the opening angle, 74°, and the estimated deformation temperature, 580 ± 50°C (Figure 19f), are not reliable.

G. 24-10-MP1113

Sample 24-10-MP1113 is a quartzite mylonite that was taken from the north side of Deadman Creek in the hanging wall of the Deadman Creek thrust and is interpreted to be from a pod of Proterozoic quartzite (Xq) within the Proterozoic gneiss (Xgn). The outcrop has SW-dipping mylonitic foliation and W-plunging lineation. The thin section shows primarily fine-grained quartz and mica that define a slight oblique fabric with respect to the overall foliation that is consistent with top-W shear. The quartz is recrystallized by SGR recrystallization. The orientation of the c- and a-axes in the pole figures (Figure 18g) indicates a slight top-E sense of shear, which is opposite of the thin section observations. Based on these results, it likely that sample 24-10-MP1113 records an older top-E shear fabric that has been incompletely overprinted by top-W shear. The intensity spectrum indicates an opening angle of 74° and corresponding deformation temperature of 559 ± 50°C (Figure 19g).

H. 24-8-MP387a

Sample 24-8-MP387a was taken from an outcrop exposure of the Deadman Creek thrust near Alpine Creek. This sample is a quartzite mylonite from the Harding Formation (Oh). It is from the footwall of the Deadman Creek thrust and records SW-dipping mylonitic foliation and SW-plunging lineation. The thin section from sample is dominantly quartz and is notably coarser-grained than other samples of the Harding Formation (Oh). The sense of shear is not obvious, but a slight oblique dynamically recrystallized grain shape fabric in quartz and overall foliation patterns indicate top-NE sense of shear. The pole figures (Figure 18h), however, indicate a clear top-SW shear pattern (c-axis girdle counterclockwise of the foliation). Contrasting with most other samples, the inverse pole figure indicates that both prism <a> and prism <c> slip systems were active during deformation, possibly indicative of higher temperature deformation. The coarser grain size of this sample may mean that the EBSD dataset is not complete or sufficiently large enough to capture the bulk CPO. Also, the CPOs of detrital quartz grains may not have been fully reset during deformation. The sample has an opening angle of 58°, corresponding to a deformation temperature of 455 ± 50°C (Figure 19h).

I. 23-6-ShC1

This sample is from a protomylonitic granodioritic intrusion (Tgd) near Short Creek with a zircon U-Pb date of 27.92 ± 0.16 Ma. The igneous body was intruded into Proterozoic gneiss (Xgn) in the footwall of the Deadman Creek thrust. The sample is a quartz-white mica mylonite taken from an outcrop with a gently-SW sipping mylonitic foliation and SW-plunging lineation. Microstructures include pervasive fracturing of feldspars, quartz ribbons with minor BLG and

SGR recrystallization, and secondary chlorite, white mica, and epidote. A clear S-C-C' fabric records top-SW sense of shear. The pole figures (Figure 18i) for this sample are consistent with these kinematics, with a clear top-SW asymmetric distribution of c- and a- axes, and the inverse pole figure indicates that prism <a> slip was the dominant quartz dislocation slip system active. The intensity spectrum and ODF c-axes pole figure indicate an opening angle of 55° which correlates to an estimated deformation temperature of 428 ± 50°C (Figure 19i).

J. 23-6-ShC6

This sample is a quartz-white mica mylonite from the Proterozoic gneiss (Xgn) collected east of sample 23-6-ShC1 and located within the same mylonitic zone. The mylonitic foliation is gently NW-dipping, and the lineation is plunging to the W. This sample has a distinct spaced foliation with mica and quartz microlithons. Quartz is dynamically recrystallized with SGR and BLG, while feldspars are pervasively fractured. Overall, the strain appears to be coaxial in thin section, as there are both top-SW and top-NE mica-lined shear bands in addition to symmetric microstructures. The pole figures for this sample (Figure 18j) are consistent with thin sections and indicate coaxial strain with a high degree of symmetry with respect to the foliation and lineation. Similar to sample 23-6-ShC1, the inverse pole figure indicates that prism <a> slip was the dominant quartz dislocation slip system. The intensity spectrum and ODF c-axes pole figure indicate an opening angle of 57° which correlates to an estimated deformation temperature of 441 ± 50°C (Figure 19j).

K. 24-8-MP662

24-8-MP662 is a quartz-white mica mylonite derived from Mesoproterozoic quartz monzonite (Yqm) from a mylonitic zone found proximal to the range front just north of Pole Creek. The location of this sample is in the footwall of the Deadman Creek thrust. The outcrop where this sample was taken records SE-dipping mylonitic foliation and E-plunging lineation. The sample has pervasively fractured feldspars, some quartz ribbons with minor BLG recrystallization, and an S-C fabric defined by white mica that indicates top-SW sense of shear. Consistent with thin section observations, the pole figures for 24-8-MP662 (Figure 18k) show clear c- and a-axes patterns that indicate top-SW shear. Additionally, the intensity spectrum and ODF diagram for this sample (Figure 19k) indicate an opening angle of 51° which correlates to a deformation temperature of 396 ± 50°C.

L. 24-10-MP1244

Sample 24-10-MP1244 is a quartz-white mica mylonite to ultramylonite just south of Deadman Creek with a clear, thinly spaced, foliation defined primarily by white mica with zones of recrystallized quartz and a clear S-C fabric that indicates top-SW sense of shear. The sample was taken from the footwall of the Deadman Creek thrust and is located in a range front-proximal mylonite zone. The outcrop displays shallow-SE dipping mylonitic foliation and NE-plunging lineation. The quartz in the sample is recrystallized by SGR and BLG. The sample also contains chlorite and subhedral opaque minerals. The protolith of this sample is Mesoproterozoic quartz monzonite (Yqm). Consistent with the thin section, the pole figures and inverse pole figure for 24-10-MP1244 (Figure 18l) indicate top-SW sense of shear and primarily basal <a> slip. The intensity spectrum indicates an opening angle of 45° and corresponding deformation temperature of 359 ± 50°C (Figure 19l).

M. 24-5-233b

Sample 24-5-233b is an aplite dike (Ta) from the core of a NE-dipping brittle-plastic normal fault that we interpret to be part of the Short Creek fault system. The aplite dike was intruded into Proterozoic gneiss (Xgn) in the footwall of the Deadman Creek thrust. The thin section contains fine-grained quartz, feldspar and white mica, with veins of coarse-grained quartz. Oblique foliation defined dominantly by the white mica indicates top-NE shear in the thin section. The top of the thin section coincides with the principal slip plane of the fault and consists of a plastically strained quartz slickenfiber that records BLG and SGR recrystallization and with an oblique grain shape fabric indicating top-NE shear. The pole figures and inverse pole figure for this sample (Figure 18m) suggests that the slip systems active while the quartz slickenfiber grew were likely prism <a> and basal <a> slip.. The plastic strain via dislocation creep in the quartz slickenfiber was likely not sufficient to reset the crystal lattice from the original slickenfiber orientation. Because of this, the orientation of c- and a- axes in the pole figures do not reliably record kinematics. There was no opening angle detected by the MATLAB processing script (Figure 19m).